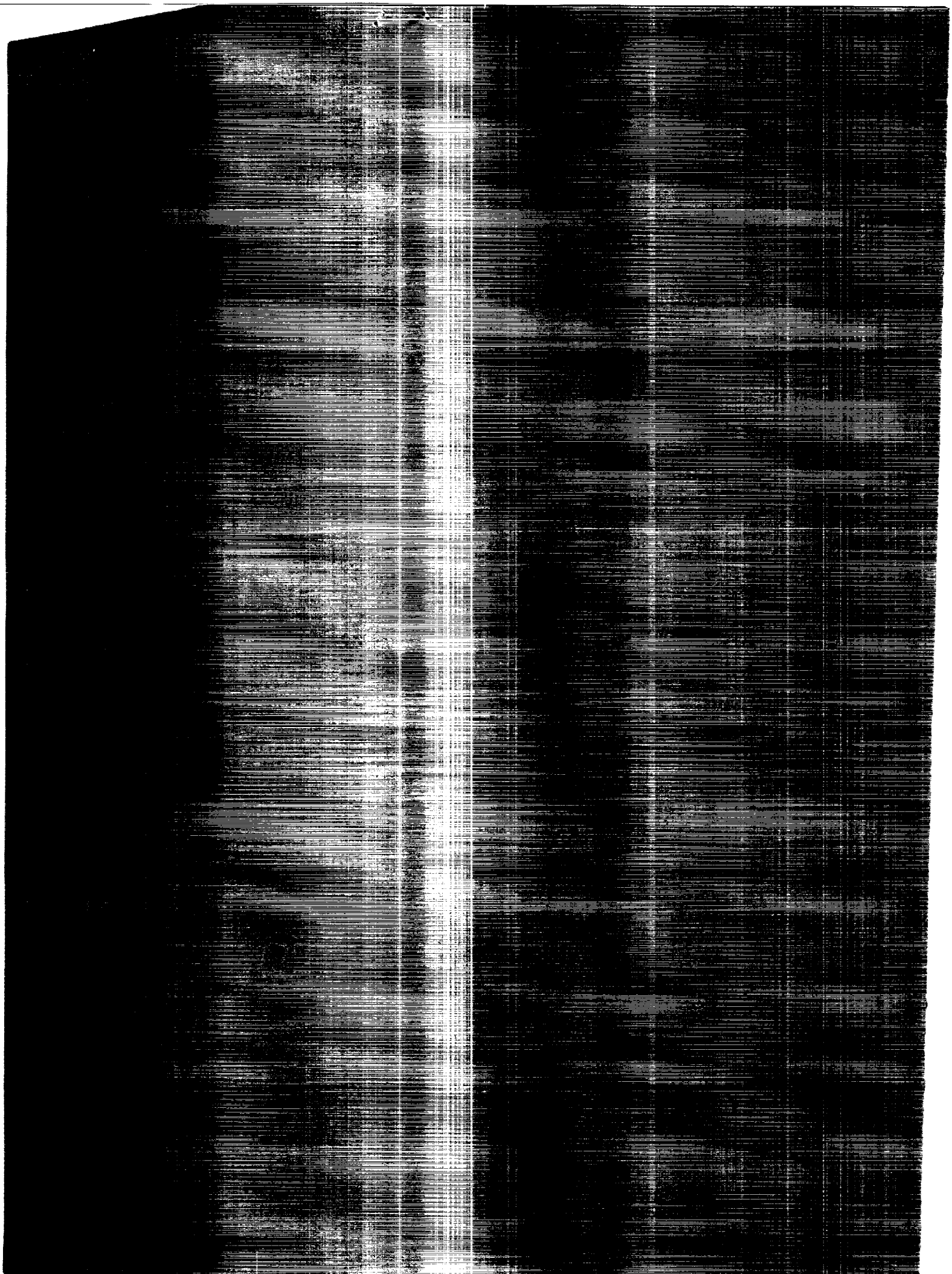

NASA Contractor Report 4254

Three-Dimensional Analysis of Surface Crack-Hertzian Stress Field Interaction

R. Ballarini and Y. Hsu
Case Western Reserve University
Cleveland, Ohio

Prepared for
Lewis Research Center
under Grant NAG3-396

National Aeronautics and
Space Administration
Office of Management
Scientific and Technical
Information Division

1989

TABLE OF CONTENTS

THREE-DIMENSIONAL ANALYSIS OF SURFACE CRACK-HERTZIAN STRESS FIELD INTERACTION

R. Ballarini and Y. Hsu

Dept. of Civil Engineering

Case Western Reserve University

Cleveland Ohio

SUMMARY

This thesis presents the results of a stress intensity factor analysis of semicircular surface cracks in the inner raceway of an engine bearing. The loading consists of a moving spherical Hertzian contact load and an axial stress due to rotation and shrink fit.

A three dimensional linear elastic Boundary Element Method code was developed to perform the stress analysis. The element library includes linear and quadratic isoparametric surface elements. Singular quarter point elements were employed to capture the square root displacement variation and the inverse square root stress singularity along the crack front. The program also possesses the capability to separate the whole domain into two subregions. This procedure enables one to solve non-symmetric fracture mechanics problems without having to separate the crack surfaces a priori.

A wide range of configuration parameters was investigated. The ratio of crack depth to bearing thickness was varied from one-sixtieth to one-fifth for several different locations of the Hertzian load. The stress intensity factors for

several crack inclinations were also investigated.

The results demonstrate the efficiency and accuracy of the Boundary Element Method. Moreover, the results can provide the basis for crack growth calculations and fatigue life prediction.

CHAPTER ONE

INTRODUCTION

Surface cracks commonly occur in machine and structural components. An example of such a component is a rotating engine bearing subjected to rolling contact. Under high speed rotation and cyclic contact loading, the surface crack initiating at the raceway of the bearing might propagate and lead to catastrophic failure. Raceway fracture is a totally unacceptable failure mechanism because it may cause serious damage to engine operations and consequently produce catastrophic engine failure. An accurate crack stress analysis of the surface-cracked component is essential in order to make a reliable prediction of fatigue life. However, due to the complexities of the nature of the surface crack problem, mathematical closed form solutions are not possible, and a numerical analysis or an experimental approach must be used to determine the stress intensity factors for surface cracks under different types of loading. The Boundary Element Method is an efficient and accurate tool for fracture mechanics analyses if singular elements and multi-domain crack modeling are employed. This method is used in this research.

Several factors will affect the growth of surface cracks in a rotational bearing under rolling contact loads. These include the geomety and inclination of the crack, the tensile hoop stress due to rotation and shrink fit, the moving Hertzian load, the pressure of the lubricant seeping into the crack, the shear stress on the raceway surface due to the sliding contact, and friction along the crack surfaces. A significant amount of research has been conducted aimed at gaining a better

understanding of the effects of each of these factors. While the surface crack is a three-dimensional problem, most of the analyses which appear in the literature are two-dimensional. These include the work of Way [1], which considers the effect of the lubricant, Fleming and Suh [2,3], which considers the effects of surface friction, Rosenfield [4], which considers the effects of crack surface friction, and Clark [5], which considers the effects of tensile hoop stresses. A recent paper by Mendelson and Ghosn [6] presents the results of fatigue life predictions of a propagating surface crack subjected to tensile hoop stresses and cyclic Hertzian contact loadings. Using a modified Forman-type crack propagation law they predicted the fatigue life of a typical bearing and compared their results with experimentally observed fatigue lives. Their predictions were conservative by a factor of 12. However, they demonstrated that the crack driving force in such problems is the alternating mixed-mode loading that occurs with each passage of the roller. Based on these results, the present research was aimed at quantifying the three-dimensional effects of the problem. Three dimensional analyses of surface cracks as applied to contact fatigue were recently performed by Murakami [7]. However, in his analysis the tensile hoop stresses were ignored. The model proposed in the present research neglects some of the factors mentioned previously. It is assumed that lubrication renders surface sliding friction negligible. The pressure on the crack surfaces which may arise from the lubricant seeping into the crack is ignored since the Hertzian loading moves past the crack very fast, thus the viscosity, compressibility, and inertia of the oil will prevent pressurization of the crack surfaces [8]. Moreover, since the radius of the Hertzian contact area is smaller than the surface length of the crack, the crack mouth will not be completely covered and the oil is allowed to squeeze out of the crack. The friction between the crack surfaces is neglected, since it tends to increase the resistance to crack growth.

This will lead to a conservative prediction of fatigue life.

Thus, the only factors assumed to be important in the present model are the mechanical loads arising from the Hertzian contact, rotation, and shrink-fit. The remaining five chapters of this paper are organized as follows:

In Chapter two the boundary integral equation is derived. The equation is reduced to a system of algebraic equations, and a procedure is described which treats the singularities which appear in the kernels. An algorithm for multi-domain analyses is also presented.

Chapter three is a brief review of linear elastic fracture mechanics. The formation of quarter point elements and traction singular elements as well as the displacement correlation method for calculating the stress intensity factors are also discussed. Several verification problems follow in Chapter four to elucidate the accuracy and efficiency of the Boundary Element Method for solving three dimensional linear elastic solid mechanics problems including crack stress analysis.

In Chapter five, the spherical Hertzian stress distribution and the hoop tensile stress due to the rotation and shrink fit of the inner raceway of the engine bearing are calculated. Results are presented for a wide range of configuration parameters. These include several different locations of the Hertzian load, different inclinations of the crack surface, several ratios of the crack depth to the raceway thickness and different intensities of the Hertzian load. A large number of the stress intensity factor versus these factors are presented.

The final chapter presents a discussion of the results and recommendations for future research.

CHAPTER TWO

BOUNDARY ELEMENT METHOD

This chapter reviews the development of the Boundary Element Method and presents a detailed derivation of the boundary integral equation. The procedures of numerical implementation and a multi-domain technique of the Boundary Element Method are also illustrated.

2.1 Introduction

The boundary integral equation was first derived explicitly by Rizzo [9], who reduced two dimensional isotropic elastostatics problems to an integral equation by using the Betti-Somigliana formula. The equation was then discretized into line segments along the boundary over which constant displacement and traction distributions are assumed to solve the elastic problem numerically. Although much of the mathematical theory of Rizzo's formula can be traced to Kupradze [10], and several papers about integral equation methods such as Jawson [11] and Symm [12], his work presented a clear form of the integral equation relating the boundary traction and displacement which is now commonly associated with the term " Boundary Integral Equation". Following Rizzo's work, Cruse [13] extended the Boundary Element Method to three dimensional isotropic elastic problems by using triangular elements with linear variations. The accuracy of the Boundary Element Method was later improved by Lachat and Watson [14], and Rizzo and Shippy [15] using higher order isoparametric elements. The application of the Boundary Element Method to fracture mechanics was carried out by Cruse [13], [16] by modeling the crack as an open notch. The results obtained using this

approach tend to be inaccurate because as the cracks surfaces are moved close to each other the system of equations becomes singular. This problem was remedied by Blandford et al. [17], who used two subregions to model the crack. The quarter-point technique developed for the Finite Element Method by Barsoum [18] was adopted and modified by Cruse and Wilson [19] to capture the square root singularity predicted by linear elastic fracture mechanics.

The Boundary Element Method developed in this paper utilizes four kinds of isoparametric surface elements: a three-node linear triangular element, a four-node linear quadrilateral element, a six-node quadratic triangular element, and eight-node quadratic quadrilateral element. A library of Gaussian integration quadrature is installed in a subroutine which can be used to accomplish the numerical integration. The quarter point element and the traction singular element are used in the program to represent the crack tip singularity. The multi-domain technique is also applied to model the topology.

2.2 Derivation of Boundary Integral Equation

The mathematical fundations of the boundary integral equation are based on the Kelvin solution and Betti's reciprocal theorem [20].

Let P and Q be two arbitrary points in an infinte elastic body as shown in Fig 2.1. A unit concentrated load acting at point P in i direction is defined as

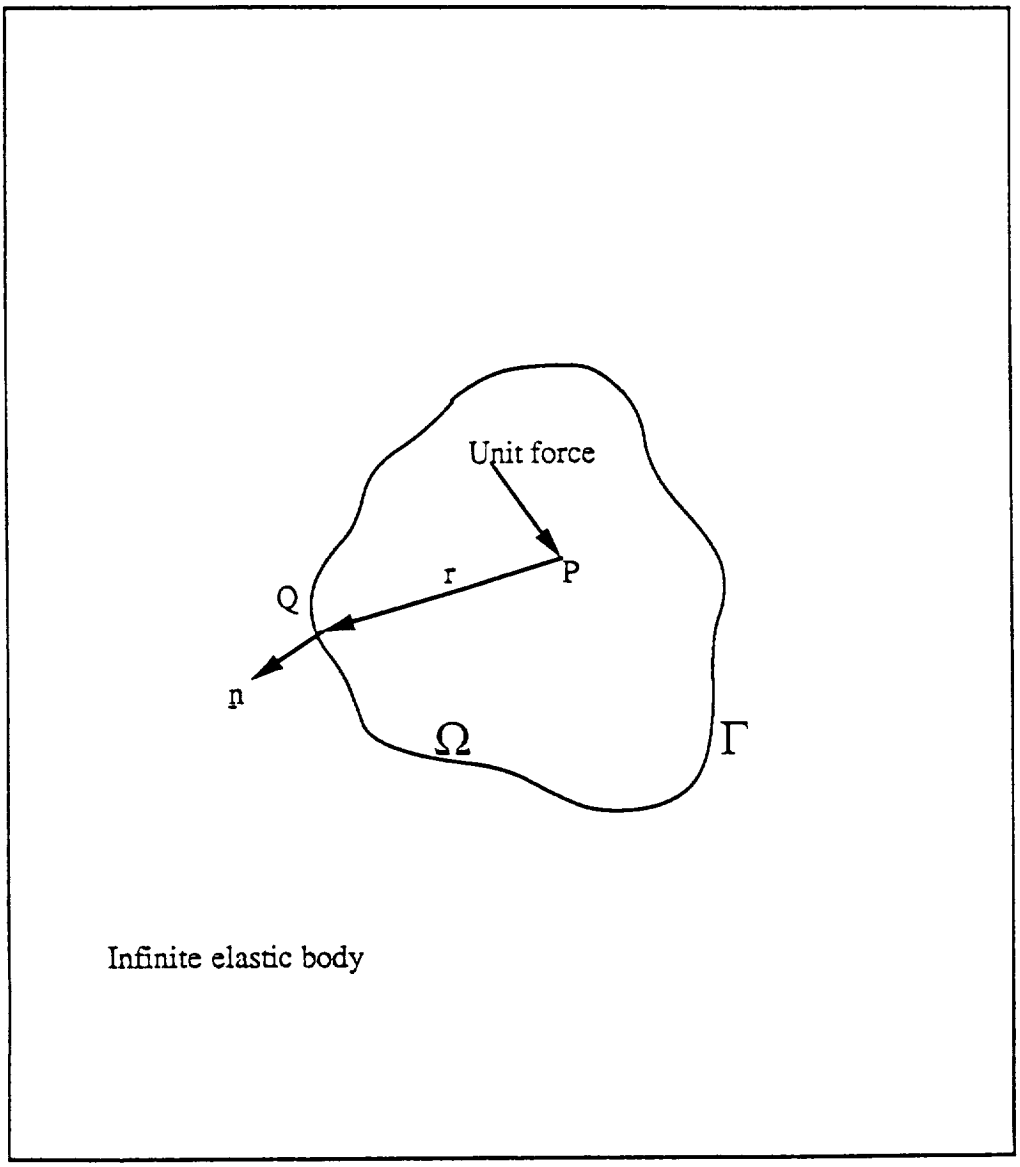

Figure 2.1 Domain and Boundary Geometry

$$f_i(P,Q) = \delta(P,Q)\, e_i$$

where e_i is the unit vector in i direction and $\delta(P,Q)$ is the Dirac delta function which is defined as a function that is equal to zero for Q does not coincide with P and becomes infinite when P=Q in such manner that

$$\int_{\Omega} \delta(P,Q)\, d\Omega(Q) = 1$$

for any point P which lies in domain Ω. The displacement in direction j at point Q due to a unit concentrated load applied in direction i at point P in an infinte linear elastic body is given by Kelvin's solution [21]

$$u_j = U_{ij}(P,Q)\, e_i \tag{2.1}$$

where

$$U_{ij}(P,Q) = \frac{1}{16\pi\mu(1-\nu)r}\, [\,(3-4\nu)\delta_{ij} + r_{,i}r_{,j}] \tag{2.2}$$

and e_i is the component of the unit base vector in direction i, μ is shear modulus, ν

is Poisson's ratio, and r is the distance between point P and point Q. Note that

$$r=\left[(x_i^Q-x_i^P)(x_i^Q-x_i^P)\right]^{1/2} \tag{2.3}$$

and

$$r_{,i}=\frac{\partial r}{\partial x_i} = \frac{(x_i^Q-x_i^P)}{r}$$

$$r_{,ij} = \frac{\partial^2 r}{\partial x_j \partial x_i} = \frac{1}{r} \left(\delta_{ij} - r_{,i} r_{,j} \right) \tag{2.4}$$

where δ_{ij} is the Kronecker delta which is equal to 1 when i = j and 0 when $i \neq j$ and comma i denotes partial differentiation with respect to direction x_i. Cartesian tensor notation is used hereinafter with all the subscripts ranging from 1 to 3 and the convention that repeated indices are summed is employed. The stress-strain relation for an isotropic linear elastic material is [22]

$$\sigma_{jk} = 2\mu \, \varepsilon_{jk} + \lambda \delta_{jk} \, \varepsilon_{nn} \tag{2.5}$$

and the strain-displacement relation is

$$\varepsilon_{jk} = \frac{1}{2}\left(u_{j,k} + u_{k,j} \right) \tag{2.6}$$

The stress-displacement relationship for an isotropic elastic material are obtained by substituting Eq.2.6 into Eq.2.5, i.e.

$$\sigma_{jk} = \lambda\delta_{jk}u_{m,m} + \mu\left(u_{j,k} + u_{k,j}\right) \tag{2.7}$$

where $\lambda = \dfrac{\nu E}{(1+\nu)(1-2\nu)}$, and E is Young's Modulus

Substituting Eq.2.1 into Eq.2.7, the stress field can be obtained as

$$\begin{aligned} D_{ijk}(P,Q) &= \lambda\delta_{jk}\, U_{im,m}(P,Q) + \mu\left(U_{ij,k}(P,Q) + U_{ik,j}(P,Q)\right) \\ &= \frac{-1}{8\pi(1-\nu)r^2}\left\{(1-2\nu)(r_{,j}\delta_{ki} + r_{,k}\delta_{ij} - r_{,i}\delta_{jk}) + 3r_{,i}r_{,j}r_{,k}\right\} \end{aligned} \tag{2.8}$$

where $D_{ijk}(P,Q)$ is interpreted as the stress component σ_{jk} at point Q due to a unit load in the i direction at point P. If point Q is put on the boundary Γ of a finite body with domain Ω cut out from the infinite body,as shown in Fig.2.1, the tractions at point Q on the surface can be determined as

$$t_j = \sigma_{jk} n_k \tag{2.9}$$

where n_k is the k_{th} component of the outward normal to the surface at point Q. Substitution of Eq.2.8 into Eq.2.9 leads to

$$\begin{aligned} T_{ij}(P,Q) &= D_{ijk}(P.Q)n_k(Q) \\ &= \frac{1}{8\pi(1-\nu)r^2}\left\{(1-2\nu)(n_j r_{,i} - n_i r_{,j}) - n_k r_{,k}\left[(1-2\nu)\delta_{ij} + 3r_{,i}r_{,j}\right]\right\} \end{aligned} \tag{2.10}$$

where $T_{ij}(P,Q)$ is the traction at point Q in direction j on the surface with outward normal n_k due to a unit load in direction i at point P. The free body cut out from the infinite body forms an equilibrium state subjected to the concentrated unit force $f_j(P,Q)$ and the boundary tractions $T_{ij}(P,Q)e_i$ with the corresponding boundary displacement $U_{ij}(P,Q)e_i$. Betti's reciprocal theorem can now be applied to derive the boundary integral equation. Suppose that there are two generalized force

systems. The first system includes body forces b_j, surface tractions t_j and displacements u_j , and the second one consists of body forces b_j^*, boundary tractions t_j^* and displacements u_j^*. If these two systems act simultaneously on a linear elastic body with domain Ω enveloped by the boundary surface Γ, Betti's reciprocal theorem states that [23]

$$\int_{\Gamma} t_j u_j^* d\Gamma + \int_{\Omega} b_j u_j^* d\Omega = \int_{\Gamma} t_j^* u_j d\Gamma + \int_{\Omega} b_j^* u_j d\Omega \tag{2.11}$$

That is, the work done by the forces of the first system with the displacements of the second system is equal to the work performed by the forces of the second system on the displacements produced by the first system. Now let the first system be the one we are seeking a solution to with the assumption that the body forces are neglected and let the second system correspond to the fundamental solutions for the traction and displacement due to a unit concentrated load f_j in an infinite body, as shown in Fig.2.2. That is,

$$\begin{aligned} b_j &= 0 \\ t_j &= t_j(Q) \\ u_j &= u_j(Q) \\ b_j^* &= f_j = \delta(P,Q)\, e_j \\ t_j^* &= T_{ij}(P,Q)\, e_i \\ u_j^* &= U_{ij}(P,Q)\, e_i \end{aligned} \tag{2.12}$$

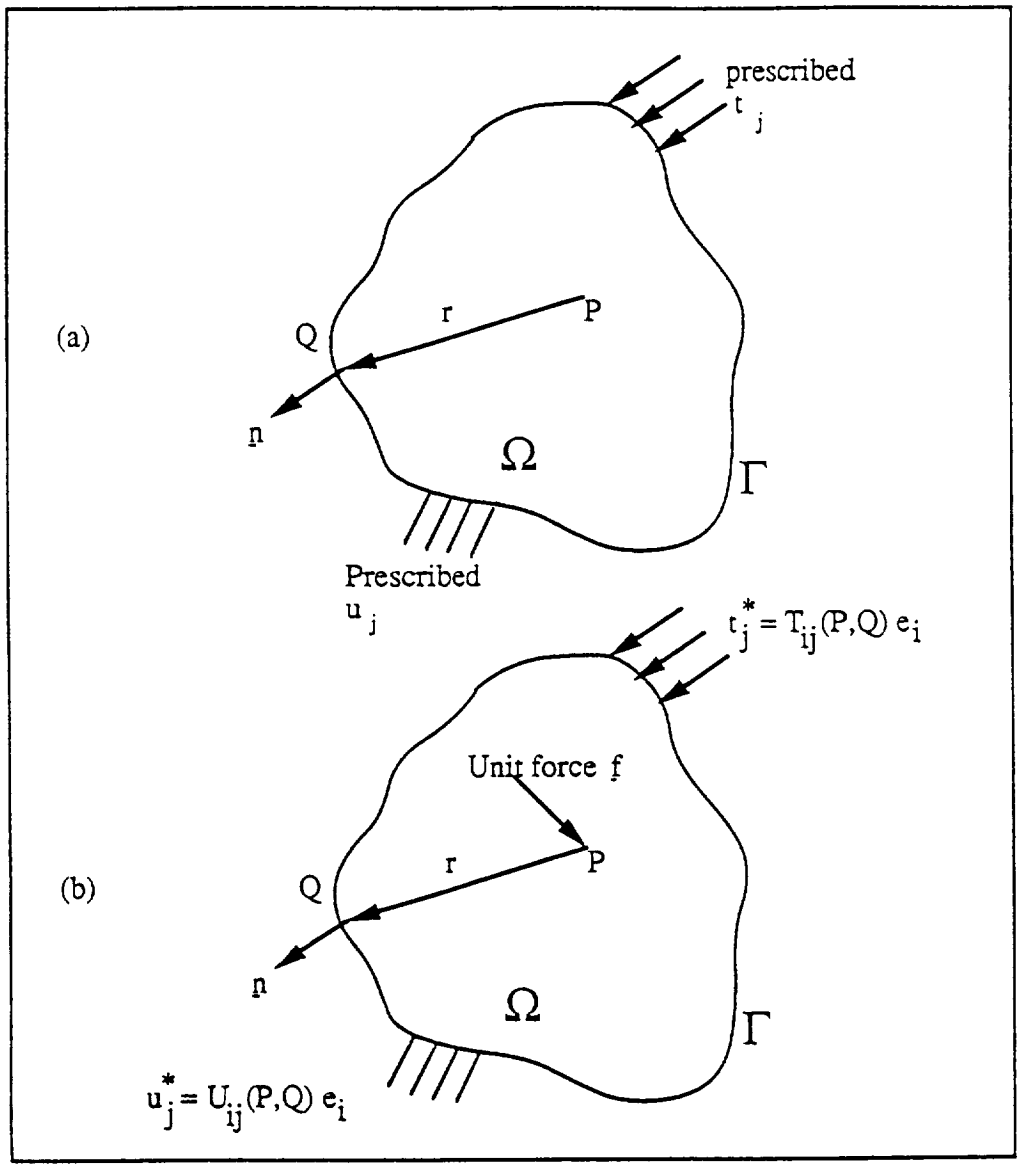

Figure 2.2 Generalized Force Systems: (a) First System with Traction t_j and Displacement u_j (b) Second System of Kelvin's Solution

Substitution of Eq.2.12 into Eq.2.11, leads to the following equation

$$\int_{\Gamma} U_{ij}(P,Q)t_j(Q)e_i d\Gamma(Q) = \int_{\Gamma} T_{ij}(P,Q)u_j(Q)e_i d\Gamma(Q) + \int_{\Omega} \delta(P,Q)e_j u_j(Q)d\Omega(Q) \tag{2.13}$$

Noting that

$$\int_{\Omega} \delta(P,Q)e_j u_j(Q)d\Omega(Q) = u_j(P)\, e_j = u_j(P)\delta_{ij}\, e_i \tag{2.14}$$

and using Eq.2.14, Eq.2.13 can be rewritten as

$$\int_{\Gamma} U_{ij}(P,Q)t_j(Q)d\Gamma(Q)e_i = \int_{\Gamma} T_{ij}(P,Q)u_j(Q)d\Gamma(Q)e_i + \delta_{ij}u_j(P)e_i \tag{2.15}$$

or

$$\delta_{ij}u_j(P) = \int_\Gamma U_{ij}(P,Q)t_j(Q)d\Gamma(Q) - \int_\Gamma T_{ij}(P,Q)u_j(Q)d\Gamma(Q) \qquad (2.16)$$

So far the point P is inside the boundary Γ. In order to have the equation relate only the points on the boundary surface Γ, we need to move the point P toward the surface. However, due to the singular nature of the kernels $U_{ij}(P,Q)$ and $T_{ij}(P,Q)$ as r tends to zero, a limiting process must be employed in order to obtain the boundary integral equation. Let us first choose a new boundary

$$\Gamma_n = \Gamma_- + \Gamma_\varepsilon$$

where Γ_ε is a surface of semi-spheric shape and Γ_- is the rest of the surface as shown in Fig.2.3. Γ_ε should envelop the point P such that P is still in domain Ω and thus Eq.2.16 is still available. With the new boundary, Eq.2.16 now becomes

$$\begin{aligned}\delta_{ij}u_j(P) = &\int_{\Gamma_-} U_{ij}(P,Q)t_j(Q)d\Gamma(Q) + \int_{\Gamma_\varepsilon} U_{ij}(P,Q)t_j(Q)d\Gamma(Q) \\ &- \int_{\Gamma_-} T_{ij}(P,Q)u_j(Q)d\Gamma(Q) - \int_{\Gamma_\varepsilon} T_{ij}(P,Q)u_j(Q)d\Gamma(Q) \qquad (2.17)\end{aligned}$$

As ε tends to zero, the boundary Γ_ε becomes the original boundary Γ. We also note that when point Q is within the region Γ_ε we have

$$d\Gamma(Q) = \varepsilon^2 \sin\theta \, d\theta \, d\phi$$

$$r = \varepsilon$$

$$r_{,i} = n_i$$

$$\tilde{n} = \begin{Bmatrix} \sin\theta \cos\phi \\ \sin\theta \sin\phi \\ \cos\theta \end{Bmatrix}$$

$$n_k r_{,k} = 1$$

$$r_{,i} n_j - r_{,j} n_i = 0$$

$$t_j(Q) = t_j(P) \text{ and } u_j(Q) = u_j(P) \qquad (2.18)$$

where $t_j(P)$ and $u_j(P)$ are the tractions and displacements at point P which are constants over the surface of the sphere as ε tends to be zero. Substituting these relations into Eq.2.17, the second term on the right hand side of Eq.2.17 becomes

$$\int_{\Gamma_\varepsilon} U_{ij}(P,Q) t_j(Q) d\Gamma(Q) = \int_0^{\bar{\phi}} \int_0^{\bar{\theta}} \frac{1}{16\pi\mu(1-\nu)\varepsilon} \left[(3-4\nu)\delta_{ij} + n_i n_j\right] \varepsilon^2 \sin\theta d\theta d\phi t_j(P)$$

$$= \frac{\varepsilon t_j(P)}{16\pi\mu(1-\nu)} \int_0^{\bar{\phi}} \int_0^{\bar{\theta}} \left[(3-4\nu)\delta_{ij} + n_i n_j\right] \sin\theta d\theta d\phi \qquad (2.19)$$

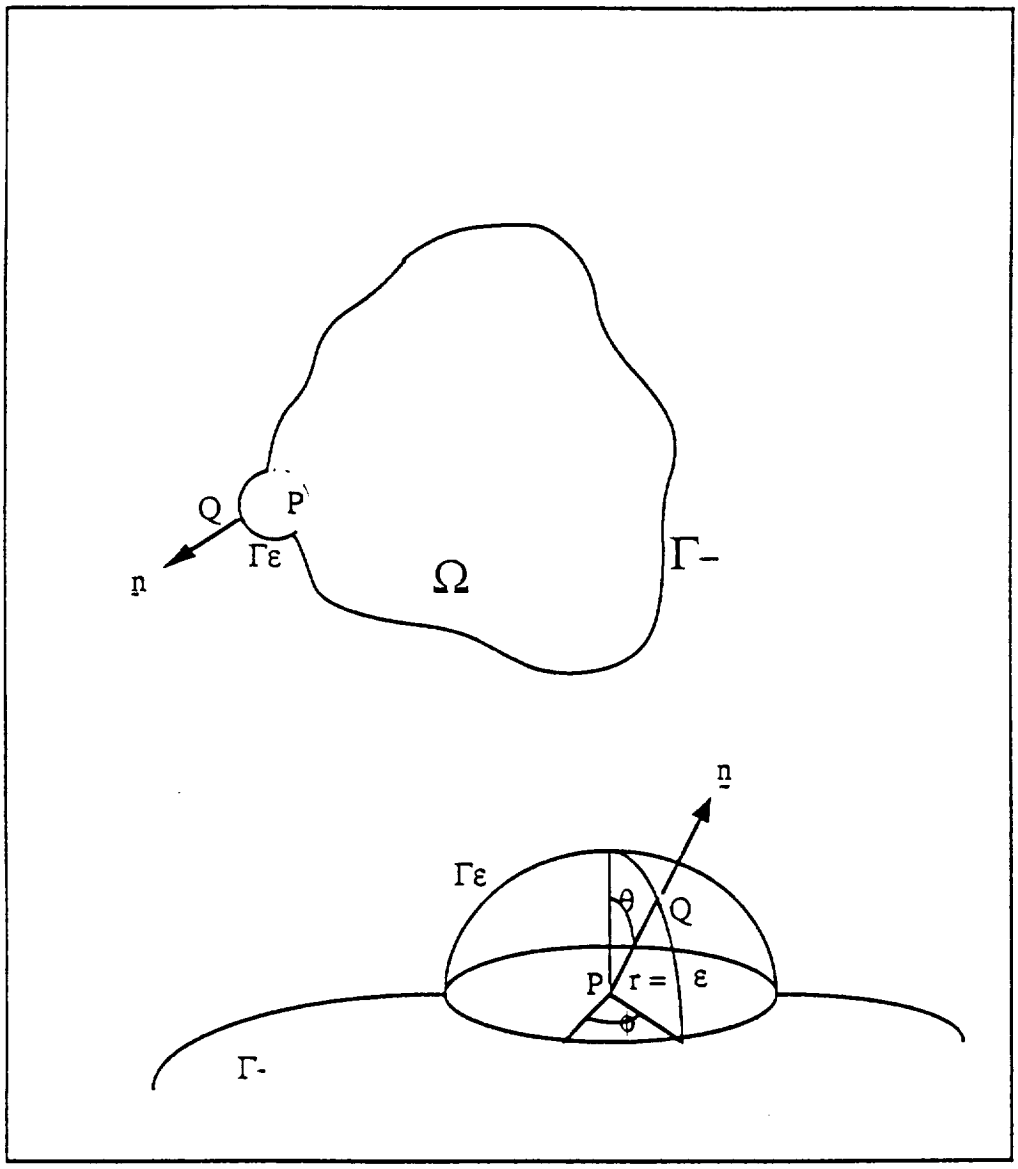

Figure 2.3 Domain and Boundary Used for Limiting Process

As $\varepsilon \rightarrow 0$, the limit of the second integral on the right hand side of Eq. 2.17 becomes

$$\lim_{\varepsilon \rightarrow 0} \int_{\Gamma_\varepsilon} U_{ij}(P,Q)t_j(Q)d\Gamma(Q) = 0 \qquad (2.20)$$

The integral of Eq.2.19 is no longer singular and thus Eq.2.20 tends to be zero as ε is approaching zero. As for the fourth term on the right hand side of Eq. 2.17

$$\int_{\Gamma_\varepsilon} T_{ij}(P,Q)u_j(Q)d\Gamma(Q) = \int_0^{\bar{\phi}} \int_0^{\bar{\theta}} \frac{-1}{8\pi(1-\nu)\varepsilon^2} [(1-2\nu)\delta_{ij} + 3n_i n_j]\varepsilon^2 \sin\theta d\theta d\phi u_j(P)$$

$$= \frac{-u_j(P)}{8\pi(1-\nu)} \int_0^{\bar{\phi}} \int_0^{\bar{\theta}} \left[(1-2\nu)\delta_{ij} + 3n_i n_j\right] \sin\theta d\theta d\phi \qquad (2.21)$$

Substituting Eq.2.18 into Eq.2.21 leads to a matrix expression for the kernel inside the integration and taking the limit as ε approaching zero

$$\lim_{\varepsilon \to 0} \int_0^{\bar{\phi}} \int_0^{\bar{\theta}} T_{ij}(P,Q) u_j(Q) ds(Q)$$

$$= \frac{-u_j(P)}{8\pi(1-\nu)} \int_0^{\bar{\phi}} \int_0^{\bar{\theta}} \begin{bmatrix} (1-2\nu)+3\sin^2\theta\cos^2\phi, & \sin^2\theta\sin\phi\cos\phi, & \sin\theta\cos\theta\cos\phi \\ \sin^2\theta\sin\phi\cos\phi, & (1-2\nu)+3\sin^2\theta\sin^2\phi, & \sin\theta\cos\theta\ \sin\phi \\ \sin\theta\cos\theta\cos\phi, & \sin\theta\cos\theta\sin\phi, & (1-2\nu)+\ 3\cos^2\theta \end{bmatrix} \begin{bmatrix} u_1(P) \\ u_2(P) \\ u_3(P) \end{bmatrix} \sin\theta d\theta d\phi \qquad (2.22)$$

The integral ranges will depend on the local geometry of the point P. If point P lies on a smooth surface,

$$\bar{\theta} = \frac{\pi}{2} \quad \text{and} \quad \bar{\phi} = 2\pi$$

and each term inside the matrix in Eq.2.22 becomes

$$\lim_{\varepsilon \to 0} \int_{\Gamma_\varepsilon} T_{ij}(P,Q) u_j(Q) d\Gamma(Q) = \begin{bmatrix} \frac{-1}{2}, & 0, & 0 \\ 0, & \frac{-1}{2}, & 0 \\ 0, & 0, & \frac{-1}{2} \end{bmatrix} \begin{bmatrix} u_1(P) \\ u_2(P) \\ u_3(P) \end{bmatrix} \qquad (2.23)$$

or in Cartesian tensor form

$$\lim_{\varepsilon \to 0} \int_{\Gamma_\varepsilon} T_{ij}(P,Q) u_j(Q) d\Gamma(Q) = \frac{-1}{2} \delta_{ij} u_j(P) \tag{2.24}$$

Substituting Eq.2.20 and Eq.2.24 into Eq.2.17 leads to the boundary integral equation for P lying on a smooth surface

$$\frac{1}{2} \delta_{ij} u_j(P) = \int_\Gamma U_{ij}(P,Q) t_j(Q) d\Gamma(Q) - \int_\Gamma T_{ij}(P,Q) u_j(Q) d\Gamma(Q) \tag{2.25}$$

If P is not on a smooth surface, the boundary integral equation is

$$C_{ij}(P) u_j(P) = \int_\Gamma U_{ij}(P,Q)\, t_j(Q)\, d\Gamma(Q) - \int_\Gamma T_{ij}(P,Q)\, u_j(Q)\, d\Gamma(Q) \tag{2.26}$$

where

$$C_{ij}(P)u_j(P) = \delta_{ij} + \lim_{\varepsilon \to 0} \int_{\Gamma_\varepsilon} T_{ij}(P,Q)d\Gamma(Q) \qquad (2.27)$$

which is only a function of the local geometry in the vicinity of point P. The integration in Eq.2.27 can be carried out by using Eq.2.22 with the appropriate integral range according to the local configuration of point P. The $C_{ij}(P,Q)$ can also be calculated from the concept of rigid body motion[24]. When the body undergose a rigid body translation, the surface is free of traction and the displacement is an arbitrary constant. By setting

$$t_j(Q) = 0$$

$$u_j(Q) = \text{constant}$$

Eq.2.26 becomes

$$C_{ij}(P) = -\int_{\Gamma} T_{ij}(P,Q)\, d\Gamma(Q) \qquad (2.28)$$

Comparing Eq.2.27 and Eq.2.28, it is apparent that the former depends on the local

geometry of each point and is different point to point. Thus it is very tedious to calculate. On the other hand, the latter is an integration on the whole boundary surface with a different kernel function and is easy to calculate for different points on the boundary. In fact, Eq.2.28 is merely a by-product of the second term on the right hand side of Eq.2.26 when it is carried out by numerical integration method. Therefore, with little effort, the term $C_{ij}(P)$ can be easily obtained. Eq.2.28 is thus adopted in this paper to calculate the $C_{ij}(P)$ term.

Eq.2.26 is also known as Somigliana's identity for three dimensional linear elastostatics with zero body force. In a well-posed boundary value problem, either traction or displacement in a direction on a boundary will be prescribed. Therefore, any corresponding unknown value on the boundary can be solved by the boundary integral equation of Eq.2.26.

After the unknown boundary tractions and/or displacements have been solved, the displacement of any point inside the body can be solved by Eq.2.16 from the boundary data. In order to obtain the stresses for the interior points, Eq.2.16 is differentiated and substituted into Eq.2.7. This results in

$$\sigma_{jk}(P) = \int_{\Gamma} D_{ijk}(P,Q)t_i(Q)d\Gamma(Q) - \int_{\Gamma} S_{ijk}(P,Q)u_i(Q)d\Gamma(Q) \qquad (2.29)$$

where

$$D_{ijk}(P,Q) = \lambda\delta_{jk}U_{im,m}(P,Q) + \mu[U_{ij,k}(P,Q) + U_{ik,j}(P,Q)]$$

$$= \frac{-1}{8\pi(1-\nu)r^2}\left[(1-2\nu)(r_{,j}\delta_{ki} + r_{,k}\delta_{ij} - r_{,i}\delta_{jk}) + 3\, r_{,i}r_{,j}r_{,k}\right] \qquad (2.30)$$

and

$$S_{ijk}(P,Q) = \lambda\delta_{jk}T_{im,m}(P,Q) + \mu[T_{ij,k}(P,Q) + T_{ik,j}(P,Q)]$$

$$= \frac{E}{8\pi(1-\nu^2)r^3}\{\, 3n_m r_{,m}[(1-2\nu)r_{,i}\delta_{jk} + \nu(r_{,j}\delta_{ki} + r_{,k}\delta_{ij}) - 5\, r_{,i}r_{,j}r_{,k}]$$

$$+3\nu(n_j r_{,k} + n_k r_{,j})r_{,i} + (1-2\nu)(3n_i r_{,j}r_{,k} + n_j\delta_{ki} + n_k\delta_{ij})$$

$$- (1-4\nu)n_i\delta_{jk}\,\} \qquad (2.31)$$

2.3 Numerical Implementation of Boundary Integral Equation

Owing to the difficulties of solving the boundary integral equation in closed form for practical problems with complicated geometries and boundary conditions, it is necessary to solve the boundary integral equation numerically.

The procedures for obtaining a numerical solution of the three dimensional boundary integral equation starts out with a discretization of the boundary surface Γ into m piecewise isoparametric surface elements. Such elements have been well developed for the Finite Element Method [25]. Each element consists of n_m nodes, the number depending on what kind of interpolation is employed in each element. The elements implemented in the present work include three-node linear triangular elements, four-node linear quadrilateral elements, six-node quadratic triangular elements, and eight-node quadratic quadrilateral elements. The shape functions for the isoparametric elements are derived in Appendix A. The cartesian coordinate of each node is given by

$$x_i = \sum_{\alpha=1}^{n_m} N^{\alpha}(\xi)\, x_i^{\alpha} \tag{2.32}$$

where x_i^{α} is the i - Cartesian coordinate of node α, $N^{\alpha}(\xi)$ is the shape function for node α which is a polynominal function of intrinsic coordinates $\xi = (\xi_1, \xi_2)$. Eq.2.32 represents a one-to-one mapping of any point on the element from the

three dimensional Catesian coordinate space into the two dimensional (ξ_1, ξ_2) coordinate system, as shown in Fig.2.4. The isoparametric elements also use identical shape function to interpolate any function on the element, such as the displacements and tractions in the Boundary Element Method. Symbolically,

$$u_i = \sum_{\alpha=1}^{n_m} N^{\alpha}(\xi)\, u_i^{\alpha}$$

$$t_i = \sum_{\alpha=1}^{n_m} N^{\alpha}(\xi)\, t_i^{\alpha} \qquad (2.33)$$

where u_i^{α}, t_i^{α} are the nodal values of displacement and tractions, respectively. By discretizing the surface Γ into m segments and utilizing the shape function, Eq.2.26 becomes

$$C_{ij}^{P}\, u_j^{P} = \sum_{l=1}^{m} \sum_{\alpha=1}^{n_m} \int_{\Gamma_l} U_{ij}(P,Q(\xi)) N^{\alpha}(\xi) J_l(\xi) d\Gamma(\xi)\, t_j^{\alpha l}$$

$$- \sum_{l=1}^{m} \sum_{\alpha=1}^{n_m} \int_{\Gamma_l} T_{ij}(P,Q(\xi)) N^{\alpha}(\xi) J_l(\xi) d\Gamma(\xi)\, u_j^{\alpha l} \quad , \text{ P not summed} \qquad (2.34)$$

where C_{ij}^{P} and u_j^{P} stand for the coefficients C_{ij} and displacement in j-direction of nodal point P, respectively. The integral over the whole surface is carried out by summing up the integral over each element surface Γ_l. The $t_i^{\alpha l}$ and $u_i^{\alpha l}$ is the

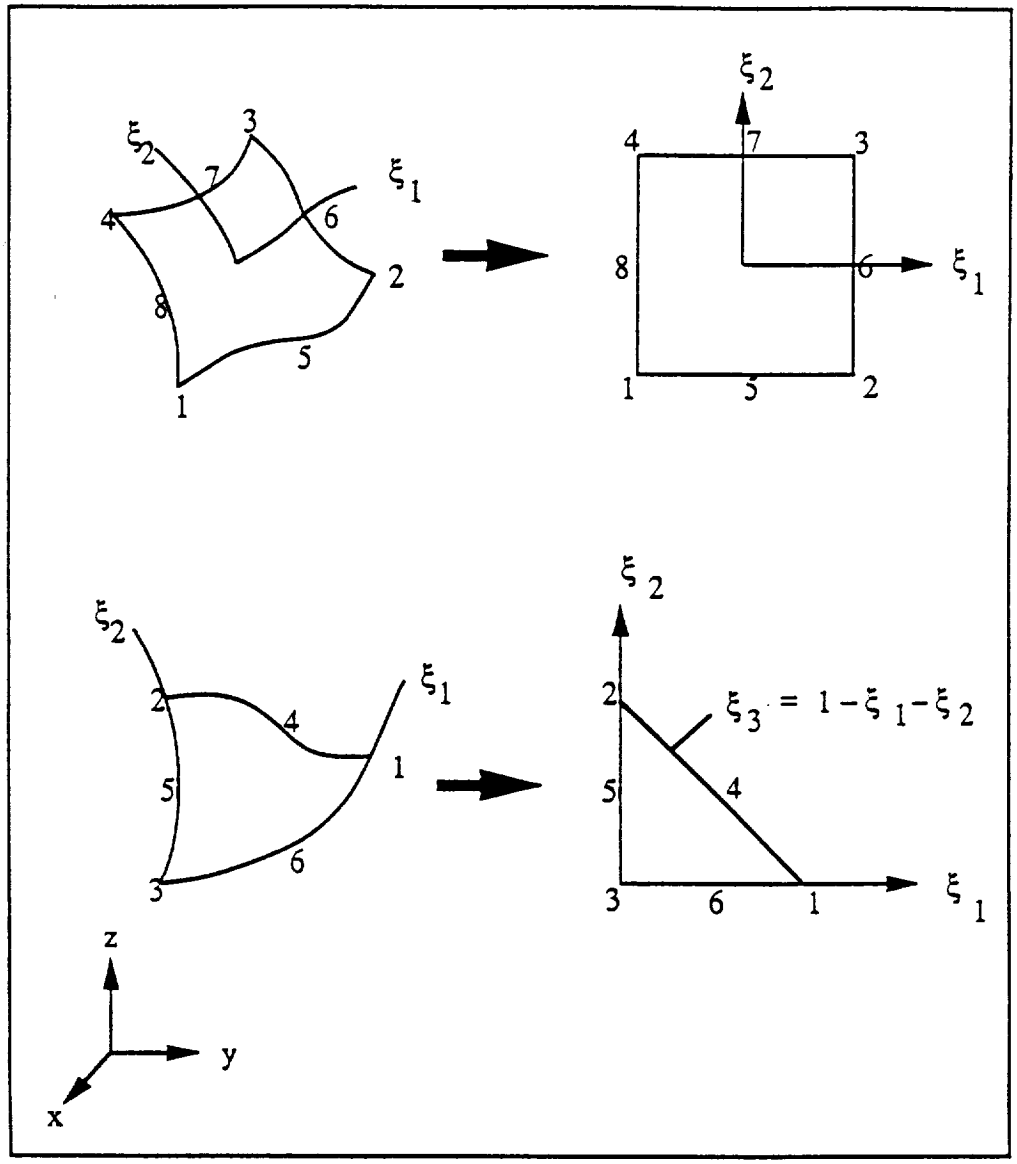

Figure 2.4 Mapping of Isoparametric Elements

traction and displacement in i-direction of node α in element l. The term $J_l(\xi)$ is the determinant of the Jacobian matrix of element l deduced from the change of the integration variables from the Cartesian coordinate to the intrinsic ξ-coordinate system. It is found to be

$$J_l(\xi) = \left| \frac{\partial x_i}{\partial \xi_j} \right| = \begin{vmatrix} \frac{\partial x_1}{\partial \xi_1}, \frac{\partial x_1}{\partial \xi_2} \\ \frac{\partial x_2}{\partial \xi_1}, \frac{\partial x_2}{\partial \xi_2} \end{vmatrix} = \begin{vmatrix} \sum_{\alpha=1}^{n_m} \frac{\partial N^\alpha(\xi_1,\xi_2)}{\partial \xi_1} x_1^{\alpha l}, \sum_{\alpha=1}^{n_m} \frac{\partial N^\alpha(\xi_1,\xi_2)}{\partial \xi_2} x_1^{\alpha l} \\ \sum_{\alpha=1}^{n_m} \frac{\partial N^\alpha(\xi_1,\xi_2)}{\partial \xi_1} x_2^{\alpha l}, \sum_{\alpha=1}^{n_m} \frac{\partial N^\alpha(\xi_1,\xi_2)}{\partial \xi_2} x_2^{\alpha l} \end{vmatrix}$$

(2.35)

Similary, Eq.2.28 is rewritten as

$$C_{ij}^P = -\sum_{l=1}^{m} \int_{\Gamma_l} T_{ij}(P,Q(\xi)) J_l(\xi) d\Gamma(\xi) \qquad (2.36)$$

A Gaussian quadrature scheme can now be applied to accomplish the integration. For the case when the point P is not on the element which is being integrated over, the Gaussian quadrature is straight forward, that is,

$$\int_{\Gamma_l} \Psi_l(P,\xi)d\Gamma(\xi) = \sum_{a=1}^{n_a}\sum_{b=1}^{n_b} w_1^a w_2^b \Psi_l(P,\xi_1^a,\xi_2^b) \qquad (2.37)$$

where

$$\Psi_l(P,\xi) = U_{ij}(P,Q(\xi))N^{\alpha}(\xi)J_l(\xi)$$

or

$$\Psi_l(P,\xi) = T_{ij}(P,Q(\xi))N^{\alpha}(\xi)J_l(\xi)$$

In Eq.2.37 n_a and n_b are the order of Gaussian quadrature and $w_1{}^a$ and $w_2{}^b$ are the weights of the corresponding Gaussian integration points ξ_1 , ξ_2 , respectively. When point P is one of the nodes of the element under integration, the standard Gaussian quadrature will not give accurate results because of the 1/r and $1/r^2$ singularities of $U_{ij}(P,Q)$ and $T_{ij}(P,Q)$, respectively. Therefore, special treatment of this singular integral must be used in order to obtain an accurate solution. The method employed here follows the work of Rizzo and Shippy [15]. The element is divided into triangles according to the position of the point P as shown in Appendix B. Inside each triangle, the ξ-coordinate system is transformed into a local polar coordinate system , r and θ, and the $d\xi$ term in the integral becomes $rdrd\theta$. The additional r due to this transformation eliminates the 1/r singularity of the kernel $U_{ij}(P,Q)$. Gaussian quadrature can then be applied to the polar coordinate system. Of course, one more transformation is needed to map the r,θ coordinate system to another polar coordinate system $\underline{r}$ and $\underline{\theta}$ so that the range

varies from -1 to 1. The details of the procedures are illustrated in Appendix B. For the integration of the kernel $T_{ij}(P,Q)$, a 1/r singularity remains after the transformation from the ξ-coordinate to the polar coordinate. However, by substituting Eq.2.36 into Eq.2.34, Eq.2.34 can be rewritten as

$$-\sum_{l=1}^{n_m}\int_{\Gamma_l} T_{ij}(P,Q(\xi))J_l(\xi)d\Gamma(\xi)\,u_j^P$$

$$=\sum_{l=1}^{m}\sum_{\alpha=1}^{n_m}\int_{\Gamma_l} U_{ij}(P,Q(\xi))N^{\alpha}(\xi)t_j^{\alpha l}J_l(\xi)d\Gamma(\xi) - \sum_{l=1}^{m}\sum_{\alpha=1}^{n_m}\int_{\Gamma_l} T_{ij}(P,Q(\xi))N^{\alpha}(\xi)u_j^{\alpha l}J_l(\xi)d\Gamma(\xi) \tag{2.38}$$

Distinguish the elements containing point P from those elements without point P for the integration involving the kernel $T_{ij}(P,Q)$, and Eq.2.38 becomes

$$-\sum_{l=1}^{m^x}\int_{\Gamma_l} T_{ij}(P,Q(\xi))J_l(\xi)d\Gamma(\xi)u_j^P$$

$$=\sum_{l=1}^{m}\sum_{\alpha=1}^{n_m}\int_{\Gamma_l} U_{ij}(P,Q(\xi))N^{\alpha}(\xi)t_j^{\alpha l}J_l(\xi)d\Gamma(\xi) - \sum_{l=1}^{m^x}\sum_{\alpha=1}^{n_m}\int_{\Gamma_l} T_{ij}(P,Q(\xi))N^{\alpha}(\xi)u_j^{\alpha l}J_l(\xi)d\Gamma(\xi)$$

$$-\sum_{l=1}^{m^p}\sum_{\alpha=1}^{n_m}\int_{\Gamma_l} T_{ij}(P,Q(\xi))N^{\alpha}(\xi)u_j^{\alpha l}J_l(\xi)d\Gamma(\xi)+\sum_{l=1}^{m^p}\int_{\Gamma_l} T_{ij}(P,Q(\xi))J_l(\xi)d\Gamma(\xi)\,u_j^P \tag{2.39}$$

where m_x is the total number of the elements excluding point P and m_p is the total number of the elements including point P. Obviously, $m = m_x + m_p$. Combining the last two terms on the right hand side of Eq.2.39, results in

$$\overline{C}_{ij}^{P} u_j^P =$$

$$\sum_{l=1}^{m} \sum_{\alpha=1}^{n_m} \int_{\Gamma_l} U_{ij}(P,Q(\xi)) N^{\alpha}(\xi) J_l(\xi) d\Gamma(\xi) t_j^{\alpha l} - \sum_{l=1}^{m_x} \sum_{\alpha=1}^{n_m} \int_{\Gamma_l} T_{ij}(P,Q(\xi)) N^{\alpha}(\xi) J_l(\xi) d\Gamma(\xi) u_j^{\alpha l}$$

$$- \sum_{l=1}^{m_p} \sum_{\alpha=1}^{n_m} \int_{\Gamma_l} T_{ij}(P,Q(\xi)) (N^{\alpha}(\xi) - \delta_{\alpha P}) J_l(\xi) d\Gamma(\xi) u_j^{\alpha l} \qquad (2.40)$$

where

$$\overline{C}_{ij}^{P} = - \sum_{l=1}^{m_x} \int_{\Gamma_l} T_{ij}(P,Q(\xi)) d\Gamma(\xi) \qquad (2.41)$$

Eq.2.41 is the negative of the integral of the kernel $T_{ij}(P,Q)$ over the elements which do not contain the point P, hence, Eq.2.41 is no longer singular. As for Eq.2.40, the remaining 1/r singularity of the kernel $T_{ij}(P,Q)$ is removed by the special shape function $N^{\alpha}(\xi) - \delta_{\alpha P}$ in the last term on the right hand side of equation because when α coincides with point P ,the constant term is eliminated

and thus the smallest order of the shape function is of order r. This additional r can cancel the 1/r singularity after the coordinate has been transformed into the local polar coordinate. Using this procedures all the singularities are eliminated and Gaussian quadrature can be used.

Eq.2.40 represents an equation at each discrete point P on the boundary surface constraining the boundary displacements and boundary tractions in the i-direction. For a surface including N nodes, Eq.2.40 can be expressed as

$$\bar{C}_{ij}^{P} u_j^{P} + \left[\underline{T}_{ij}^{1}, \underline{T}_{ij}^{2}, \ldots\ldots \underline{T}_{ij}^{N} \right] \begin{Bmatrix} u_j^1 \\ u_j^2 \\ \vdots \\ u_j^N \end{Bmatrix} = \left[\underline{U}_{ij}^{1}, \underline{U}_{ij}^{2}, \ldots\ldots, \underline{U}_{ij}^{N} \right] \begin{Bmatrix} t_j^1 \\ t_j^2 \\ \vdots \\ t_j^N \end{Bmatrix} \qquad (2.42)$$

where each term of $\underline{T}_{ij}^{n}$ for node n is the integration summed up from the contribution of the elements which share the same node n. The same applies for $\underline{U}_{ij}^{n}$. Eq.2.42 can be rewritten as

$$\bar{C}_{ij}^{P} u_j^{P} + \sum_{n=1}^{N} \underline{T}_{ij}^{n} u_j^{n} = \sum_{n=1}^{N} \underline{U}_{ij}^{n} t_j^{n} \qquad (2.43)$$

This equation can be expressed more simply by combining the first term into the summation on the left hand side, i.e.,

$$\sum_{n=1}^{N} T_{ij}^{*n} u_j^n = \sum_{n=1}^{N} U_{ij}^{*n} t_j^n \tag{2.44}$$

where

$$T_{ij}^{*n} = \underline{T}_{ij}^n \qquad \text{for } n \neq P$$

$$T_{ij}^{*n} = \underline{T}_{ij}^n + \overline{C}_{ij}^P \qquad \text{for } n = P \tag{2.45}$$

Another way of dealing with the singularity which is worthy to mention here is through the use of rigid body motion. For a rigid body motion in direction j, Eq.2.44 reduces to

$$\sum_{n=1}^{N} T_{ij}^{*n} = 0 \tag{2.46}$$

This indicates that the sum of T_{ij}^{*n} from each node in a row for certain direction j should be zero. Hence the value of the singular term T_{ij}^{*P} when n = P can be

easily calculated once all the other terms are known, that is,

$$T_{ij}^{*P} = -\sum_{\substack{n=1 \\ n\neq P}}^{N} T_{ij}^{*P} \tag{2.47}$$

For three dimensional problems the indices i and j range from 1 to 3. Therefore, for a surface including N nodes, the dimension of the total algebraic system of equations formed by Eq.2.44 for each node in each direction is 3Nx3N. The system can be represented in matrix form as

$$\mathbf{T^{*}u = U^{*}t} \tag{2.48}$$

The matrixes $\mathbf{T^{*}}$ and $\mathbf{U^{*}}$ are rearranged by interchanging the suitable columns on each side of equation so that all the unknown variables are contained in a column vector **x** and all the prescribed values of the boundary are included in the column **y** on the other side of the equation. Symbolically,

$$\mathbf{Ax = By = f} \tag{2.49}$$

The system of equations can now be easily solved by the Gaussian elimination method.

After all the boundary data are obtained, the displacements and stresses at interior points are solved by substituting the boundary tractions and displacements into Eq.2.16 and Eq.2.29, respectively, and using the shape functions to carry out the integration.

2.4 Subregion Technique

Since the boundary integral equation is a constraint relation between boundary tractions and boundary displacements with the kernel functions which include the term $1/r$ and $1/r^2$, any two distinct points on the boundary can not coincide. Therefore problems for which the boundary includes two contacting surfaces can not be solved by the Boundary Element Method using a single region. Partitioning the whole boundary into subregions is necessary to deal with such problems.

Consider for simplicity the case where the body is partitioned into two subregions. Similar procedures can be followed to separate the body into more than two regions. A body with domain Ω surrounded by the boundary Γ is partitioned into two subregions; one consists of domain Ω_1 and boundary Γ_1 and the other possesses the domain Ω_2 and boundary Γ_2, as was shown in Fig.2.5. The two regions share the same interface Γ_i. Each subregion can be treated as an independent body. Thus the procedure described in Section 2.1 can be used to

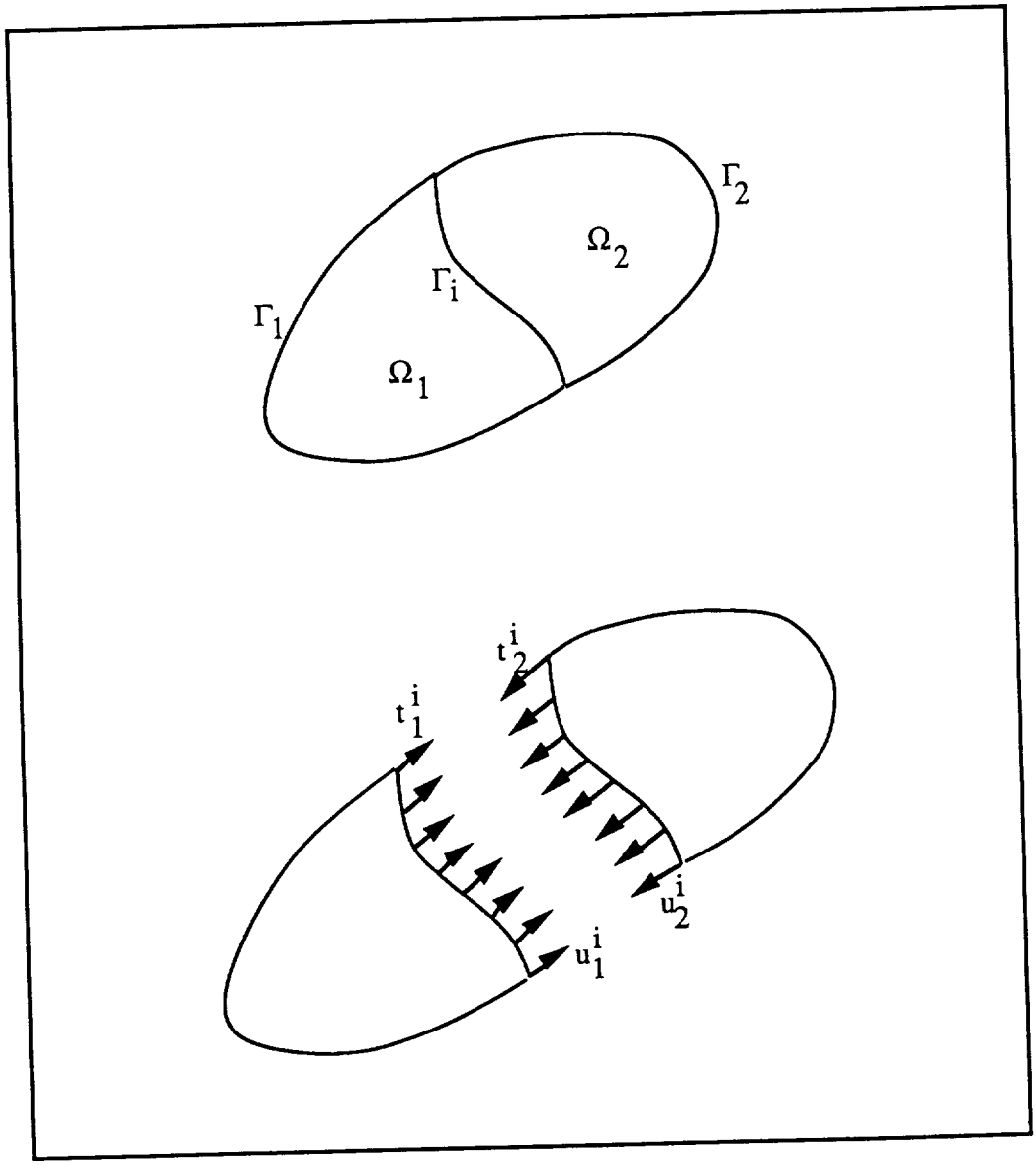

Figure 2.5 Domain Divided into Two Subregions

form the system of algebraic equations for each subregion. Before the compatibility and equilibrium conditions are enforced along the interface between two subregions, the corresponding columns of the matrix $\mathbf{U}^*$ of unknown tractions and the corresponding columns of the matrix $\mathbf{T}^*$ of known displacements in Eq.2.48 must be interchanged so that all the known and unknown variables will be at the same side of the equations. Let $\mathbf{A}_S$ and $\mathbf{B}_S$ be the kernel matrices related to the unknown column vectors $\mathbf{Uk_e}^S$ and $\mathbf{K_e}^S$ on the external surface of region s after rearrangement. Furthermore let $\mathbf{t_i}^S$, $\mathbf{u_i}^S$ be the unknown tractions and unknown displacements on the interface of region s. The system of equations for subregion one can be expressed as

$$\begin{bmatrix} A_1 \end{bmatrix} \begin{bmatrix} Uk_e^1 \\ t_i^1 \end{bmatrix} = \begin{bmatrix} B_1 \end{bmatrix} \begin{bmatrix} K_e^1 \\ u_i^1 \end{bmatrix} \tag{2.50}$$

After pre-multiplying each side by the inverse of $\mathbf{B}_1$, Eq.2.50 becomes

$$\begin{bmatrix} D_{ee}^1 & D_{ei}^1 \\ D_{ie}^1 & D_{ii}^1 \end{bmatrix} \begin{bmatrix} Uk_e^1 \\ t_i^1 \end{bmatrix} = \begin{bmatrix} K_e^1 \\ u_i^1 \end{bmatrix} \tag{2.51}$$

where $\mathbf{D}_1 = \mathbf{B}_1^{-1} \mathbf{A}_1$. By the same procedure the system for the second subregion becomes

$$\begin{bmatrix} D_{ee}^2 & D_{ei}^2 \\ D_{ie}^2 & D_{ii}^2 \end{bmatrix} \begin{bmatrix} Uk_e^2 \\ t_i^2 \end{bmatrix} = \begin{bmatrix} K_e^2 \\ u_i^2 \end{bmatrix} \tag{2.52}$$

Enforcing the compatibility and equilibrium condition along the interface

$$t_i^1 = -t_i^2 = t_i$$

$$u_i^1 = u_i^2 = u_i \tag{2.53}$$

Equations 2.51 and 2.52 can be combined to be [26]

$$\begin{bmatrix} D_{ee}^1 & D_{ei}^1 & 0 \\ D_{ie}^1 & D_{ii}^1 - D_{ii}^2 & D_{ie}^2 \\ 0 & -D_{ei}^2 & D_{ee}^2 \end{bmatrix} \begin{bmatrix} Uk_e^1 \\ t_i \\ Uk_e^2 \end{bmatrix} = \begin{bmatrix} K_e^1 \\ 0 \\ K_e^2 \end{bmatrix} \tag{2.54}$$

(2.54)

This is a system of $3(N_e^1 + N_e^2 + N_i)$ equations for $3N_e^1$ unknowns on the external surface of subregion one, $3N_e^2$ unknowns on the external boundary of subsurface two, and $3N_i$ unknown tractions on the interface. The unknown displacements on the interface can be obtained through either Eq.2.51 or Eq.2.52 after Eq.2.54 has been solved. The equation which is not used can be used as a check.

This method is simple and direct. However it is not usually adopted because the inverse of the matrix of kernel $\mathbf{B}_S$ must be calculated for both subregions. This involves a tremendous amount of computer processing time and requires a lot of memory space. Therefore, this method is not used in this paper.

An alternative procedure which eliminates the need for solving the inverse of the matrix is described herein. After the appropriate columns of $\mathbf{T}^*$ and $\mathbf{U}^*$ have been interchanged, the system of equation of the two subregions are assembled into two big matrices and two column vectors as

$$\begin{bmatrix} A^1 & 0 \\ 0 & A^2 \end{bmatrix} \begin{Bmatrix} Uk_e^1 \\ t_i^1 \\ Uk_e^2 \\ t_i^2 \end{Bmatrix} = \begin{bmatrix} B^1 & 0 \\ 0 & B^2 \end{bmatrix} \begin{Bmatrix} K_e^1 \\ u_i^1 \\ K_e^2 \\ u_i^2 \end{Bmatrix}$$

(2.55)

To be more specific,

$$\begin{bmatrix} A^1_{ee} & A^1_{ei} & 0 & 0 \\ A^1_{ie} & A^1_{ii} & 0 & 0 \\ 0 & 0 & A^2_{ee} & A^2_{ei} \\ 0 & 0 & A^2_{ie} & A^2_{ii} \end{bmatrix} \begin{bmatrix} Uk^1_e \\ t^1_i \\ Uk^2_e \\ t^2_i \end{bmatrix} = \begin{bmatrix} B^1_{ee} & B^1_{ei} & 0 & 0 \\ B^1_{ie} & B^1_{ii} & 0 & 0 \\ 0 & 0 & B^2_{ee} & B^2_{ei} \\ 0 & 0 & B^2_{ie} & B^2_{ii} \end{bmatrix} \begin{bmatrix} K^1_e \\ u^1_i \\ K^2_e \\ u^2_i \end{bmatrix} \tag{2.56}$$

Using the compatibility and equilibrium conditions (Eq.2.53), Eq.2.56 reduces to

$$\begin{bmatrix} A^1_{ee} & A^1_{ei} & 0 & B^1_{ei} \\ A^1_{ie} & A^1_{ii} & 0 & B^1_{ii} \\ 0 & -A^2_{ei} & A^2_{ee} & B^2_{ei} \\ 0 & -A^2_{ii} & A^2_{ie} & B^2_{ii} \end{bmatrix} \begin{bmatrix} Uk^1_e \\ t_i \\ Uk^2_e \\ u_i \end{bmatrix} = \begin{bmatrix} B^1_{ee} & 0 \\ B^1_{ie} & 0 \\ 0 & B^2_{ee} \\ 0 & B^2_{ie} \end{bmatrix} \begin{bmatrix} K^1_e \\ K^2_e \end{bmatrix} = \begin{bmatrix} f_1 \\ f_2 \\ f_3 \\ f_4 \end{bmatrix} \tag{2.57}$$

Since now the known variables appear on the right hand side of the equation and the unknown variables appear on the other side,the equations can be solved without

any difficulty. Although this method avoids solving for the inverse matrix and thus saves a lot of computer processing time, it still has the drawback of using two big matrices which occupy tremendous storage space. Therefore another algorithm is introduced next.

Let the numbering of the nodes along the interface be always arranged at the position following the external nodes for both subregions, as shown in Eq.2.50. Rewrite Eq.2.50 for the first region as follows

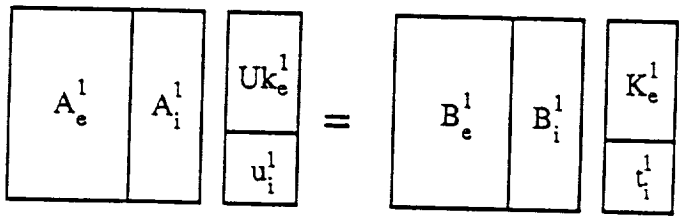

(2.58)

where the dimensions of each block are as following

A_1^e and B_1^e are $3(N_e^1 + N_i) \times 3N_e^1$

A_1^i and B_1^i are $3(N_e^1 + N_i) \times 3N_i$

K_e^1 and Uk_e^1 are $3N_e^1 \times 1$

t_i^1 and u_i^1 are $3N_i^1 \times 1$

$\mathbf{B_e}^1$ and $\mathbf{K_e}^1$ can be multiplied together to form a known column vector $\mathbf{f}^1$

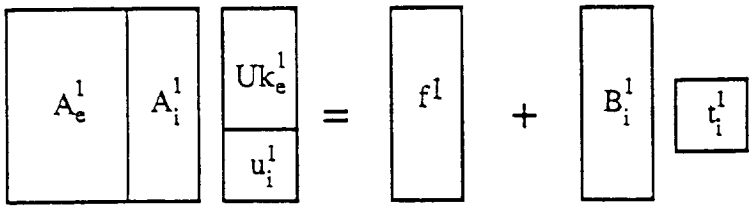

(2.59)

Moving the second term of the right hand side of Eq.2.58 to the left hand side leads to

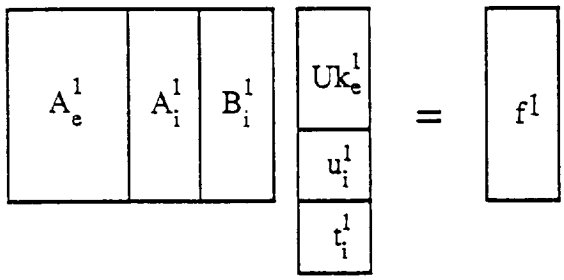

(2.60)

Note that the left hand side of Eq.2.60 now become a matrix with dimension of $3(N_e^1 + N_i)$ by $3(N_e^1 + 2N_i)$ multiplied by an unknown vector with dimension of $3(N_e^1 + N_i)$ by 1. Obviously, this system can not be solved since there are $3N_i$ more unknown than the total number of equations. Before we proceed to the second subregion, Eq.2.60 is reduced to

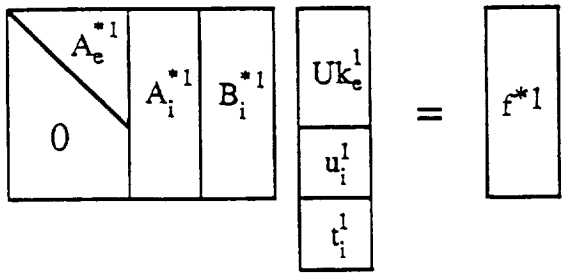

(2.61)

Eq.2.61 can be represented more conveniently as

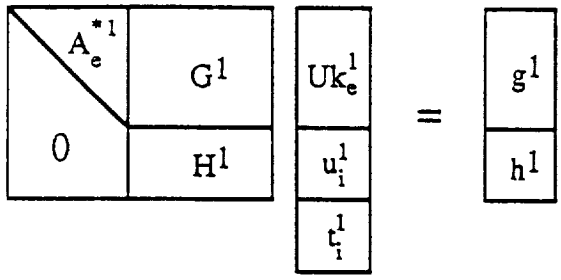

(2.62)

Eq.2.62 can be treated as two set of equations ,viz.

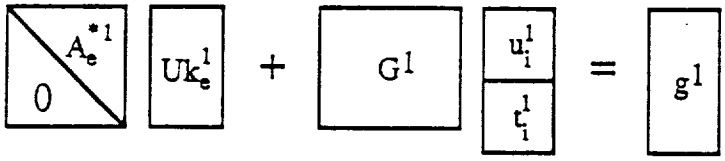

(2.63)

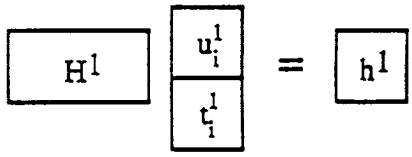

(2.64)

The same procedure can be applied to the second subregion and a similar set of

equations is obtained

$$\begin{bmatrix} A_e^{*2} \\ 0 \end{bmatrix} \begin{bmatrix} Uk_e^2 \end{bmatrix} + \begin{bmatrix} G^2 \end{bmatrix} \begin{bmatrix} u_i^2 \\ t_i^2 \end{bmatrix} = \begin{bmatrix} g^2 \end{bmatrix} \tag{2.65}$$

$$\begin{bmatrix} H^2 \end{bmatrix} \begin{bmatrix} u_i^2 \\ t_i^2 \end{bmatrix} = \begin{bmatrix} h^2 \end{bmatrix} \tag{2.66}$$

Note that the unknowns in Eq.2.64 and Eq.2.66 now only involve the unknown displacements and unknown tractions on the interface between the two subregions. By applying the compatibility and equilibrium condition of Eq.2.53,

$$t_i^1 = -t_i^2 = t_i$$
$$u_i^1 = u_i^2 = u_i$$

these two sets of equations can be assembled together as Eq.2.67 to solve for the unknown tractions and unknown displacements along the interface.

$$\begin{bmatrix} H^1 \\ \overline{H}^2 \end{bmatrix} \begin{bmatrix} u_i \\ t_i \end{bmatrix} = \begin{bmatrix} h^1 \\ h^2 \end{bmatrix} \tag{2.67}$$

where

$$\overline{H}^2 = - H^2$$

After the displacement $\mathbf{u}_i$ and the traction $\mathbf{t}_i$ of the interface have been solved using Eq.2.64, the unknowns on the external surfaces of each subregion can be solved through Eq.2.63 and Eq.2.65.

This method not only saves computer excution time by eliminating the need for solving for the inverse of the matrices but also saves a lot of memory storage space because the procedure can be performed on the system of equations of each subregion separately with little effort by using an index control in the computer program. It is therefore used in this paper.

2.5 Discontinuity of Traction

The data of prescribed tractions and prescribed displacements must be read into the computer according to the element rather than the node due to the possibility of a node lying on a position without an unique tangent plane. That is, when a node is at the intersection of two or more planes, the traction acting on this node depends on which plane is considered, since each surface is associated with a different normal. For example, in Fig.2.6, three elements share the same node P. For the sake of easy interpretation, we let the unit normal of these three elements coincide with the unit vectors of the Cartesian coordinate system.

$$\tilde{n}_1 = \hat{i}$$
$$\tilde{n}_2 = \hat{j}$$
$$\tilde{n}_3 = \hat{k}$$

The component of the traction of node P in direction i on element 1 is the normal stress σ_{11} but the traction of point P in the same direction on element 2 is the shear stress σ_{12} and the traction in the i-direction on element 3 is the shear stress σ_{13} at point P. Therefore, the prescribed traction must be input according to the element so that each different traction on the same node can be multiplied by an appropriate kernel contributed from each element surface. Also note that when the displacement in one direction is prescribed at a certain node, for a unique solution only one of

the corresponding tractions on this node can be unknown and all the others must be prescribed. For the same example in Fig.2.6, two of three tractions on three different elements must be known if the displacement of that node is prescribed. Eq.2.37 in fact is a concise expression for convenient intrepretation. To be more specific, it should read

$$\begin{bmatrix} \cdots & T^P & \cdots \end{bmatrix} \begin{bmatrix} \vdots \\ u^P \\ \vdots \end{bmatrix} = \begin{bmatrix} \cdots & U_1^P, & \cdots & U_2^P, & \cdots & U_3^P, & \cdots \end{bmatrix} \begin{bmatrix} \vdots \\ t_1^P \\ \vdots \\ t_2^P \\ t_3^P \\ \vdots \end{bmatrix} \qquad (2.68)$$

Thus, the equation for a certain row is

$$\cdots + T^P u^P + \cdots = \cdots + U_1^P t_1^P + U_2^P t_2^P + U_3^P t_3^P + \cdots \qquad (2.69)$$

When the tractions t_1P, t_2P and t_3P are known at point P, they must be multiplied by these different kernel function U_1^P, U_2^P, and U_3^P which are calculated from each different element with different normal vector. As for the case of the displacement being prescribed, only one traction can be unknown, say t_2^P, and the traction on another surface t_1^P and t_3^P must be forced to be known. Thus, the

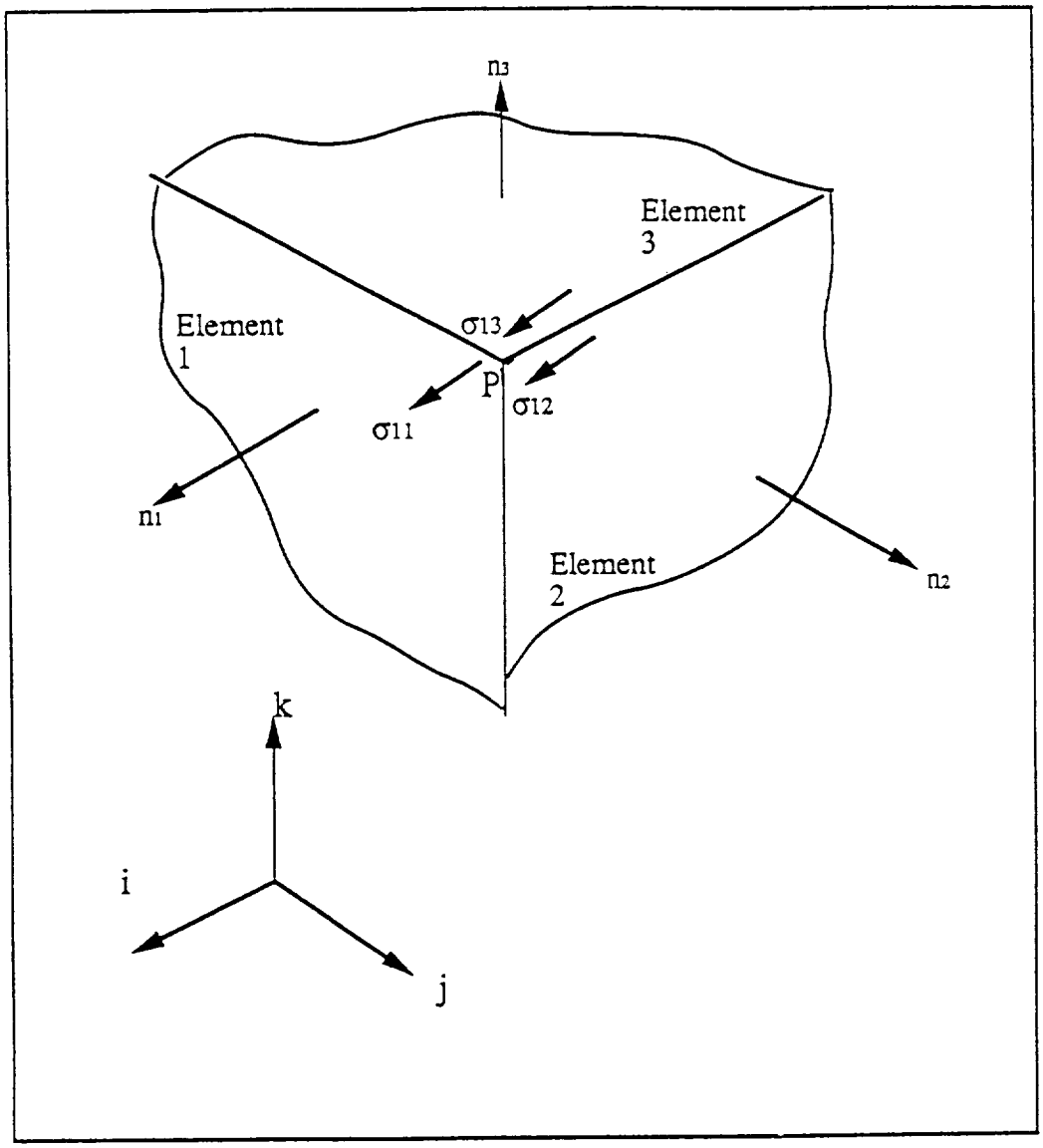

Figure 2.6 Illustration of Different Tractions at Node P

equation becomes

$$....+\ T^P u^P - U_1^P t_1^P - U_3{}^P t_3{}^P +..... = ...+\ U_2^P t_2^P + ... \qquad (2.70)$$

so that only one unknown is left on the right hand side of the equation which is needed to be solved and all the known values are summed up on the left hand side of the equation.

One incident merit of inputting the traction element by element is that discontinuous tractions can be modeled exactly.

CHAPTER THREE

LINEAR ELASTIC FRACTURE MECHANICS

3.1 Introduction

The presence of cracks in a material causes a stress concentration in the vicinity of the crack tip. Consequently, plastic yielding or microcracking will occur in the region surrounding the crack tip. Linear elastic fracture mechanics assumes that the nonlinear deformations are restricted to a region whose dimensions are small compared to other characteristic dimensions, so that the elastic solution provides an accurate description of the stress and displacement fields in the vicinity of the crack tip. This is often referred to as small scale yielding (S.S.Y.).

It can be shown that the loading on a crack is in general a superposition of three independent modes as shown in Figure 3.1. The first (Fig.3.1.a) is called the crack opening mode, or mode-I, which is a result of a relative normal separation of the crack surfaces (symmetric with respect to x-z and x-y planes). Fig.3.1.b is called the crack sliding mode, or mode-II, which is associated with a relative sliding displacement in the x-direction (symmetric with respect to x-y plane and skew-symmetric with respect to the x-z plane). The tearing mode (mode-III) corresponds to relative motion in the z-direction of the two crack surfaces (skew-symmetric with respect to the x-y and x-z planes). Using Westergard's technique, Irwin and Williams showed that the stress and displacement fields in the vicinity of a crack tip can be expressed as an infinite series whose leading term is square root singular. The coefficient of this singular term is defined as the stress intensity factor. With respect to a r-θ polar coordinate system as shown in Figure 3.2 , the stresses and

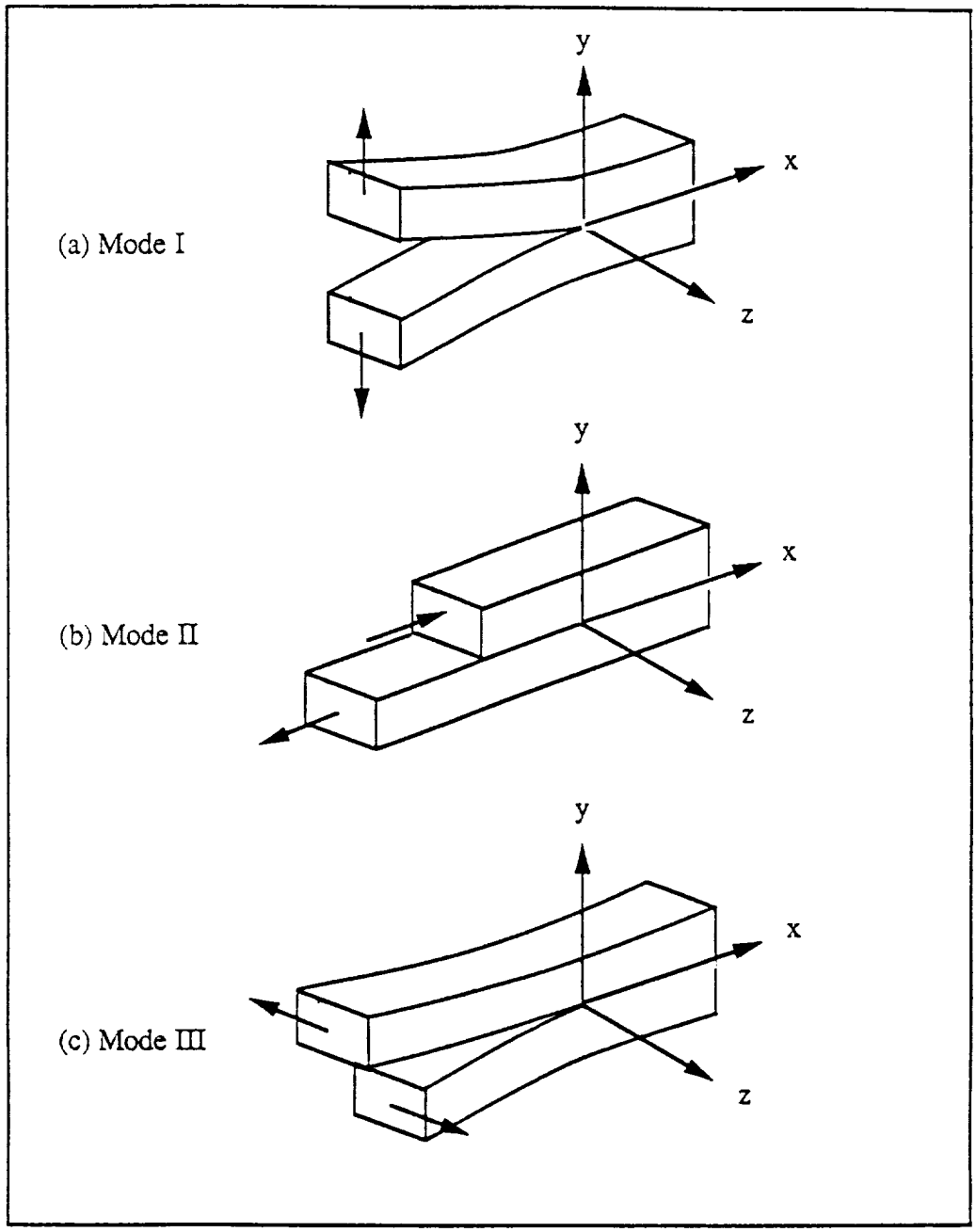

Figure 3.1 The Three Basic Modes of Crack Surface Displacement

displacements near a crack tip are given by [27]

Mode I

$$\sigma_{xx}= \frac{K_I}{\sqrt{2\pi r}} \cos\frac{\theta}{2} [\, 1- \sin\frac{\theta}{2} \sin\frac{3\theta}{2} \,]$$

$$\sigma_{yy}= \frac{K_I}{\sqrt{2\pi r}} \cos\frac{\theta}{2} [\, 1+ \sin\frac{\theta}{2} \sin\frac{3\theta}{2} \,]$$

$$\sigma_{xy}= \frac{K_I}{\sqrt{2\pi r}} \sin\frac{\theta}{2} \cos\frac{\theta}{2} \cos\frac{3\theta}{2}$$

$$\sigma_{zz}= \nu\, (\sigma_{xx}+ \sigma_{yy}), \qquad \sigma_{xz}= \sigma_{yz}= 0$$

$$u_1 = \frac{K_I}{\mu} \sqrt{\frac{r}{2\pi}} \cos\frac{\theta}{2} [\, 1 - 2\nu + \sin^2\frac{\theta}{2} \,]$$

$$u_2 = \frac{K_I}{\mu} \sqrt{\frac{r}{2\pi}} \sin\frac{\theta}{2} [\, 2 - 2\nu - \cos^2\frac{\theta}{2} \,]$$

$$u_3 = 0 \qquad (3.1)$$

Mode II

$$\sigma_{xx}= \frac{K_{II}}{\sqrt{2\pi r}} \sin\frac{\theta}{2} [\, 2 + \cos\frac{\theta}{2} \cos\frac{3\theta}{2} \,]$$

$$\sigma_{yy}= \frac{K_{II}}{\sqrt{2\pi r}} \sin\frac{\theta}{2} \cos\frac{\theta}{2} \cos\frac{3\theta}{2}$$

$$\sigma_{xy}= \frac{K_{II}}{\sqrt{2\pi r}} \cos\frac{\theta}{2} [\, 1 - \sin\frac{\theta}{2} \sin\frac{3\theta}{2} \,]$$

$$\sigma_{zz}= \nu\, (\sigma_{xx}+ \sigma_{yy}), \quad \sigma_{xz}= \sigma_{yz}= 0$$

$$u_1 = \frac{K_{II}}{\mu}\sqrt{\frac{r}{2\pi}}\sin\frac{\theta}{2}\left[2 - 2\nu + \cos^2\frac{\theta}{2}\right]$$

$$u_2 = \frac{K_{II}}{\mu}\sqrt{\frac{r}{2\pi}}\cos\frac{\theta}{2}\left[-1 + 2\nu + \sin^2\frac{\theta}{2}\right]$$

$$u_3 = 0 \qquad (3.2)$$

Mode III

$$\sigma_{xz} = -\frac{K_{III}}{\sqrt{2\pi r}}\sin\frac{\theta}{2}$$

$$\sigma_{yz} = \frac{K_{III}}{\sqrt{2\pi r}}\cos\frac{\theta}{2}$$

$$\sigma_{xx} = \sigma_{yy} = \sigma_{zz} = \sigma_{xy} = 0$$

$$u_1 = u_2 = 0$$

$$u_3 = \frac{K_{III}}{\mu}\sqrt{\frac{r}{2\pi}}\sin\frac{\theta}{2} \qquad (3.3)$$

where K_I, K_{II}, and K_{III} are the stress intensity factors corresponding to modes I, II, and III, respectively. Note that Eq.3.1-3.3 are valid only when $r << L$, where L is another characterictic length of the geometry (may be the crack length). Also note that these equations do not contain any information about the externally applied loading, crack geometry, geometric configuration, etc, and that the stress intensity factors are not functions of the local coordinate r and θ. These factors are embedded

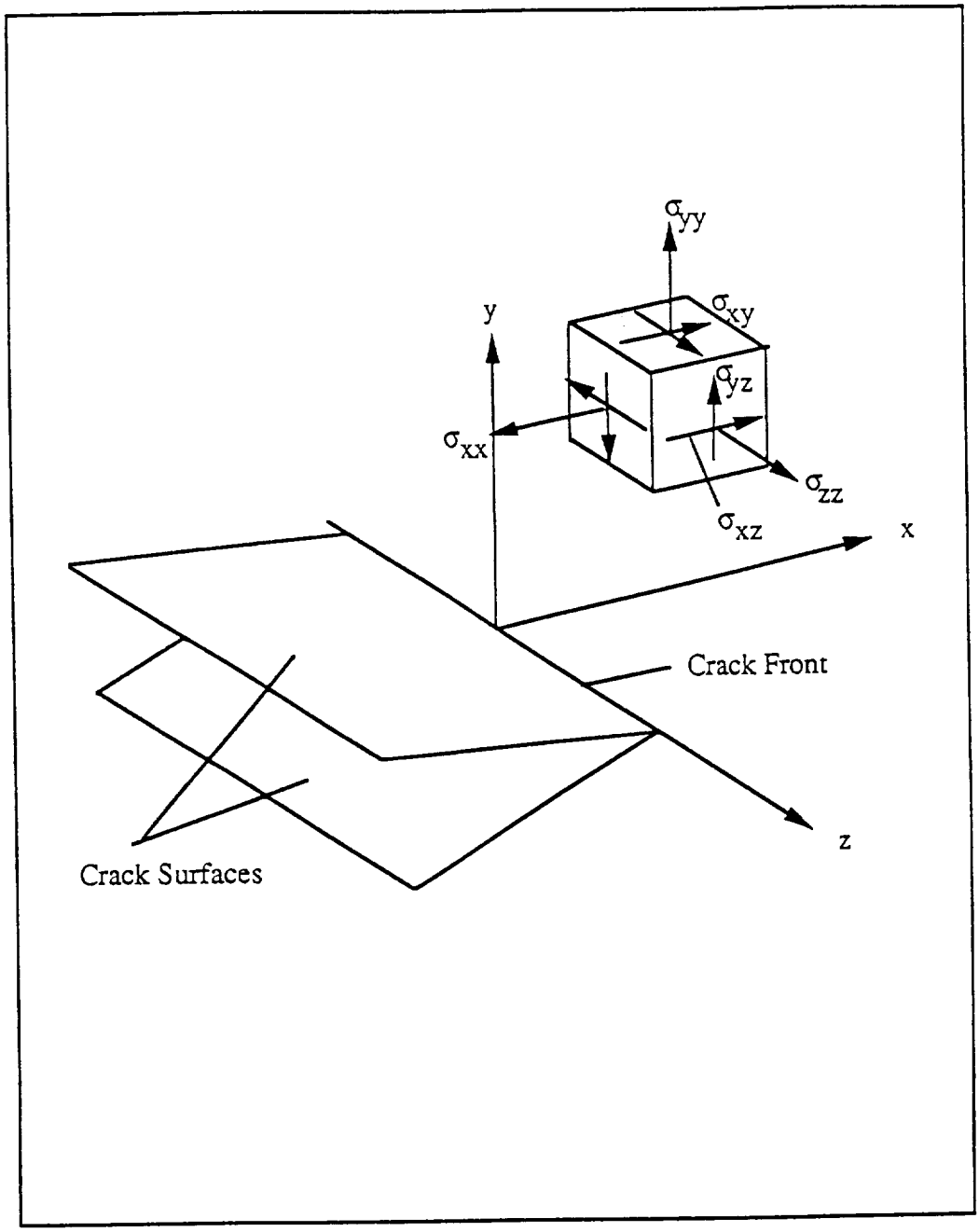

Figure 3.2 Coordinate and Stress Components for Crack Tip Stress Field

in K_I, K_{II}, and K_{III}. That is, the stress intensity factors K_I, K_{II}, and K_{III}, which must be determined by the boundary conditions and the loadings control the magnitudes of the stress and displacement fields around the crack tip. Thus, a given combination of values of K_I, K_{II}, and K_{III} represents uniquely a crack tip stress field environment for small scale yielding. The determination of the stress intensity factors is thus the most important task in linear elastic fracture mechanics. Although Eq.3.1-3.3 are valid for the plane strain problem, they may be modified to represent the plane stress problem by letting $\sigma_z = 0$ and substituting ν with $\nu/(1+\nu)$.

Eq.3.1 and Eq.3.2 were derived for plane problems. However, it was shown by Sih and Liebowitz [28] that for an elliptical crack in a three dimensional linear elastic body, the local stress and displacement fields along a crack front are a superposition of plane strain and antiplane shear. Hence, Eq.3.1-3.3 can still be used for three dimensional crack problems as long as the coordinate system is allowed to move along the crack front with its z-axis tangent to the crack front and the y-coordinate perpendicular to the crack surface, as shown in Fig.3.3. Referring to the moving coordinate, the stress intensity factors are now also a function of the position of the origin on the crack front and the formulas are not available for a crack near a free surface because the stress singularity is not of inverse square root there.

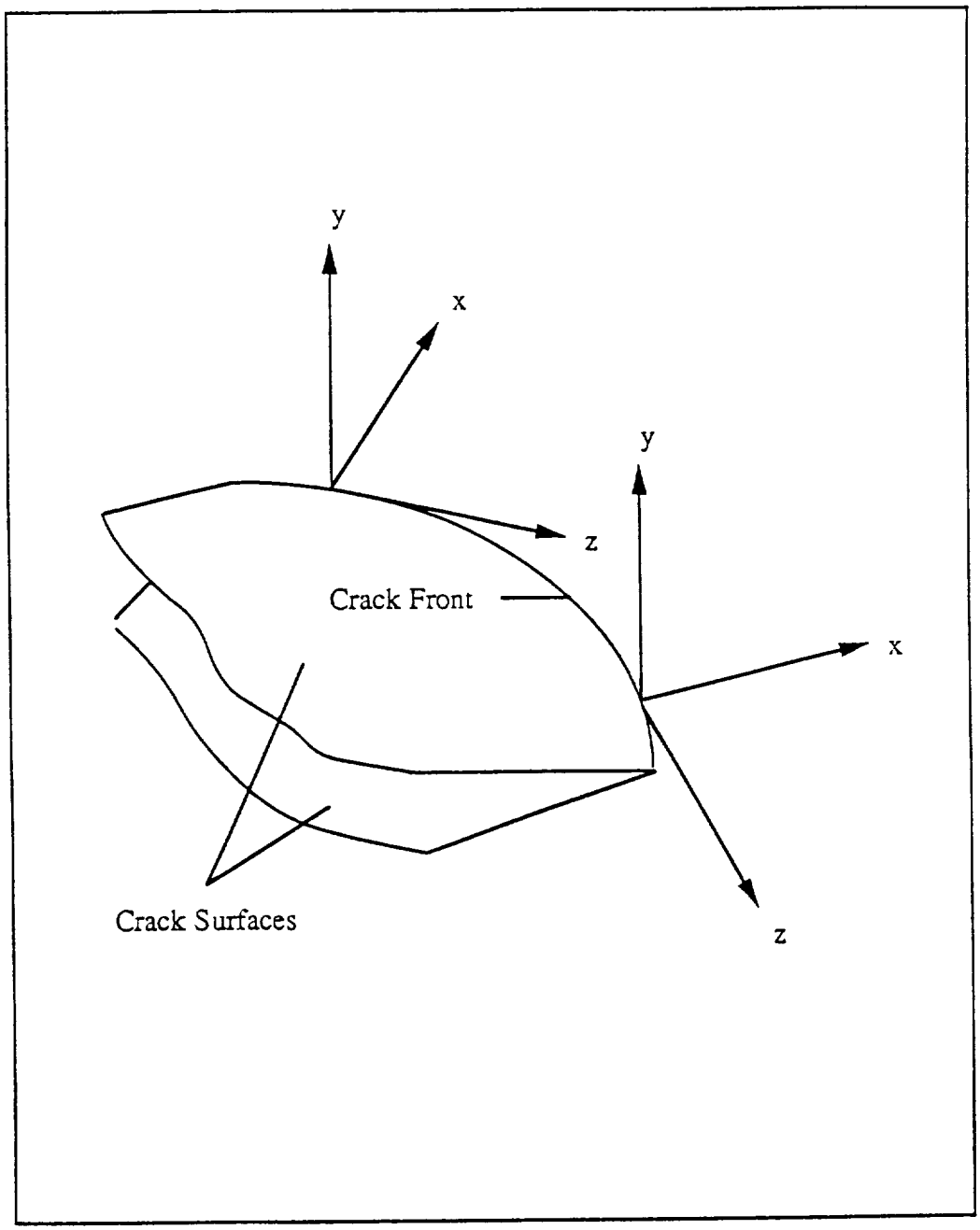

Figure 3.3 Coordinate System on the Crack Front for Three Dimensional Crack

3.2 Calculation of Stress Intensity Factors Using the Boundary Element Method

The variation of any function in an isoparametric element is polynominal. The degree of the polynominal depends on the number and arrangement of the nodes. Therefore, if a quadratic surface element is used in the vicinity of a crack, the distributions of the displacement and traction in the element will have at most quadratic variations. Since the variation of the displacement is square root of r and the variation of the tracton is inverse of square root of r around the crack, a fine mesh is needed to model the crack so that the quadratic variation can imitate the correct distribution inside each small segment. However, even this refinement cannot achieve a high degree of accuracy.

Fortunately, this problem was solved by Barsoum [18] who modified the quadratic isoparametric element by relocating appropriate midside nodes to the quarter-point to capture the inverse square root singularity. Even though he had done this for the Finite Element Method, a similar approach can be used in the Boundary Element Method. For example, consider an eight node quadrilateral element with two sides having equal length L perpendicular to the crack front (side 1-5-2),as shown in Fig.3.4. Relocate the two midside node (6 and 8) to the quarter-point near the crack front. Denoting the distance originated from the crack front to any point on the element by r, then

$$r = \sum_{i=1}^{8} N_i(\xi_1,\xi_2) r_i \qquad (3.4)$$

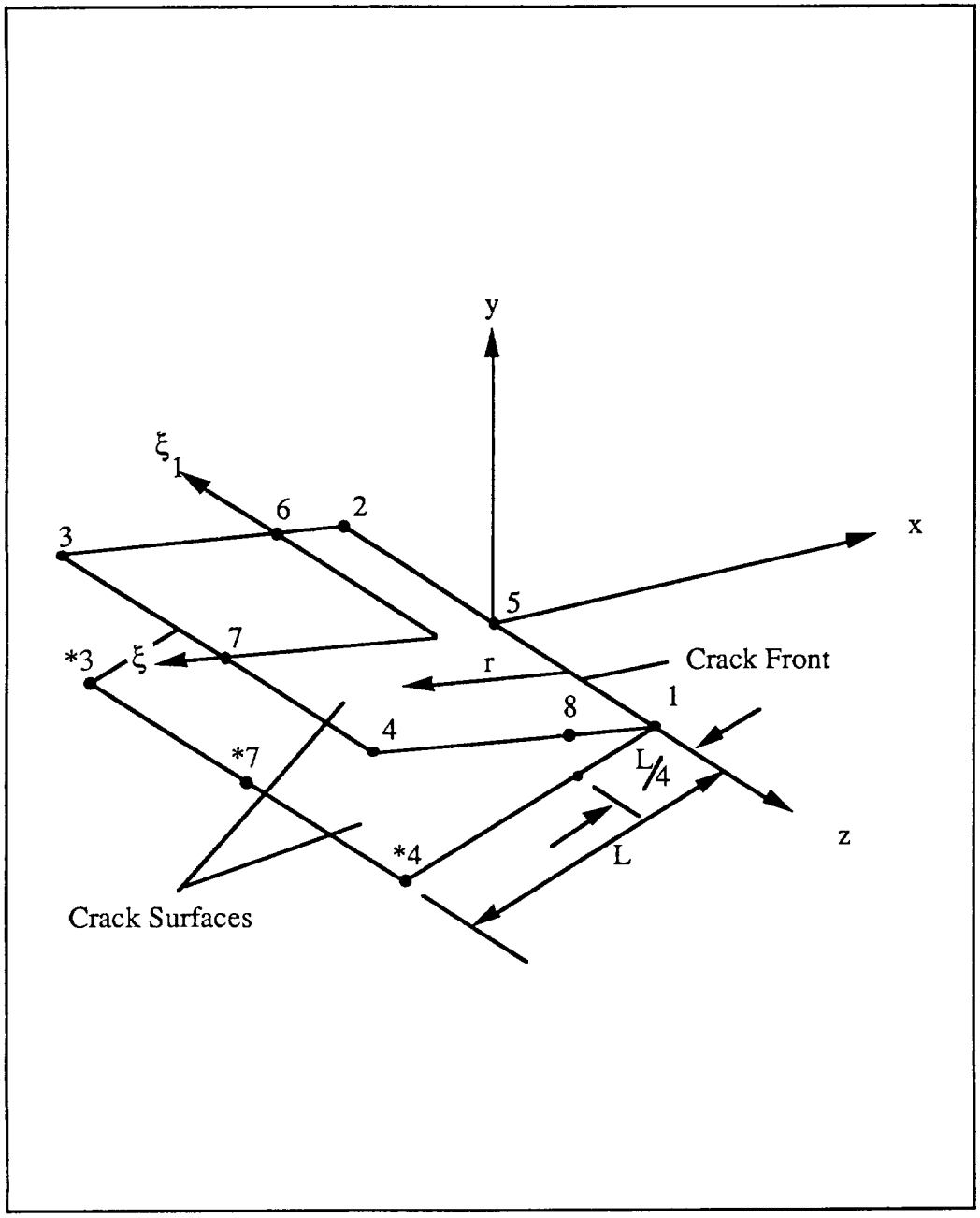

Figure 3.4 Illustration of 8-node Quarter Point Element

Choosing $r_1 = r_2 = r_5 = 0$, $r_3 = r_4 = r_7 = L$, and $r_6 = r_8 = L/4$, Eq.3.4 becomes

$$r = \frac{1}{4}(\xi_1+\xi_2- 1)(1+ \xi_1)(1+ \xi_2)\, L + \frac{1}{4}(\xi_1- \xi_2+ 1)(\xi_1- 1)(\xi_2 +1)\, L$$
$$+\frac{1}{2}(1+ \xi_1)(1 - \xi_2^2)\times\frac{L}{4} + \frac{1}{2}(1+ \xi_2)(1 - \xi_1^2)L + \frac{1}{2}(1 - \xi_1)(1 - \xi_2^2)\times\frac{L}{4}$$

Simplifying,

$$\xi_2 = 2\sqrt{\frac{r}{L}} - 1 \qquad (3.5)$$

Substitution of Eq.3.5 into Eq.2.33, leads to the following variation of the displacement and traction in direction i versus the distance r

$$
\begin{aligned}
u_i(r) &= \sum_{k=1}^{8} N^k u_i^k \\
&= [(-u_i^1 - u_i^2 - u_i^3 - u_i^4 - u_i^5 + 2u_i^6 + u_i^7 + 2u_i^8) \\
&\quad + \frac{\xi_1}{2}(3u_i^1 - 3u_i^2 - u_i^3 + u_i^4 + 4u_i^6 - 4u_i^8) \\
&\quad + \frac{\xi_1^2}{2}(-u_i^1 - u_i^2 + u_i^3 + u_i^4 + 2u_i^5 - 2u_i^7)] \sqrt{\frac{r}{L}} \\
&+ [(u_i^1 + u_i^2 + u_i^3 + u_i^4 - 2u_i^6 - 2u_i^8) \\
&+ [u_i^5 + \frac{\xi_1}{2}(-u_i^1 + u_i^2) + \frac{\xi_1^2}{2}(u_i^1 + u_i^2 - 2u_i^5)]
\end{aligned}
\tag{3.6}
$$

which can be rewritten as,

$$
u_i(r) = A_i^1 + A_i^2 \sqrt{\frac{r}{L}} + A_i^3 \frac{r}{L} \tag{3.7}
$$

Similary,

$$
t_i(r) = B_i^1 + B_i^2 \sqrt{\frac{r}{L}} + B_i^3 \frac{r}{L} \tag{3.8}
$$

The displacement variation given in Eq.3.7 contains the square root of r term which is asymptotically correct. However, the traction appearing in Eq.3.8 does not include the correct inverse square root of r term needed to model the stress singularity around the crack tip. The correct singularity is obtained by multiplying the right hand side of Eq.3.8 by the factor [19]

$$\phi(r) = \sqrt{\frac{L}{r}} = \frac{2}{\xi_2 + 1} \tag{3.9}$$

such that the variation of traction becomes

$$\begin{aligned} t_i(r) &= \left(B_i^1 + B_i^2 \sqrt{\frac{r}{L}} + B_i^3 \frac{r}{L} \right) \sqrt{\frac{L}{r}} \\ &= B_i^1 \sqrt{\frac{L}{r}} + B_i^2 + B_i^3 \sqrt{\frac{r}{L}} \end{aligned} \tag{3.10}$$

which possesses the correct inverse square root of r term.

For six node triangular quadratic elements, if all the sides are straight as shown in Fig.3.5, by similar procedure, the relation between r and the nature coordinate ξ can be obtained as

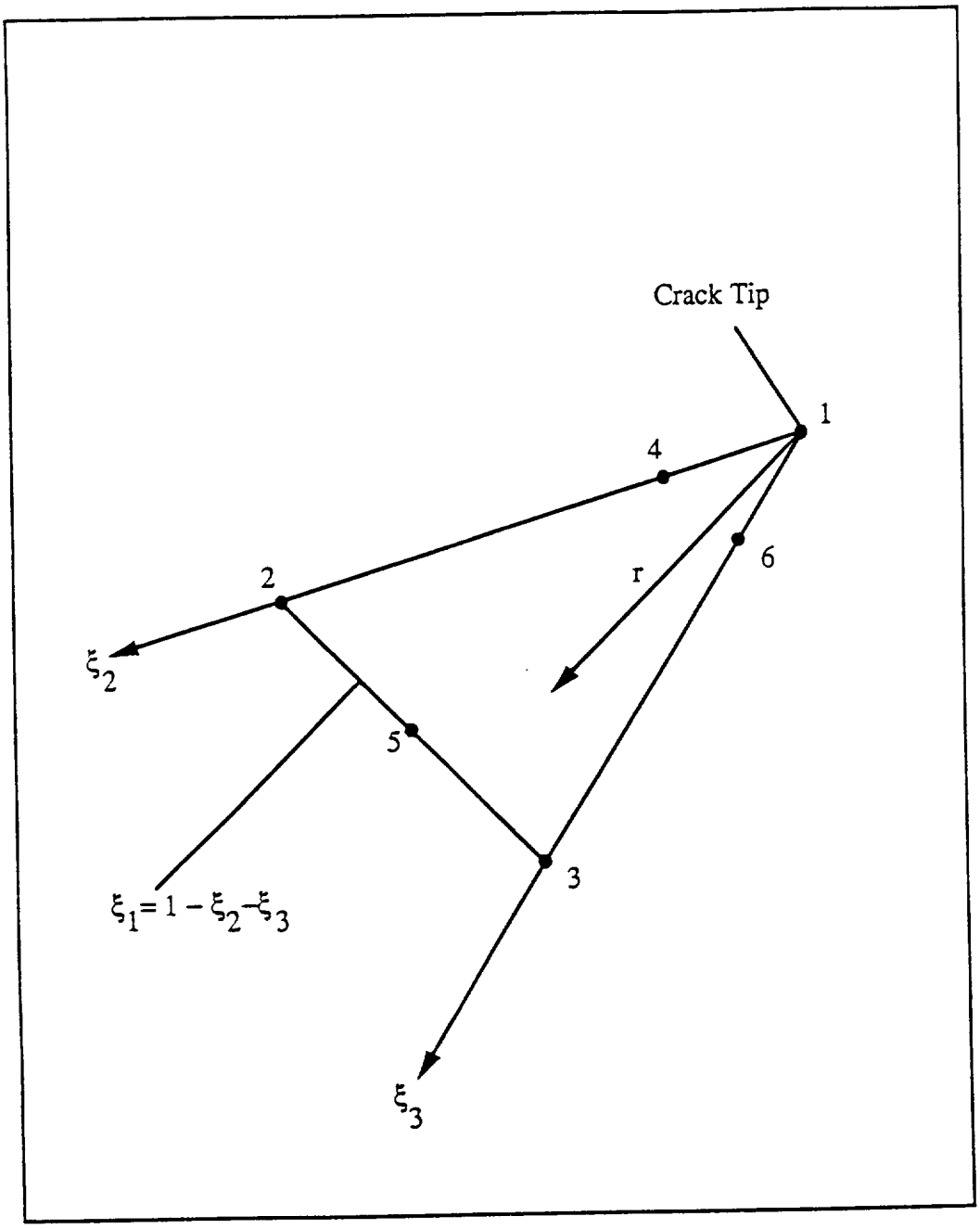

Figure 3.5 Illustration of 6-node Quarter Point Element

$$\xi_1 = 1 - \sqrt{\frac{r}{c}} \tag{3.11}$$

where c is the ratio ξ_2 / ξ_3 which is constant for a given direction r. It is easy to show that the variation of the displacement has the same form as Eq.3.7 by substituting Eq.3.11 into Eq.2.30 with the help of appropriate shape function. The correct traction variation is obtained by multiplying the shape function for traction by the correction factor

$$\phi(r) = \sqrt{\frac{c}{r}} = \frac{1}{1 - \xi_1} \tag{3.12}$$

The stress intensity factors are then evaluated by the displacement correlation technique [29]. By setting $\theta = 180°$ in Eq.3.1-3.3, the displacement fields become

$$u_1 = \frac{2(1-\nu^2)}{E}\sqrt{\frac{2r}{\pi}}\, K_I$$
$$u_2 = \frac{2(1-\nu^2)}{E}\sqrt{\frac{2r}{\pi}}\, K_{II}$$
$$u_3 = \frac{2(1+\nu)}{E}\sqrt{\frac{2r}{\pi}}\, K_{III} \tag{3.13}$$

Equating the square root of r term in Eq.3.13 to that in Eq.3.6 yields

$$K_I = \frac{E}{2(1-\nu^2)}\sqrt{\frac{\pi}{2L}}\ [(-u_1^{\,1} - u_1^{\,2} - u_1^{\,3} - u_1^{\,4} - u_1^{\,5} + 2u_1^{\,6} + u_1^{\,7} + 2u_1^{\,8}) + \frac{\xi_1}{2}(3u_1^{\,1} - 3u_1^{\,2} - u_1^{\,3} + u_1^{\,4} + 4u_1^{\,6} - 4u_1^{\,8}) + \frac{\xi_1^{\,2}}{2}(-u_1^{\,1} - u_1^{\,2} + u_1^{\,3} + u_1^{\,4} + 2u_1^{\,5} - 2u_1^{\,7})]$$

$$K_{II} = \frac{E}{2(1-\nu^2)}\sqrt{\frac{\pi}{2L}}\ [(-u_2^{\,1} - u_2^{\,2} - u_2^{\,3} - u_2^{\,4} - u_2^{\,5} + 2u_2^{\,6} + u_2^{\,7} + 2u_2^{\,8}) + \frac{\xi_1}{2}(3u_2^{\,1} - 3u_2^{\,2} - u_2^{\,3} + u_2^{\,4} + 4u_2^{\,6} - 4u_2^{\,8}) + \frac{\xi_1^{\,2}}{2}(-u_2^{\,1} - u_2^{\,2} + u_2^{\,3} + u_2^{\,4} + 2u_2^{\,5} - 2u_2^{\,7})]$$

$$K_{III} = \frac{E}{2(1+\nu)}\sqrt{\frac{\pi}{2L}}\ [(-u_3^{\,1} - u_3^{\,2} - u_3^{\,3} - u_3^{\,4} - u_3^{\,5} + 2u_3^{\,6} + u_3^{\,7} + 2u_3^{\,8}) + \frac{\xi_1}{2}(3u_3^{\,1} - 3u_3^{\,2} - u_3^{\,3} + u_3^{\,4} + 4u_3^{\,6} - 4u_3^{\,8}) + \frac{\xi_1^{\,2}}{2}(-u_3^{\,1} - u_3^{\,2} + u_3^{\,3} + u_3^{\,4} + 2u_3^{\,5} - 2u_3^{\,7})]$$

(3.14)

For non-symmetric problems both crack surfaces must be modeled. The stress intensity factors are given by

$$K_I = \frac{E}{4(1-\nu^2)}\sqrt{\frac{\pi}{2L}}\{[(-u_1^3 - u_1^4 + 2u_1^6 + u_1^7 + 2u_1^8) - (-u_1^{*3} - u_1^{*4} + 2u_1^{*6} + u_1^{*7} + 2u_1^{*8})]$$
$$+ \frac{\xi_1}{2}[(-u_1^3 + u_1^4 + 4u_1^6 - 4u_1^8) - (-u_1^{*3} + u_1^{*4} + 4u_1^{*6} - 4u_1^{*8})]$$
$$+ \frac{\xi_1^2}{2}[(u_1^3 + u_1^4 - 2u_1^7) - (u_1^{*3} + u_1^{*4} - 2u_1^{*7})]\}$$

$$K_{II} = \frac{E}{4(1-\nu^2)}\sqrt{\frac{\pi}{2L}}\{[(-u_2^3 - u_2^4 + 2u_2^6 + u_2^7 + 2u_2^8) - (-u_2^{*3} - u_2^{*4} + 2u_2^{*6} + u_2^{*7} + 2u_2^{*8})]$$
$$+ \frac{\xi_1}{2}[(-u_2^3 + u_2^4 + 4u_2^6 - 4u_2^8) - (-u_2^{*3} + u_2^{*4} + 4u_2^{*6} - 4u_2^{*8})]$$
$$+ \frac{\xi_1^2}{2}[(u_2^3 + u_2^4 - 2u_2^7) - (u_2^{*3} + u_2^{*4} - 2u_2^{*7})]\}$$

$$K_{III} = \frac{E}{4(1+\nu)}\sqrt{\frac{\pi}{2L}}\{[(-u_3^3 - u_3^4 + 2u_3^6 + u_3^7 + 2u_3^8) - (-u_3^{*3} - u_3^{*4} + 2u_3^{*6} + u_3^{*7} + 2u_3^{*8})]$$
$$+ \frac{\xi_1}{2}[(-u_3^3 + u_3^4 + 4u_3^6 - 4u_3^8) - (-u_3^{*3} + u_3^{*4} + 4u_3^{*6} - 4u_3^{*8})]$$
$$+ \frac{\xi_1^2}{2}[(u_3^3 + u_3^4 - 2u_3^7) - (u_3^{*3} + u_3^{*4} - 2u_3^{*7})]\} \qquad (3.15)$$

where the asterisk refers to the displacement of the node on the element opposite to the one shown in Fig.3.5. Note that Eq.3.14 and Eq.3.15 involve the natural coordinate ξ_1 up to quadratic terms. Therefore a quadratic variation of the stress intensity factor in the ξ_1 direction can also be represented.

CHAPTER FOUR

VERIFICATION PROBLEMS

Several verification problems were studied to examine the accuracy and efficiency of the Boundary Element Method. This chapter presents the results obtained using the techniques described in the previous chapters for problems whose analytical solution is known as well as for a problem whose solution was obtained numerically by other researchers using different techniques. All problems were performed using single precision on a CRAY-X-MP. The material properities are: E = 30,000 ksi and ν = 0.3.

4.1 Prismatic Bar under Uniform Tension

The first verification problem is a linear elastic prismatic bar under simple tension as shown in Figure 4.1. Only one-eighth of the specimen is modeled due to the symmetry of this problem. The domain is chosen to be a cube with side length equal to 1 subjected to a uniform tension on the surface z=1. The planes x=0, y=0,and z=0 are fixed in x, y, and z directions, respectively. The geometry and boundary segments are given in Figures 4.2 to 4.5. Four different elements: 3-node triangular element, 4-node quadrilateral element, 6-node triangular element, and 8-node quadrilateral element were tested. Different schemes of Gaussian quadrature were chosen to perform both the regular integral and singular integral as described in Section 2.3. The traction in direction z at point A and the transverse displacement in the x-direction of point B in Figure 4.1 were calculated and compared with the exact solution [31]:

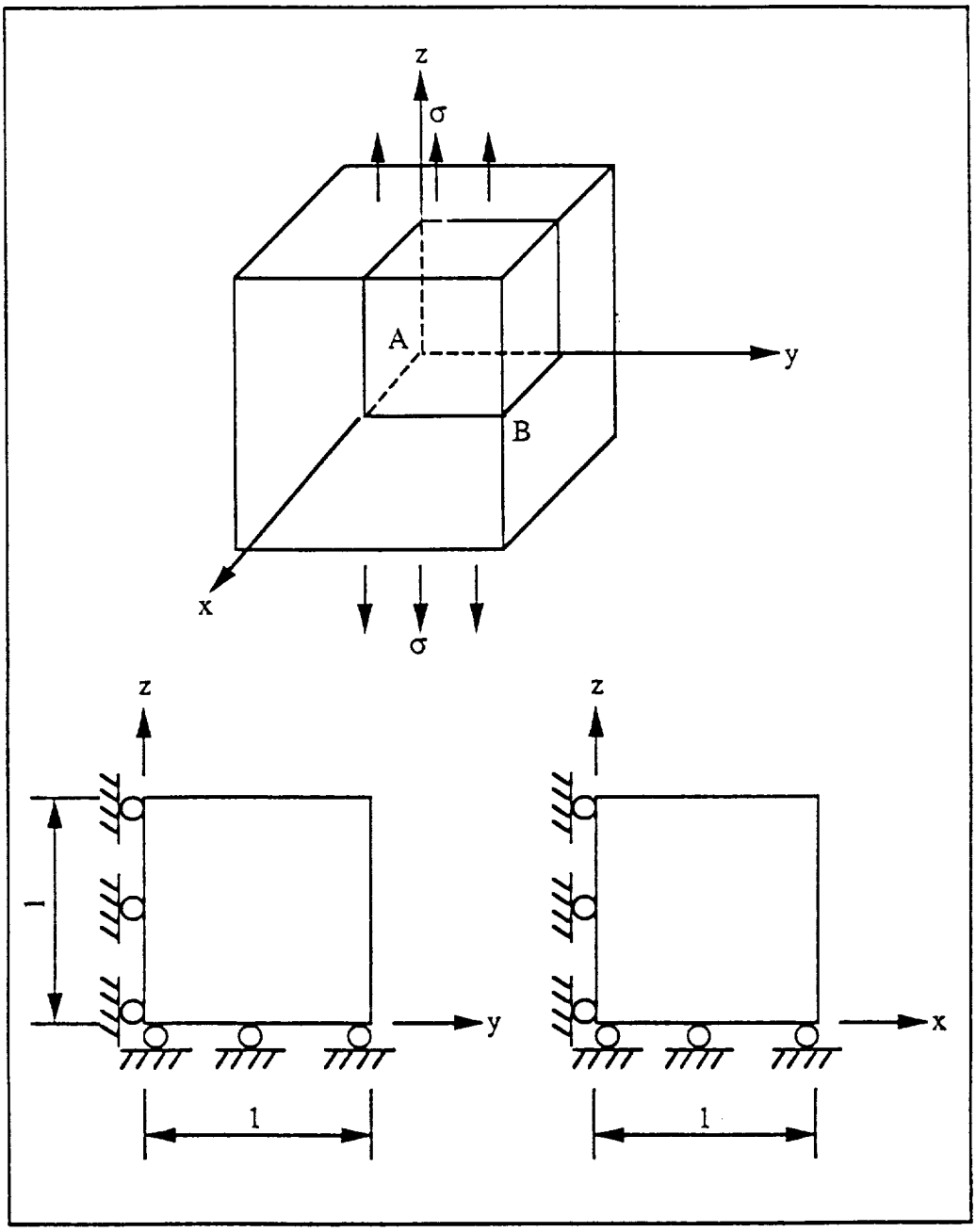

Figure 4.1 Geometry and Boundary Conditions for Prismatic Bar in Uniform Tension

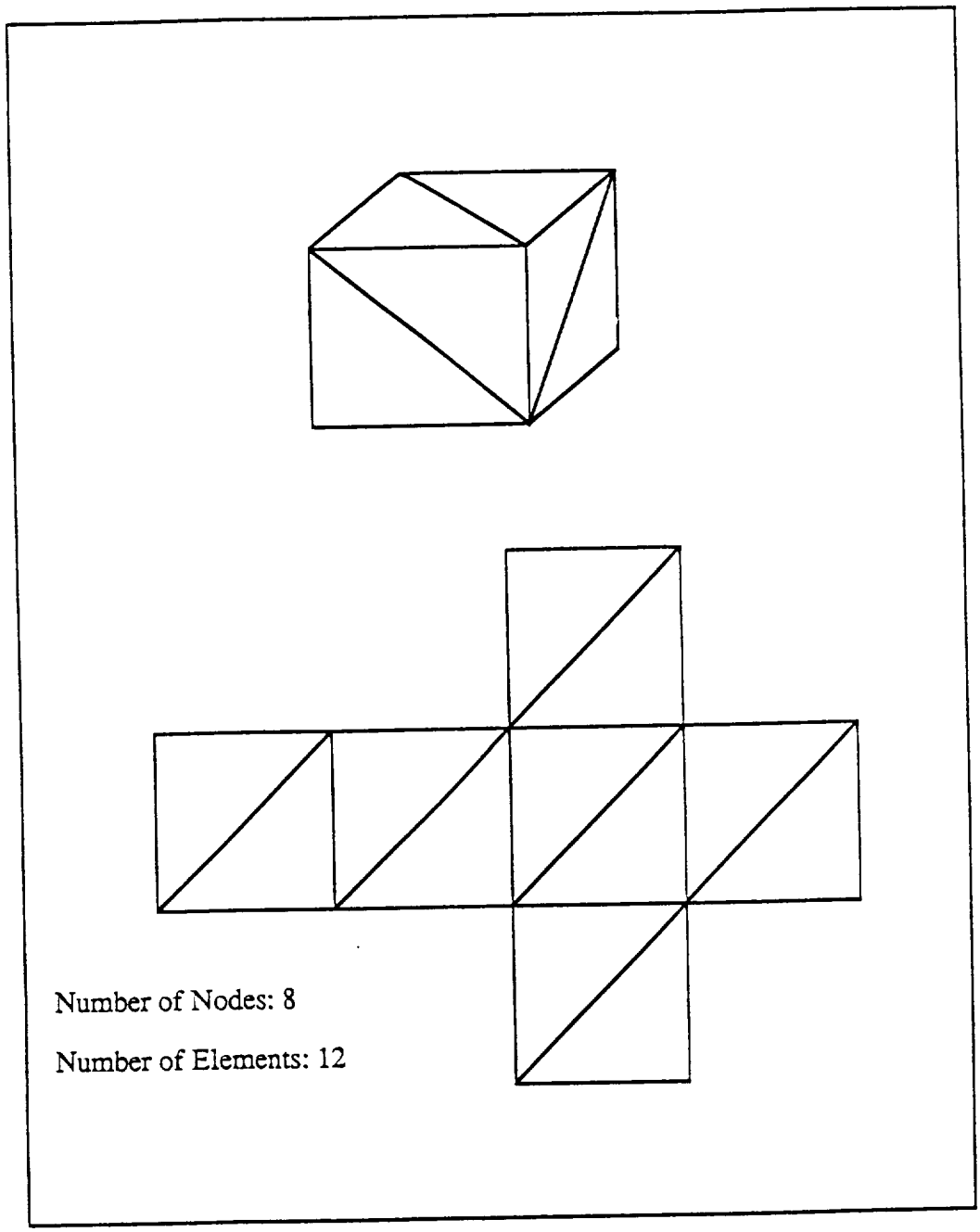

Figure 4.2 3-Node Triangular Element Mesh for Uniform Tension Problem

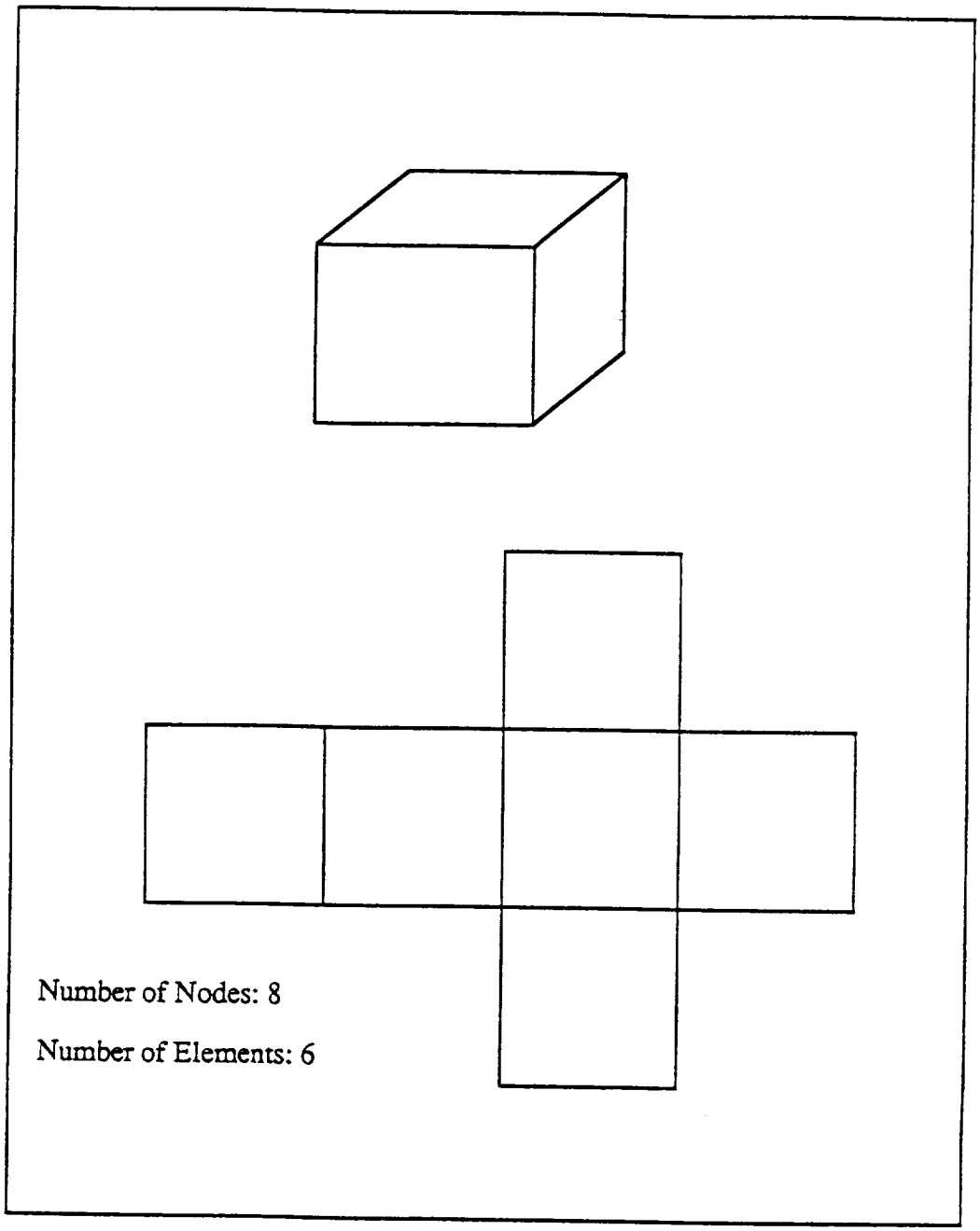

Figure 4.3 4-Node Quadrilateral Element Mesh for Uniform Tension Problem

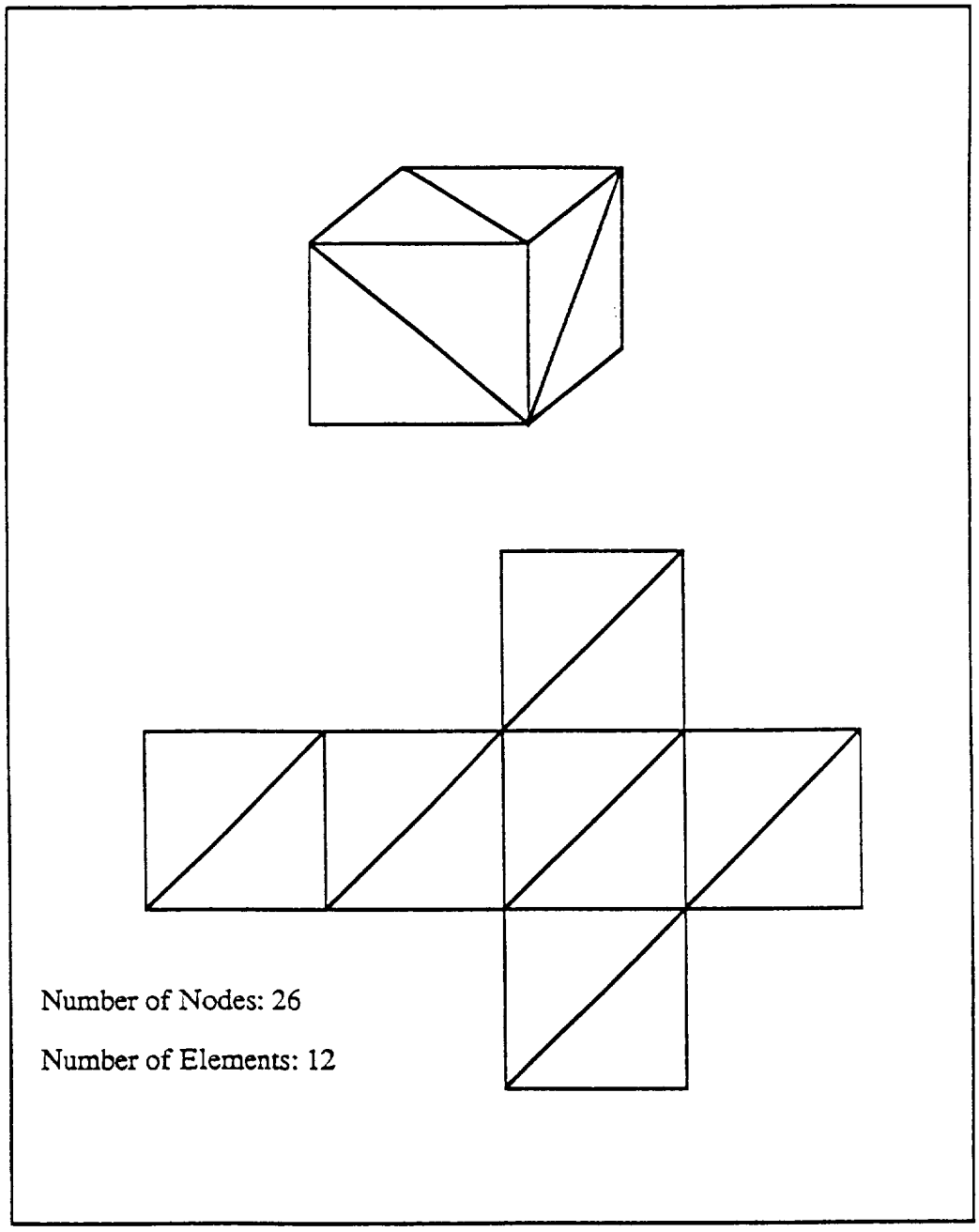

Figure 4.4 6-Node Triangular Element Mesh for Uniform Tension Problem

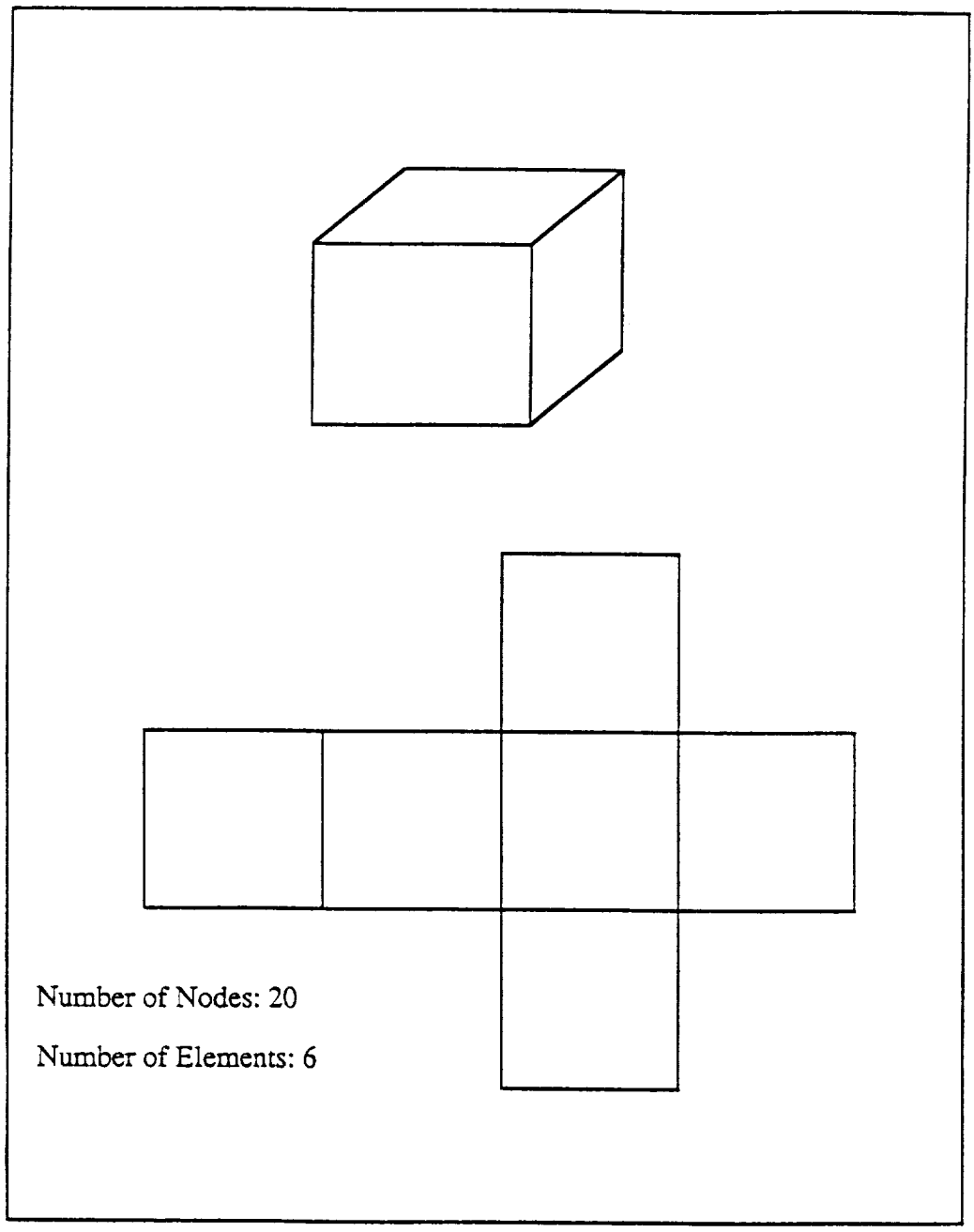

Figure 4.5 8-Node Quadrilaterial Element Mesh for Uniform Tension Problem

$$t_A = -\sigma$$

$$u_B = -\nu\,\sigma/E \qquad (4.1)$$

The results are summarized in Table 4.1 to 4.4. The results indicate that as long as the singular integral is evaluated with at least a 3x3 quadrature, then the accuracy depends on the number of points used to evaluate the regular integral. For reliable results the regular integral should be evaluated using at least a 3x3 quadrature for quadrilateral elements and 6 points quadrature for triangular elements.

Tables 4.5 to 4.8 demonstrate the accuracy of the multi-domain technique. The conclusions are similar to those for the single region. However, the two-region results are more accurate since for the same number of integration points there are more nodes.

NRI	NSI	u_A ($\times 10^{-6}$)	Error (%)	t_B	Error (%)	CPU Time (second)
1	1x1	------	>100	------	>100	0.0628
	2x2	1.4397	43.97	-0.4897	51.03	0.1156
	3x3	1.4214	42.14	-0.5409	45.91	0.2056
	4x4	1.4197	41.97	-0.5451	45.49	0.3362
	5x5	1.4197	41.97	-0.5454	45.46	0.4948
	6x6	1.4197	41.97	-0.5454	45.46	0.7030
3	1x1	0.7303	26.97	-0.4628	53.72	0.1110
	2x2	0.9376	6.24	-0.9861	1.39	0.1629
	3x3	0.9600	4.00	-1.0470	4.70	0.2430
	4x4	0.9582	4.18	-1.0611	6.11	0.3808
	5x5	0.9580	4.20	-1.0611	6.11	0.5437
	6x6	0.9580	4.20	-1.0611	6.11	0.7409
4	1x1	0.7244	27.56	-0.4808	51.92	0.1312
	2x2	0.9310	6.90	-1.0121	1.21	0.1852
	3x3	0.9548	4.52	-1.0800	8.00	0.2762
	4x4	0.9549	4.51	-1.0862	8.62	0.3998
	5x5	0.9547	4.53	-1.0867	8.67	0.5635
	6x6	0.9547	4.53	-1.0867	8.67	0.7684
6	1x1	0.7564	24.36	-0.4041	59.59	0.1954
	2x2	0.9746	2.54	-0.9250	7.50	0.2466
	3x3	1.0035	0.35	-0.9907	0.93	0.3379
	4x4	1.0017	0.17	-0.9967	0.33	0.4635
	5x5	1.0019	0.19	-0.9971	0.29	0.6254
	6x6	1.0019	0.19	-0.9971	0.29	0.8280
7	1x1	0.7559	24.41	-0.4031	59.69	0.2184
	2x2	0.9739	2.61	-0.9237	7.61	0.2692
	3x3	0.9984	0.16	-0.9897	1.03	0.3623
	4x4	0.9988	0.12	-0.9956	0.44	0.4865
	5x5	0.9989	0.11	-0.9960	0.40	0.6615
	6x6	0.9989	0.11	-0.9960	0.40	0.8518
12	1x1	0.7552	24.48	-0.4072	59.28	0.4131
	2x2	0.9728	2.72	-0.9280	7.20	0.4764
	3x3	0.9979	0.21	-0.9937	0.63	0.5624
	4x4	1.0002	0.02	-0.9997	0.03	0.6848
	5x5	1.0001	0.01	-1.0000	0.00	0.8425
	6x6	1.0001	0.01	-1.0000	0.00	1.0503

NRI : Number of Gaussian quadrature points for regular integral
NS I : Number of Gaussian quadrature points for singular integral
Exact solution : u=1.E-06, t=-1.00

Table 4.1 Beam in Uniform Tension, 3-node Triangular Element: Comparison of Error for Displacement and Traction, and CPU Time

NRI	NSI	u_A ($\times 10^{-6}$)	Error (%)	t_B	Error (%)	CPU Time (second)
1x1	1x1	------	>100	-----	>100	0.0565
	2x2	1.3438	34.38	-1.0000	0.00	0.1445
	3x3	1.3453	34.53	-1.0000	0.00	0.2951
	4x4	1.3453	34.53	-1.0000	0.00	0.4984
	5x5	1.3453	34.53	-1.0000	0.00	0.7735
	6x6	1.3453	34.53	-1.0000	0.00	1.0980
2x2	1x1	0.9264	7.36	-1.0000	0.00	0.0764
	2x2	0.9559	4.41	-1.0000	0.00	0.1659
	3x3	0.9568	4.32	-1.0000	0.00	0.3120
	4x4	0.9568	4.32	-1.0000	0.00	0.5217
	5x5	0.9568	4.32	-1.0000	0.00	0.7866
	6x6	0.9568	4.32	-1.0000	0.00	1.1149
3x3	1x1	0.9689	3.11	-1.0000	0.00	0.1118
	2x2	1.0008	0.08	-1.0000	0.00	0.2003
	3x3	1.0017	0.17	-1.0000	0.00	0.3492
	4x4	1.0017	0.17	-1.0000	0.00	0.5586
	5x5	1.0017	0.17	-1.0000	0.00	0.8286
	6x6	1.0017	0.17	-1.0000	0.00	1.1609
4x4	1x1	0.9673	3.27	-1.0000	0.00	0.1582
	2x2	0.9992	0.08	-1.0000	0.00	0.2502
	3x3	1.0000	0.00	-1.0000	0.00	0.3997
	4x4	1.0000	0.00	-1.0000	0.00	0.6060
	5x5	1.0000	0.00	-1.0000	0.00	0.8679
	6x6	1.0000	0.00	-1.0000	0.00	1.2027
5x5	1x1	0.9673	3.27	-1.0000	0.00	0.2204
	2x2	0.9991	0.09	-1.0000	0.00	0.3112
	3x3	1.0000	0.00	-1.0000	0.00	0.4604
	4x4	1.0000	0.00	-1.0000	0.00	0.6677
	5x5	1.0000	0.00	-1.0000	0.00	0.9362
	6x6	1.0000	0.00	-1.0000	0.00	1.2642
6x6	1x1	0.9673	3.27	-1.0000	0.00	0.2985
	2x2	0.9991	0.09	-1.0000	0.00	0.3882
	3x3	1.0000	0.00	-1.0000	0.00	0.5335
	4x4	1.0000	0.00	-1.0000	0.00	0.7416
	5x5	1.0000	0.00	-1.0000	0.00	1.0112
	6x6	1.0000	0.00	-1.0000	0.00	1.3333

NRI : Number of Gaussian quadrature points for regular integral
NSI : Number of Gaussian quadrature points for singular integral
Exact solution : u=1.E-06, t=-1.00

Table 4.2 Beam in Uniform Tension, 4-node Quadrilateral Element: Comparison of Error for Displacement and Traction, and CPU Time

NRI	NSI	u_A ($\times 10^{-6}$)	Error (%)	t_B	Error (%)	CPU Time (second)
1	1x1	------	>100	------	>100	0.3332
	2x2	1.8007	80.07	-0.4114	58.86	0.5378
	3x3	1.8843	88.34	-0.3102	68.98	0.8721
	4x4	1.8754	87.54	-0.3153	68.47	1.3492
	5x5	1.8759	87.59	-0.3239	67.61	1.9639
	6x6	1.8776	87.76	-0.3224	67.76	2.7301
3	1x1	------	>100	------	>100	0.5478
	2x2	0.7482	25.18	-1.3980	39.80	0.7635
	3x3	0.8437	15.63	-1.2393	23.93	1.0886
	4x4	0.8473	15.27	-1.2196	21.96	1.5714
	5x5	0.8459	15.41	-1.2299	22.99	2.1947
	6x6	0.8465	15.35	-1.2291	22.91	2.9585
4	1x1	------	>100	------	>100	0.6481
	2x2	0.7151	28.49	-1.4042	40.42	0.8548
	3x3	0.8083	19.17	-1.2411	24.11	1.1982
	4x4	0.7938	20.62	-1.2162	21.62	1.6839
	5x5	0.7970	20.30	-1.2266	22.66	2.2990
	6x6	0.8002	19.98	-1.2260	22.60	3.0547
6	1x1	------	>100	------	>100	0.9212
	2x2	0.9357	6.43	-1.1711	17.11	1.1272
	3x3	1.0349	3.49	-0.9648	3.52	1.4828
	4x4	1.0286	2.86	-0.9564	4.36	1.9553
	5x5	1.0278	2.78	-0.9667	3.33	2.5755
	6x6	1.0284	2.84	-0.9653	3.47	3.3316
7	1x1	------	>100	------	>100	1.0463
	2x2	0.9252	7.48	-1.2021	20.21	1.2503
	3x3	1.0422	4.22	-0.9718	2.82	1.5904
	4x4	1.0185	1.85	-0.9836	1.64	2.0833
	5x5	1.0176	1.76	-0.9794	2.06	2.6995
12	6x6	1.0200	2.00	-0.9791	2.09	3.4563
	1x1	------	>100	------	>100	1.9069
	2x2	0.9057	9.43	-1.2149	21.49	2.1113
	3x3	0.9799	2.01	-1.0127	1.27	2.4536
	4x4	0.9926	0.74	-1.0061	0.61	2.9403
	5x5	0.9962	0.38	-1.0021	0.21	3.5512
	6x6	0.9986	0.14	-1.0017	0.17	4.3225

NRI : Number of Gaussian quadrature points for regular integral
NS I : Number of Gaussian quadrature points for singular integral
Exact solution : u=1.E-06, t=-1.00

Table 4.3 Beam in Uniform Tension, 6-node Triangular Element: Comparison of Error for Displacement and Traction, and CPU Time

NRI	NSI	u_A ($\times 10^{-6}$)	Error (%)	t_B	Error (%)	CPU Time (second)
1x1	1x1	------	>100	------	>100	0.1926
	2x2	------	>100	-0.3553	64.47	0.4299
	3x3	------	>100	-0.3430	65.70	0.8292
	4x4	------	>100	-0.3441	65.59	1.3935
	5x5	------	>100	-0.3441	65.59	2.1057
	6x6	------	>100	-0.3441	65.59	2.9901
2x2	1x1	1.1266	12.66	-0.6751	32.49	0.2595
	2x2	0.8189	18.11	-1.2086	20.86	0.4985
	3x3	0.8074	19.26	-1.2429	24.29	0.8954
	4x4	0.8086	19.14	-1.2390	23.90	1.4562
	5x5	0.8086	19.14	-1.1979	19.79	2.1756
	6x6	0.8086	19.14	-1.2497	24.97	3.0527
3x3	1x1	0.9108	8.92	-1.3704	37.04	0.3715
	2x2	1.0389	3.89	-0.9424	5.76	0.6111
	3x3	1.0228	2.28	-0.9710	2.90	1.0103
	4x4	1.0210	2.10	-0.9736	2.64	1.5556
	5x5	0.9814	1.86	-0.9738	2.62	2.2889
	6x6	1.0208	2.08	-0.9738	2.62	3.1837
4x4	1x1	0.9283	7.17	-1.3788	37.88	0.5236
	2x2	1.0187	1.87	-0.9648	3.52	0.7674
	3x3	1.0028	0.28	-0.9959	0.41	1.1598
	4x4	0.9984	0.16	-0.9984	0.16	1.7192
	5x5	0.9984	0.16	-0.9990	0.10	2.4486
	6x6	0.9984	0.16	-0.9988	0.12	3.3228
5x5	1x1	0.9278	7.22	-1.3453	34.53	0.7288
	2x2	1.0139	1.39	-0.9666	3.34	0.9667
	3x3	1.0014	0.14	-0.9971	0.29	1.3594
	4x4	0.9997	0.03	-1.0003	0.03	1.9274
	5x5	0.9997	0.03	-1.0006	0.06	2.6425
	6x6	0.9997	0.03	-1.0006	0.06	3.4846
6x6	1x1	0.9275	7.25	-1.3459	34.59	0.9826
	2x2	1.0143	1.43	-0.9660	3.40	1.2132
	3x3	1.0018	0.18	-0.9969	0.31	1.6159
	4x4	1.0002	0.02	-0.9997	0.03	2.1875
	5x5	1.0000	0.00	-1.0000	0.00	2.8705
	6x6	1.0000	0.00	-1.0000	0.00	3.7663

NRI : Number of Gaussian quadrature points for regular integral
NS I : Number of Gaussian quadrature points for singular integral
Exact solution : u=1.E-06, t=-1.00

Table 4.4 Beam in Uniform Tension, 8-node Quadrilateral Element: Comparison of Error for Displacement and Traction, and CPU Time

NRI	NSI	u_A ($\times 10^{-6}$)	Error (%)	t_B	Error (%)	CPU Time (second)
3	3x3	0.9426	5.74	-1.0365	3.65	0.6251
	4x4	0.9438	5.62	-1.0418	4.18	1.2028
	5x5	0.9438	5.62	-1.0415	4.15	0.8792
	6x6	0.9439	5.61	-1.0418	4.18	1.6006
4	3x3	0.9260	7.40	-1.0529	5.29	0.6661
	4x4	0.9272	7.28	-1.0579	5.79	0.9229
	5x5	0.9273	7.27	-1.0582	5.82	1.2458
	6x6	0.9273	7.27	-1.0582	5.82	1.6534
6	3x3	1.0034	0.34	-0.9928	0.72	0.7982
	4x4	1.0029	0.29	-0.9978	0.22	1.0496
	5x5	1.0030	0.30	-0.9981	0.19	1.3701
	6x6	1.0030	0.30	-0.9981	0.19	1.7863
7	3x3	0.9992	0.08	-0.9923	0.77	0.8463
	4x4	1.0028	0.28	-0.9972	0.28	1.0990
	5x5	1.0029	0.29	-0.9975	0.25	1.4222
	6x6	1.0028	0.28	-0.9975	0.25	1.8274
12	3x3	0.9974	0.26	-0.9948	0.52	1.2506
	4x4	1.0000	0.00	-0.9997	0.03	1.5061
	5x5	1.0000	0.00	-1.0000	0.00	1.8256
	6x6	1.0000	0.00	-1.0000	0.00	2.2321
13	3x3	0.9974	0.26	-0.9948	0.52	1.3041
	4x4	1.0000	0.00	-1.0000	0.00	1.5561
	5x5	1.0000	0.00	-1.0000	0.00	1.8756
	6x6	1.0000	0.00	-1.0000	0.00	2.2818

NRI : Number of Gaussian quadrature points for regular integral
NS I : Number of Gaussian quadrature points for singular integral
Exact solution : u=1.E-06, t=-1.00

Table 4.5 Beam in Uniform Tension, 3-node Triangular Element, Double Region: Comparison of Error for Displacement and Traction, and CPU Time

NRI	NSI	u_A ($\times 10^{-6}$)	Error (%)	t_B	Error (%)	CPU Time (second)
3x3	3x3	1.0017	0.17	-1.0000	0.00	0.8452
	4x4	1.0017	0.17	-1.0000	0.00	1.3190
	5x5	1.0017	0.17	-1.0000	0.00	1.9215
	6x6	1.0017	0.17	-1.0000	0.00	2.6509
4x4	3x3	1.0000	0.00	-1.0000	0.00	0.9502
	4x4	1.0000	0.00	-1.0000	0.00	1.4150
	5x5	1.0000	0.00	-1.0000	0.00	2.0153
	6x6	1.0000	0.00	-1.0000	0.00	2.7682
5x5	3x3	1.0000	0.00	-1.0000	0.00	1.0912
	4x4	1.0000	0.00	-1.0000	0.00	1.5542
	5x5	1.0000	0.00	-1.0000	0.00	2.1523
	6x6	1.0000	0.00	-1.0000	0.00	2.8998
6x6	3x3	1.0000	0.00	-1.0000	0.00	1.2692
	4x4	1.0000	0.00	-1.0000	0.00	1.7257
	5x5	1.0000	0.00	-1.0000	0.00	2.3466
	6x6	1.0000	0.00	-1.0000	0.00	3.0907

NRI : Number of Gaussian quadrature points for regular integral
NS I : Number of Gaussian quadrature points for singular integral
Exact solution : u=1.E-06, t=-1.00

Table 4.6 Beam in Uniform Tension, 4-node Quadrilateral Element, Double Region: Comparison of Error for Displacement and Traction, and CPU Time

NRI	NSI	u_A ($\times 10^{-6}$)	Error (%)	t_B	Error (%)	CPU Time (second)
4	3x3	0.7582	24.18	-1.2355	23.55	2.3109
	4x4	0.7391	26.09	-1.2142	21.42	3.2921
	5x5	0.7420	25.80	-1.2183	21.83	4.5192
	6x6	0.7448	25.52	-1.2182	21.82	6.0571
6	3x3	1.0412	4.12	-0.9650	3.50	2.8737
	4x4	1.0299	2.99	-0.9536	4.64	3.8452
	5x5	1.0304	3.04	-0.9646	3.54	5.0775
	6x6	1.0311	3.11	-0.9638	3.62	6.6007
7	3x3	1.0458	4.58	-1.0546	5.46	3.1014
	4x4	1.0212	2.12	-1.0357	3.57	4.0894
	5x5	1.0236	2.36	-1.0441	4.41	5.2954
	6x6	1.0257	2.57	-1.0443	4.43	6.8005
12	3x3	1.0197	1.97	-1.0087	0.87	4.8588
	4x4	0.9932	0.68	-0.9881	1.19	5.8394
	5x5	0.9968	0.32	-1.0017	0.17	7.0863
	6x6	0.9991	0.09	-0.9994	0.06	8.5758
13	3x3	1.0192	1.92	-1.0086	0.86	5.1568
	4x4	0.9928	0.72	-0.9883	1.17	6.1327
	5x5	0.9964	0.36	-0.9948	0.52	7.3690
	6x6	0.9987	0.13	-0.9984	0.16	8.8721

NRI : Number of Gaussian quadrature points for regular integral
NS I : Number of Gaussian quadrature points for singular integral
Exact solution : u=1.E-06, t=-1.00

Table 4.7 Beam in Uniform Tension, 6-node Triangular Element, Double Region: Comparison of Error for Displacement and Traction, and CPU Time

NRI	NSI	u_A ($\times 10^{-6}$)	Error (%)	t_B	Error (%)	CPU Time (second)
3x3	3x3	1.0179	1.79	-0.9653	3.47	1.9954
	4x4	1.0170	1.70	-0.9680	3.20	3.1194
	5x5	1.0170	1.70	-0.9683	3.17	4.5595
	6x6	1.0169	1.69	-0.9683	3.17	6.3246
4x4	3x3	1.0017	1.70	-0.9955	0.45	2.3013
	4x4	1.0012	0.12	-0.9986	0.14	3.4235
	5x5	1.0012	0.12	-0.9988	0.12	4.8600
	6x6	1.0012	0.12	-0.9989	0.11	6.6606
5x5	3x3	1.0006	0.12	-0.9973	0.27	2.7091
	4x4	0.9999	0.01	-1.0004	0.04	3.8227
	5x5	0.9996	0.04	-1.0007	0.07	5.2572
	6x6	0.9996	0.04	-1.0007	0.07	7.0385
6x6	3x3	0.9993	0.07	-0.9966	0.34	3.2110
	4x4	1.0000	0.00	-0.9997	0.03	4.3337
	5x5	1.0000	0.00	-1.0000	0.00	5.7791
	6x6	1.0000	0.00	-1.0000	0.00	7.5443

NRI : Number of Gaussian quadrature points for regular integral
NS I : Number of Gaussian quadrature points for singular integral
Exact solution : u=1.E-06, t=-1.00

Table 4.8 Beam in Uniform Tension, 8-node Quadrilateral Element, Double Region: Comparison of Error for Displacement and Traction, and CPU Time

4.2 Beam Subjected to Pure Bending

The problem of a beam in pure bending was solved to investigate the convergence of each element as a function of number of elements used. The geometry and boundary conditions are shown in Figure 4.6. For each element, three different meshes were used as shown in Figures 4.7 to 4.10. The exact solution for the displacements are [31]

$$u_x = \frac{\nu M}{EI} xy$$

$$u_y = -\frac{M}{EI}\left(z^2 - \nu x^2 + \nu y^2 \right)$$

$$u_z = \frac{M}{EI} yz \qquad (4.2)$$

and the traction at point B in Figure 4.6 is

$$t_z = \sigma \qquad (4.3)$$

where M is the applied moment and I is the moment of inertia with respect to the z axis. The displacements at point A and the traction in direction z at point B are compared with these exact solutions. The results are listed in Tables 4.9 to 4.12. The 3-node triangular element and 4-node quadrilateral element do not converge to

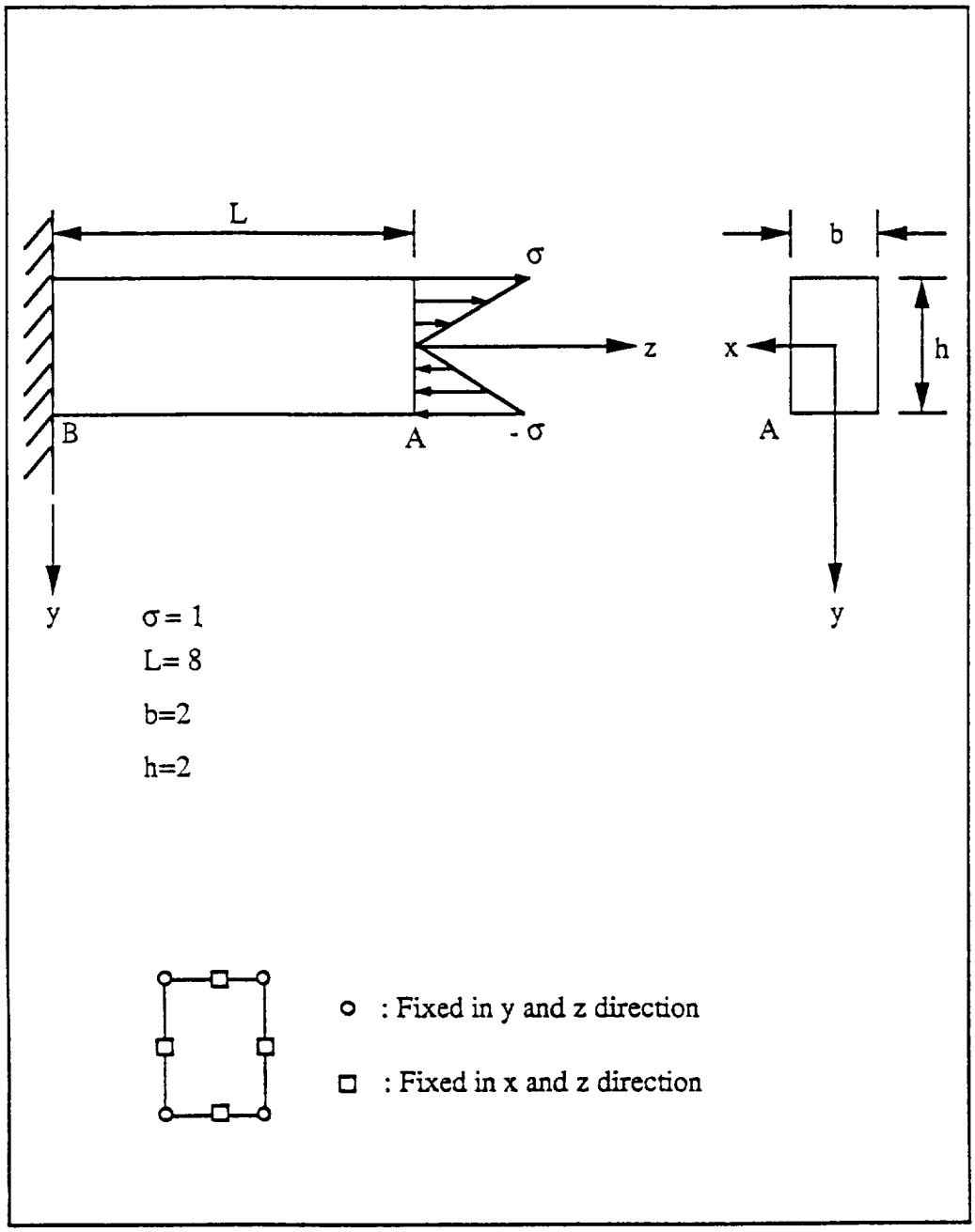

Figure 4.6 Geometry and Boundary Conditions for Beam in Pure Bending

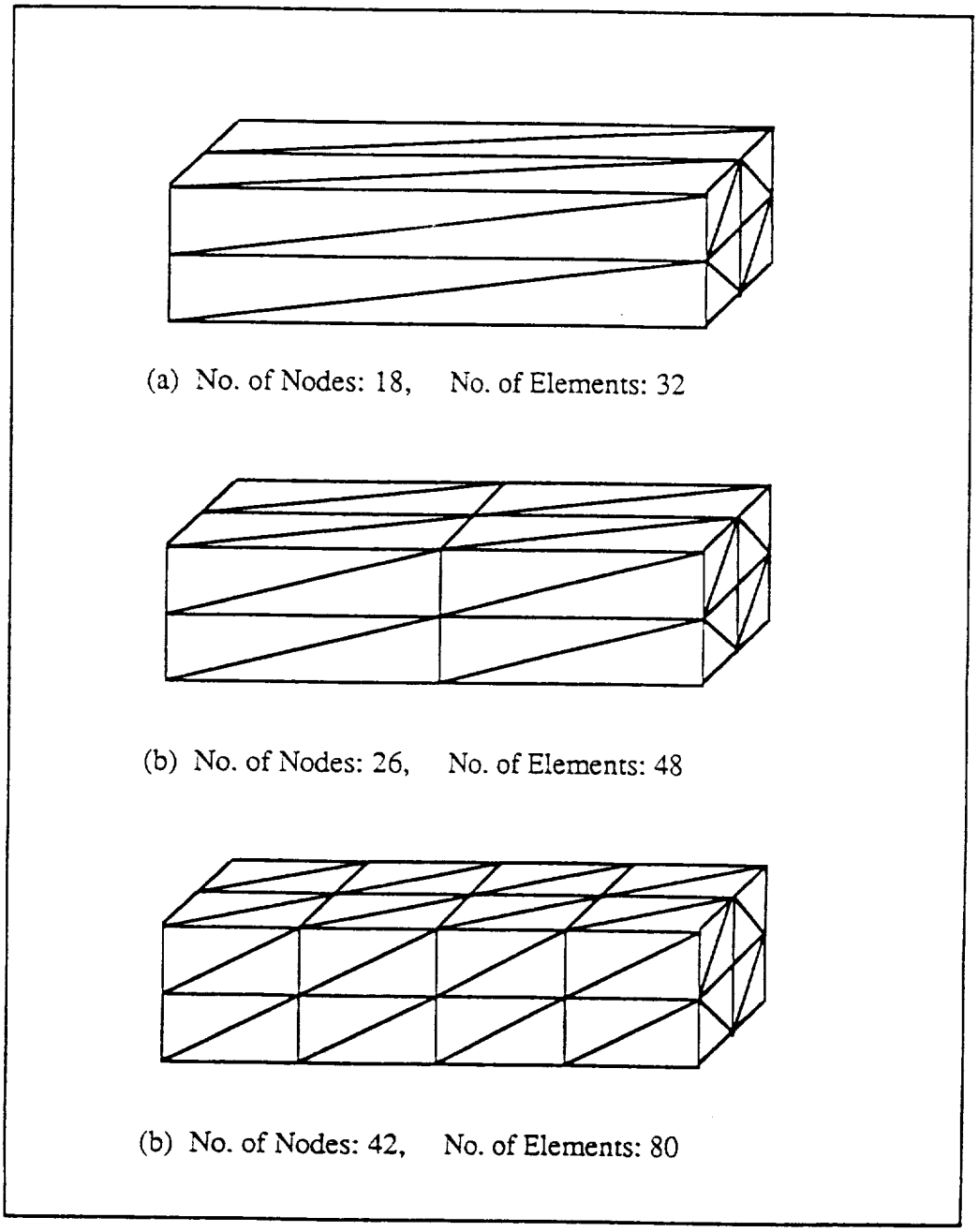

Figure 4.7 3-Node Triangular Element Meshes for Beam in Pure Bending

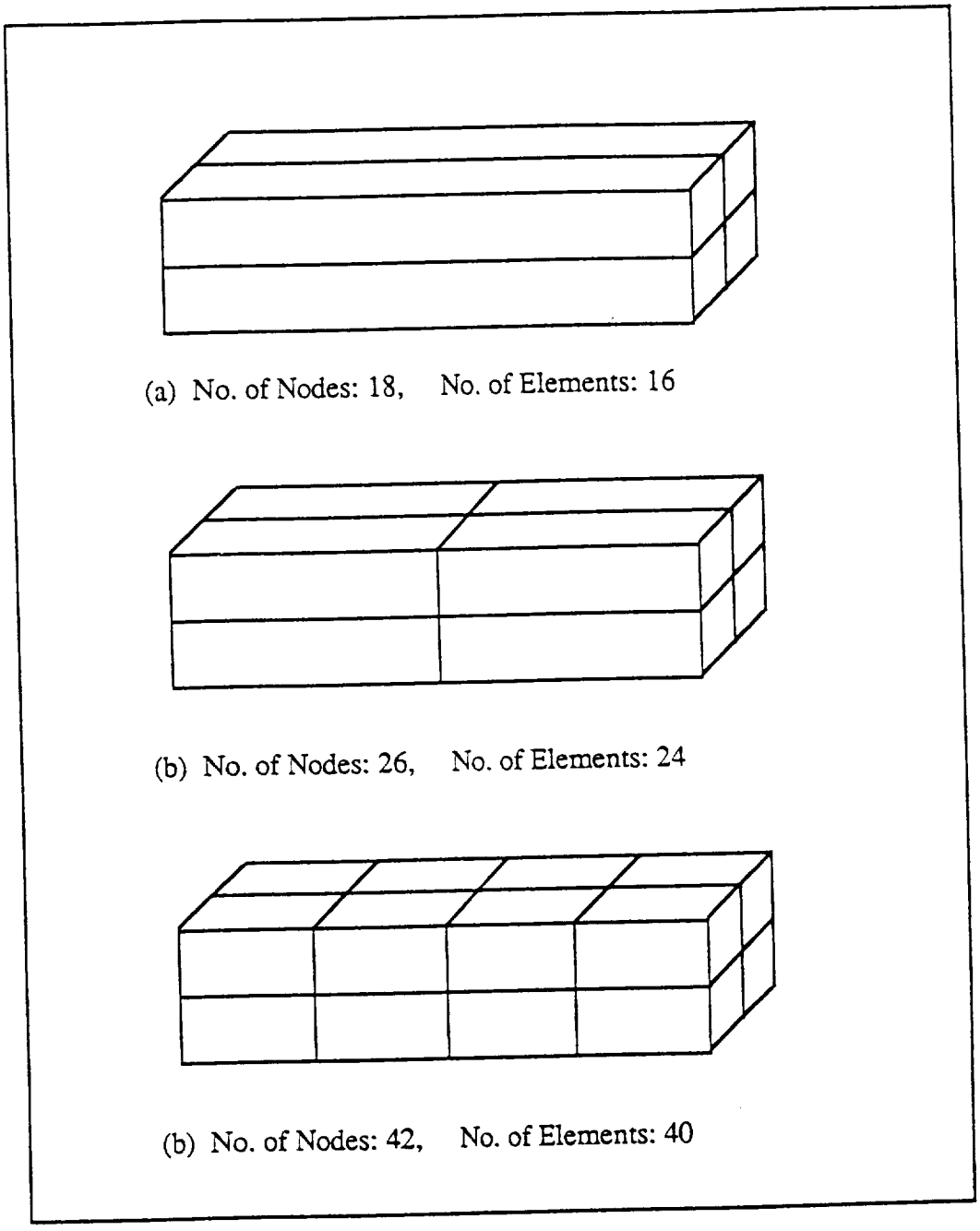

(a) No. of Nodes: 18, No. of Elements: 16

(b) No. of Nodes: 26, No. of Elements: 24

(b) No. of Nodes: 42, No. of Elements: 40

Figure 4.8 4-Node Quadrilateral Element Meshes for Beam in Pure Bending

Mesh (fig.)	NRI	NSI	$u_x(\times 10^{-7})$	Error (%)	$u_y(\times 10^{-5})$	Error (%)	$u_z(\times 10^{-6})$	Error (%)	t_z	Error (%)	CPU Time (second)
4.7a	13	6x6	------	>100	------	>100	------	>100	------	>100	7.3314
4.7b	13	6x6	0.8091	19.09	1.3224	24.16	-3.1664	18.74	0.3257	67.43	16.4664
4.7c	13	6x6	0.8679	13.21	1.2312	15.42	-2.9395	10.23	0.5768	42.32	48.2012

NRI : Number of Gaussian quadrature points for regular integral

NS I : Number of Gaussian quadrature points for singular integral

Exact solution : u_x= 1.00000E-07, u_y = 1.06667E-05, u_z = -2.66667E-06, t_z = 1.00

Table 4.9 Beam in Pure Bending, 3-node Triangular Element:Comparison of Error for Displacements and Traction, and CPU Time

Mesh (fig.)	NRI	NSI	$u_x(\times 10^{-7})$	Error (%)	$u_y(\times 10^{-5})$	Error (%)	$u_z(\times 10^{-6})$	Error (%)	t_z	Error (%)	CPU Time (second)
4.8a	6x6	6x6	------	>100	------	>100	------	>100	1.8042	80.42	16.8100
4.8b	6x6	6x6	0.5468	45.32	1.5602	46.27	-3.8483	44.31	1.5024	50.24	25.5960
4.8c	6x6	6x6	0.9007	9.93	1.1810	10.72	-2.9101	9.13	1.3896	38.96	61.4273

NRI : Number of Gaussian quadrature points for regular integral

NS I : Number of Gaussian quadrature points for singular integral

Exact solution : u_x= 1.00000E-07, u_y = 1.06667E-05, u_z = -2.66667E-06, t_z = 1.00

Table 4.10 Beam in Pure Bending, 4-node Quadrilateral Element:Comparison of Error for Displacementsand Traction, and CPU Time

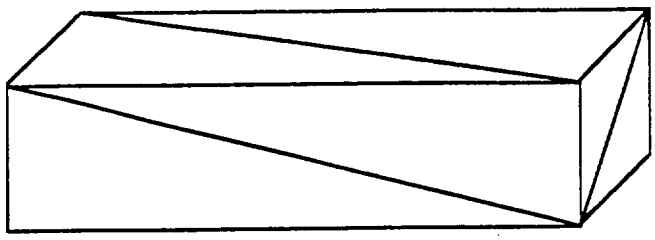

(a) No. of Nodes: 26, No. of Elements:12

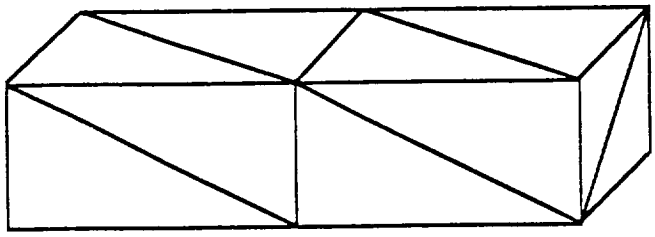

(b) No. of Nodes: 42, No. of Elements: 20

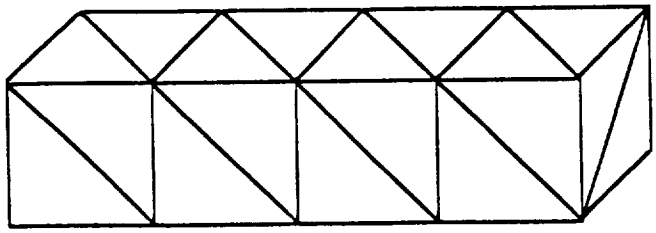

(b) No. of Nodes: 74, No. of Elements: 36

Figure 4.9 6-Node Triangular Element Meshes for Beam in Pure Bending

Mesh (fig.)	NRI	NSI	$u_x(\times 10^{-7})$	Error (%)	$u_y(\times 10^{-5})$	Error (%)	$u_z(\times 10^{-6})$	Error (%)	t_z	Error (%)	CPU Time (second)
4.11.a	12	5x5	0.9455	5.45	0.9953	6.69	-2.5350	4.94	0.8957	10.43	3.4184
	13	6x6	0.9474	5.26	1.1020	3.31	-2.7315	2.43	0.8889	11.11	4.2770
4.11.b	12	5x5	1.0049	4.49	1.0832	1.55	-2.8473	6.77	1.0114	1.14	8.0072
	13	6x6	1.0067	0.67	1.0881	2.00	-2.6985	1.19	1.0156	1.56	9.6098
4.11.c	6	3x3	1.0075	0.75	0.9940	6.81	-2.5789	3.29	1.0286	2.86	11.1545
		4x4	1.0062	0.62	1.0742	0.71	-2.7402	2.76	1.0233	2.33	12.6157
		5x5	1.0090	0.90	1.0825	1.48	-2.7159	1.85	1.0254	2.54	14.4747
		6x6	1.0087	0.87	1.0729	0.58	-2.7042	1.41	1.0138	1.38	16.7805
	7	3x3	0.9993	0.07	0.9850	7.66	-2.5578	4.08	1.0191	1.91	12.4066
		4x4	0.9968	0.32	1.0652	0.13	-2.7192	1.97	1.0025	0.25	13.8485
		5x5	0.9991	0.09	1.0729	0.58	-2.6974	1.05	1.0038	0.38	15.7151
		6x6	0.9991	0.09	1.0633	0.32	-2.6829	0.61	0.9924	0.76	17.9984
	12	3x3	1.0028	0.28	0.9951	6.71	-2.5535	4.24	0.9818	1.82	21.2357
		4x4	0.9996	0.04	1.0733	0.62	-2.7086	1.57	1.0186	1.86	22.5984
		5x5	1.0014	0.14	1.0783	1.09	-2.6783	0.44	1.0144	1.44	24.4300
		6x6	1.0016	0.16	1.0696	0.27	-2.6684	0.06	1.0044	0.44	26.7404
	13	3x3	1.0033	0.33	0.9956	6.66	-2.5543	4.21	0.9830	1.70	22.5775
		4x4	1.0087	0.87	1.0740	0.69	-2.7099	1.62	1.0196	1.96	23.9937
		5x5	1.0021	0.21	1.0792	1.17	-2.6797	0.49	1.0155	1.55	25.8158
		6x6	1.0022	0.22	1.0703	0.34	-2.6698	0.12	1.0054	0.54	28.0484

NRI : Number of Gaussian quadrature points for regular integral

NS I : Number of Gaussian quadrature points for singular integral

Exact solution : $u_x = 1.00000E\text{-}07$, $u_y = 1.06667E\text{-}05$, $u_z = -2.66667E\text{-}06$, $t_z = 1.00$

Table 4.11 Beam in Pure Bending, 6-node Triangular Element :Comparison of Error for Displacements and Traction, and CPU Time

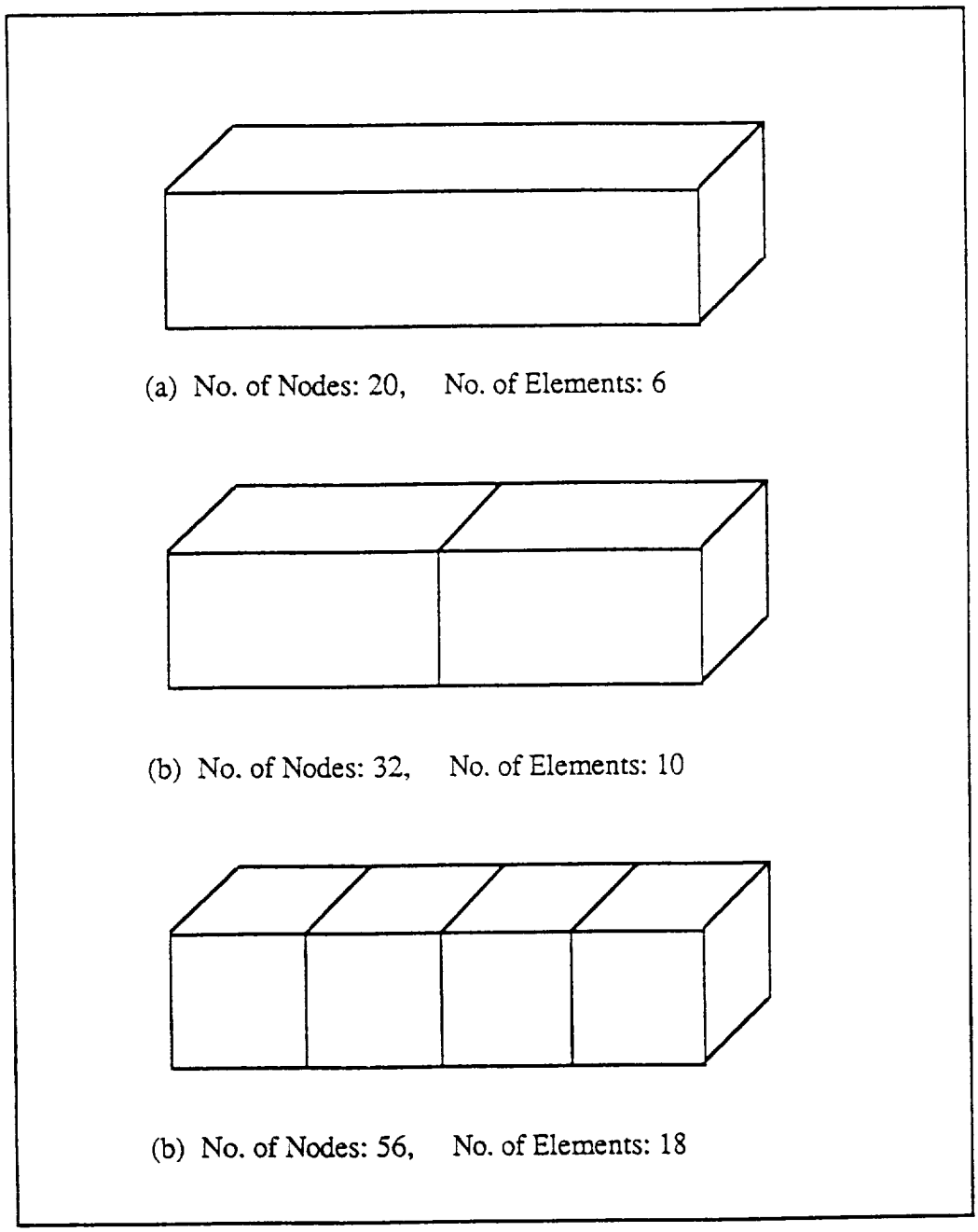

Figure 4.10 8-Node Quadrilateral Element Meshes for Beam in Pure Bending

Mesh (fig.)	NRI	NSI	$u_x(\times 10^{-7})$	Error (%)	$u_y(\times 10^{-5})$	Error (%)	$u_z(\times 10^{-6})$	Error (%)	t_z	Error (%)	CPU Time (second)
4.12.a	6x6	6x6	------	>100	------	>100	------	>100	1.0018	0.18	3.7343
4.12.b	4x4	4x4	1.0143	1.43	1.1099	4.05	-2.7466	2.92	1.0356	3.56	3.5880
	5x5	5x5	1.0066	0.66	1.0661	0.05	-2.6649	0.07	1.0068	0.68	5.4499
	6x6	6x6	0.9994	0.06	1.0646	0.19	-2.6630	0.14	0.9977	0.23	7.7781
4.12.c	3x3	3x3	1.0091	0.91	1.0943	2.59	-2.7221	2.07	1.0236	2.36	5.6464
		4x4	1.0115	1.15	1.0967	2.82	-2.7262	2.23	1.0219	2.19	7.3205
		5x5	1.0118	1.18	1.0966	2.81	-2.7261	2.23	1.0213	2.13	9.4597
		6x6	1.0119	1.19	1.0966	2.81	-2.7261	2.23	1.0212	2.12	12.1219
	4x4	3x3	0.9961	0.39	1.0578	0.83	-2.6505	0.61	0.9945	0.55	7.5160
		4x4	0.9984	0.16	1.0599	0.63	-2.6541	0.47	0.9915	0.85	9.2054
		5x5	0.9987	0.13	1.0598	0.64	-2.6539	0.48	0.9922	0.78	11.3726
		6x6	0.9988	0.12	1.0598	0.64	-2.6539	0.48	0.9922	0.78	14.0521
	5x5	3x3	0.9972	0.28	1.0648	0.18	-2.6634	0.12	1.0030	0.30	9.9432
		4x4	0.9996	0.04	1.0669	0.02	-2.6671	0.02	0.9995	0.05	11.6219
		5x5	0.9999	0.01	1.0669	0.02	-2.6670	0.01	1.0001	0.01	13.8086
		6x6	0.9999	0.01	1.0668	0.01	-2.6669	0.01	1.0001	0.01	16.4239
	6x6	3x3	0.9973	0.27	1.0647	0.18	-2.6634	0.12	1.0026	0.26	12.9395
		4x4	0.9997	0.03	1.0669	0.02	-2.6671	0.02	0.9995	0.05	14.5802
		5x5	1.0000	0.00	1.0668	0.01	-2.6670	0.01	1.0002	0.02	16.7482
		6x6	1.0000	0.00	1.0668	0.01	-2.6669	0.01	1.0001	0.01	19.4238

NRI : Number of Gaussian quadrature points for regular integral

NS I : Number of Gaussian quadrature points for singular integral

Exact solution : u_x = 1.00000E-07, u_y = 1.06667E-05, u_z = -2.66667E-06, t_z = 1.00

Table 4.12 Beam in Pure Bending, 8-node Quadrilateral Element :Comparison of Error for Displacements and Traction, and CPU Time

the exact solution even for the highest order of Gaussian quadrature and for the finest mesh. These results lead to the conclusion that the linear elements should not be used for problems in which the order of traction and displacement distributions are higher than linear. The 6-node triangular element and 8-node quadrilateral element both converge to the exact solutions either by increasing the number of Gaussian quadrature points or by refining the mesh. It is also concluded that the 8-node element is superior to the 6-node element. In order to obtain results with less than 1% error in both the traction and displacement, the 6-node element requires at least 17.9984 seconds using the 7 point Gaussian quadrature for the regular integral and 6x6 for the singular integral on the 42 node mesh but the 8-node element only needs 7.5160 seconds by choosing 4x4 Gaussian quadrature for the regular integral and 3x3 for the singular integral on the 56 node mesh.

The multi-domain technique was also applied using the 8-node element. Two different meshes were tested, as shown in Figure 4.11. The results in Table 4.13 show that the double region mesh can achieve an equivalent accuracy by consumming less CPU time than that the single domain mesh does. This is because the system matrices for the two subregions are, in fact, separated and thus for the same number of nodes the double region mesh needs less calculation than the single domain mesh.

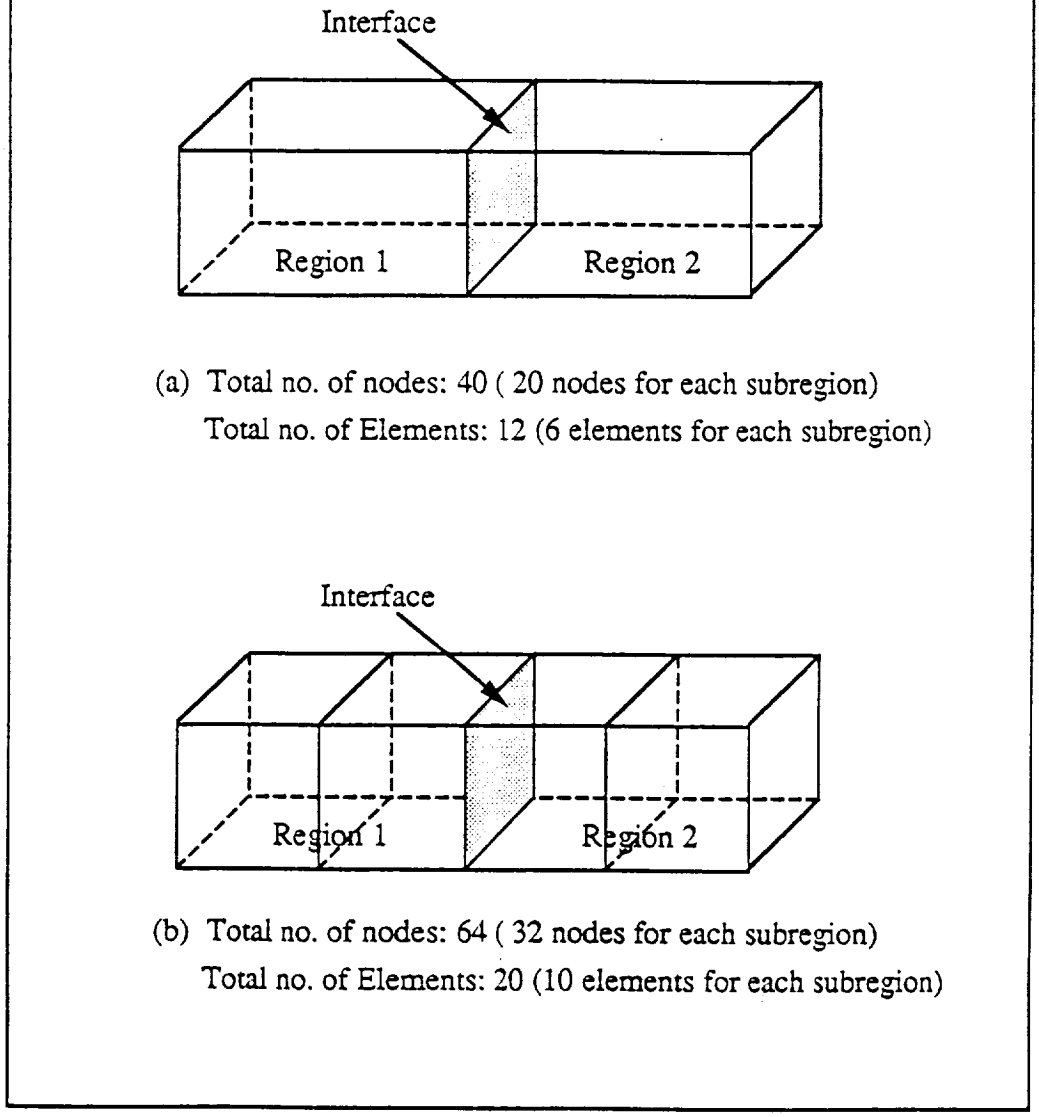

Figure 4.11 8-Node Quadrilateral Element, Two-Subregion Meshes for Beam in Pure Bending

Mesh (fig.)	NRI	NSI	$u_x(\times 10^{-7})$	Error (%)	$u_y(\times 10^{-5})$	Error (%)	$u_z(\times 10^{-6})$	Error (%)	t_z	Error (%)	CPU Time (second)
4.11a	3x3	3x3	1.0091	0.91	1.0904	2.22	-2.7162	1.86	1.0169	1.69	4.0336
	4x4	4x4	0.9982	0.18	1.0584	0.78	-2.6525	0.53	0.9889	1.11	0.9223
	5x5	5x5	0.9999	0.01	1.0671	0.04	-2.6673	0.02	1.0011	0.11	8.1955
	6x6	6x6	1.0000	0.00	1.0668	0.01	-2.6669	0.01	1.0001	0.01	15.2171
4.12b	4x4	4x4	1.0145	1.45	1.1132	4.36	-2.7496	3.11	1.0529	5.29	3.4141
	5x5	5x5	1.0065	0.65	1.0661	0.05	-2.6648	0.07	0.9955	0.45	5.2490
	6x6	6x6	0.9994	0.06	1.0663	0.03	-2.6671	0.02	0.9973	0.27	7.5234

NRI : Number of Gaussian quadrature points for regular integral

NS I : Number of Gaussian quadrature points for singular integral

Exact solution : u_x= 1.00000E-07, u_y = 1.06667E-05, u_z= -2.66667E-06, t_z = 1.00

Table 4.13 Beam in Pure Bending, 8-node Quadrilateral Element, Double Region:Comparison of Error for Displacements and Traction, and CPU Time

4.3 Circular Buried Crack Under Uniform Tension

The stress intensity factor of a circular crack buried in an infinite body subjected to far field uniform distributed traction is studied in this section. The exact solution is [32]

$$K_I = 2\sigma\sqrt{\frac{a}{\pi}} \tag{4.4}$$

where σ is the applied stress and a is the crack radius. For this problem K_{II} and K_{III} are zero since the load is perpendicular to the crack surface. Six different meshes with either different number of nodes or different boundary conditions were studied. The overall dimensions of these meshes were chosen large enough to simulate the infinite medium.

The first mesh is a two-subregion model which describes the whole domain of the problem. Each subregion consists of 52 elements and 150 nodes in which 88 nodes belong to the interface which bonds the two subregions as shown in Figure 4.12. The crack face which is kept traction free. Each crack face is formed by eight 8-node quadrilateral quarter point elements and eight 6-node triangular elements. Traction singular elements are placed along the crack front. The uniform distributed tractions σ in direction z are applied on the plane parallel to the interface plane of one subregion mesh, and the same plane for another subregion is then fixed in the z-direction with node A fixed in direction x and node B fixed in

C-2

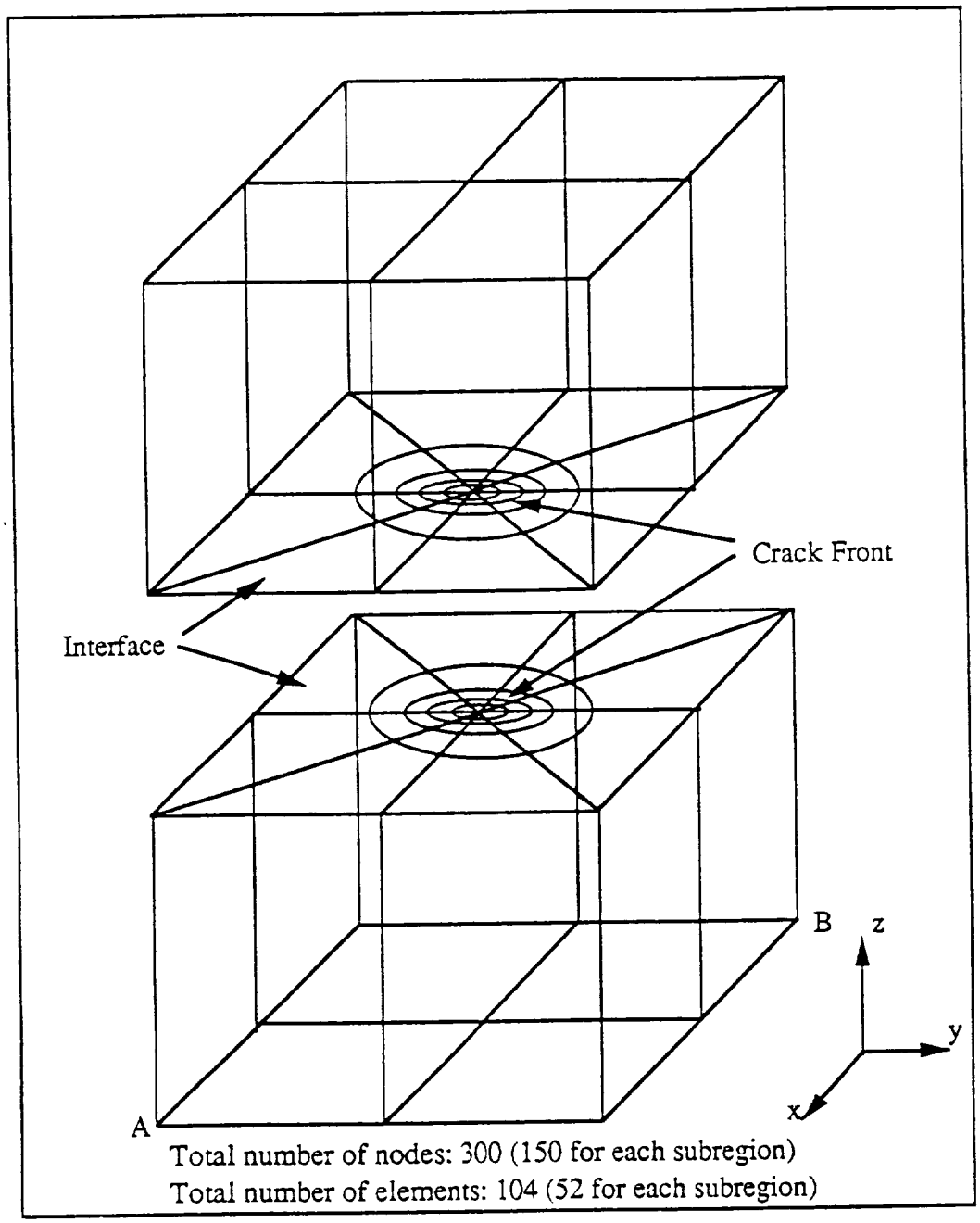

Figure 4.12 Element Mesh of Double Region Model for Buried Circular Crack

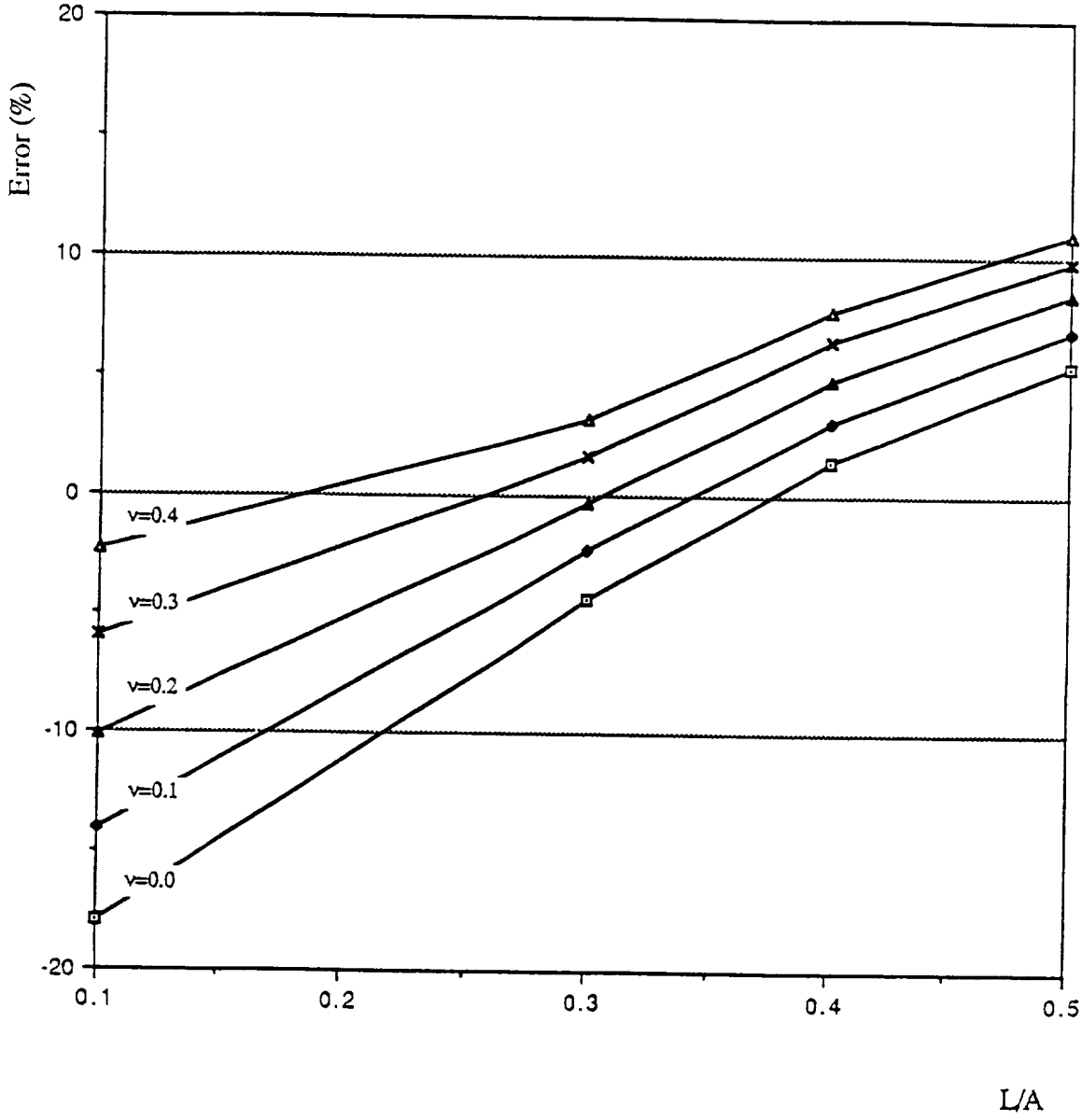

Fig.4.13 Average Error in Computed KI by Different L/A for Varied Poisson Ratio

direction y, as showm in Fig.4.12, to prevent rigid body translation and rotation. Ingraffea and Mann [33] pointed out that the ratio of the length L of the crack front element to the crack length a affects the accuracy of the results. Therefore, convergence for different L/a ratios under varied Poisson's ratio ν was studied first. Five different ratios of L/a varying from 0.1 to 0.5 were applied for Poisson's ratios varying from 0.0 to 0.4. The results are shown in Figure 4.13 revealing that the absolute error is confined to within 5% when the ratio of L/a is in between 0.26 and 0.34 for Poisson's ratios ranging from 0.1 to 0.4. Thus, the ratio of L/a of the models used in this paper is chosen to be 0.3.

In the second example the problem is modeled using the coarse double region mesh shown in Figure 4.14. It consists of 73 nodes and 25 elements. The ratio of L/a is 0.3. The maximum error in the calculated K_I was found to be 0.23%. The CPU time for this case was 31 seconds.

The third and fourth meshes used are the same as the ones above except that only half of the subregion is taken into consideration. The nodes belonging to the interface are now constrained in the z-direction as shown in Figure 4.15 and 4.16 to simulate the correct symmetric boundary conditions. The calculated K_I is almost constant along the crack front and the absolute errors were 1.6% and 0.27% for the mesh of Figure 4.15 and the mesh in Figure 4.16, respectively. The CPU times were 71 seconds and 20 seconds, respectively.

The fifth mesh is the half cut of the third mesh with an additional cut plane y=0 which is fixed in the y-direction as shown in Figure 4.17. The 6-node triangular elements around the crack tip on this cut plane are converted to be traction

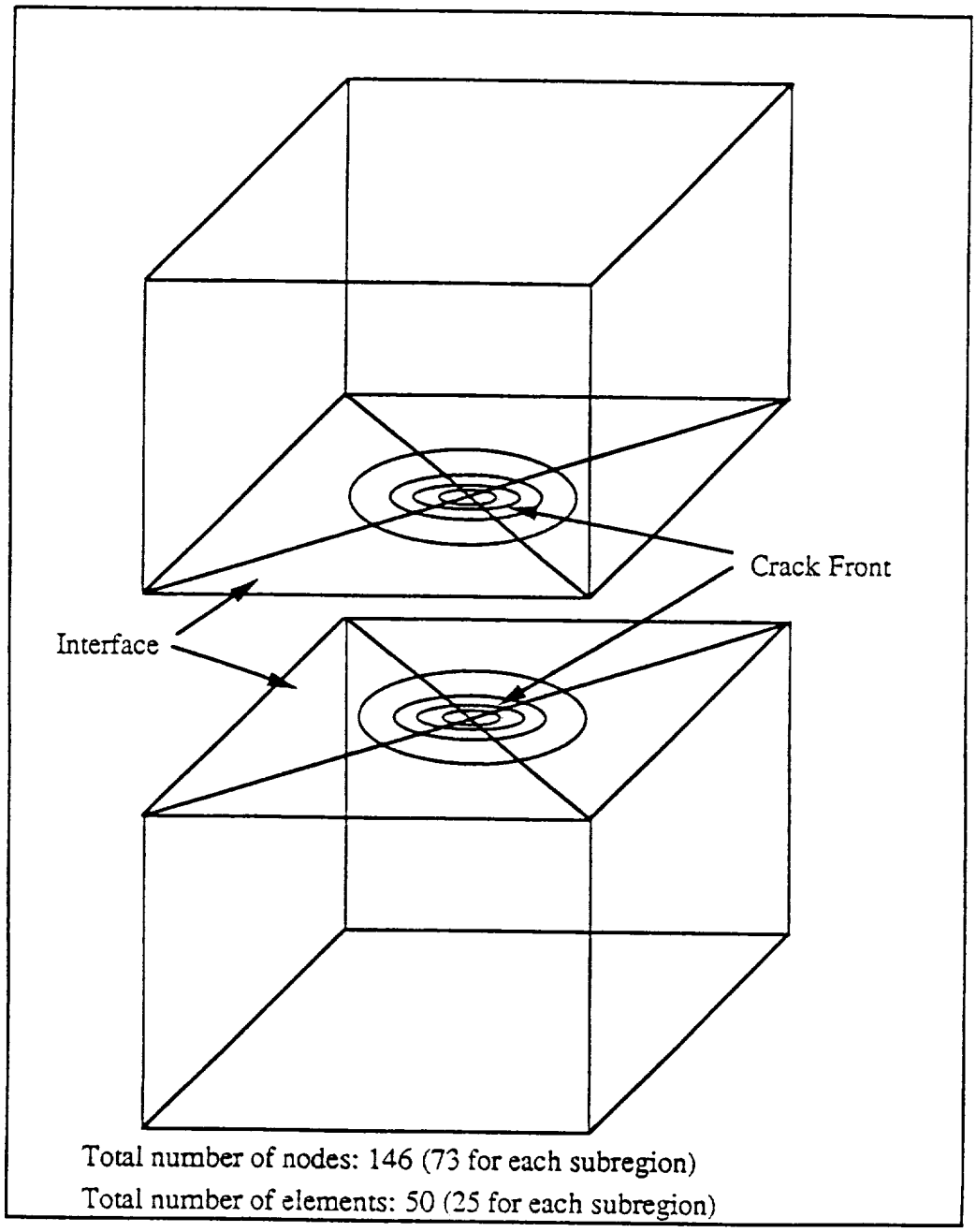

Figure 4.14 Element Mesh of Double Region Model for Buried Circular Crack

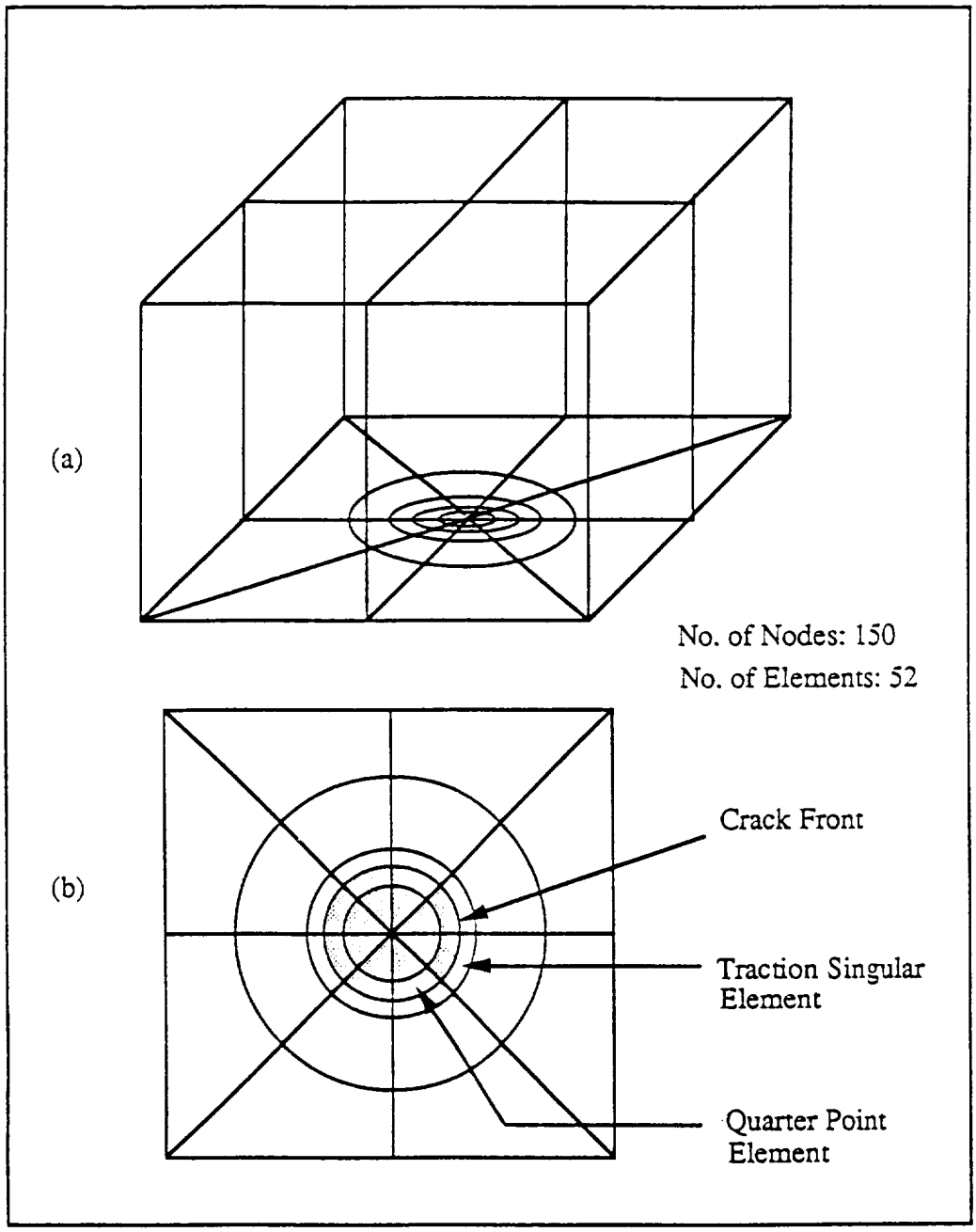

Figure 4.15 (a) Element Mesh for Half Domain of Buried Circular Crack
(b) Illustration of Elements around Crack

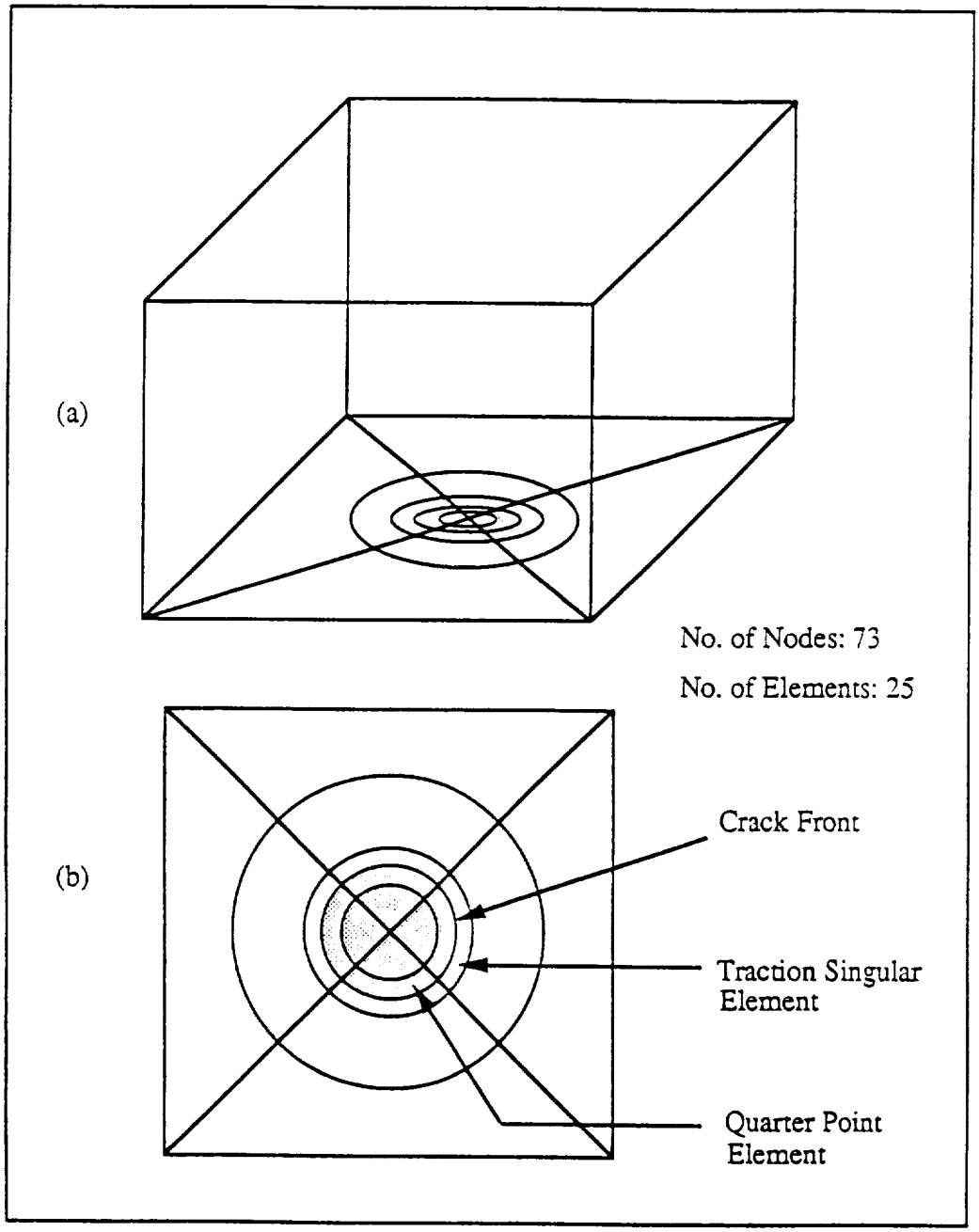

Figure 4.16 (a) Element Mesh for Half Domain of Buried Circular Crack
(b) Illustration of Elements around Crack

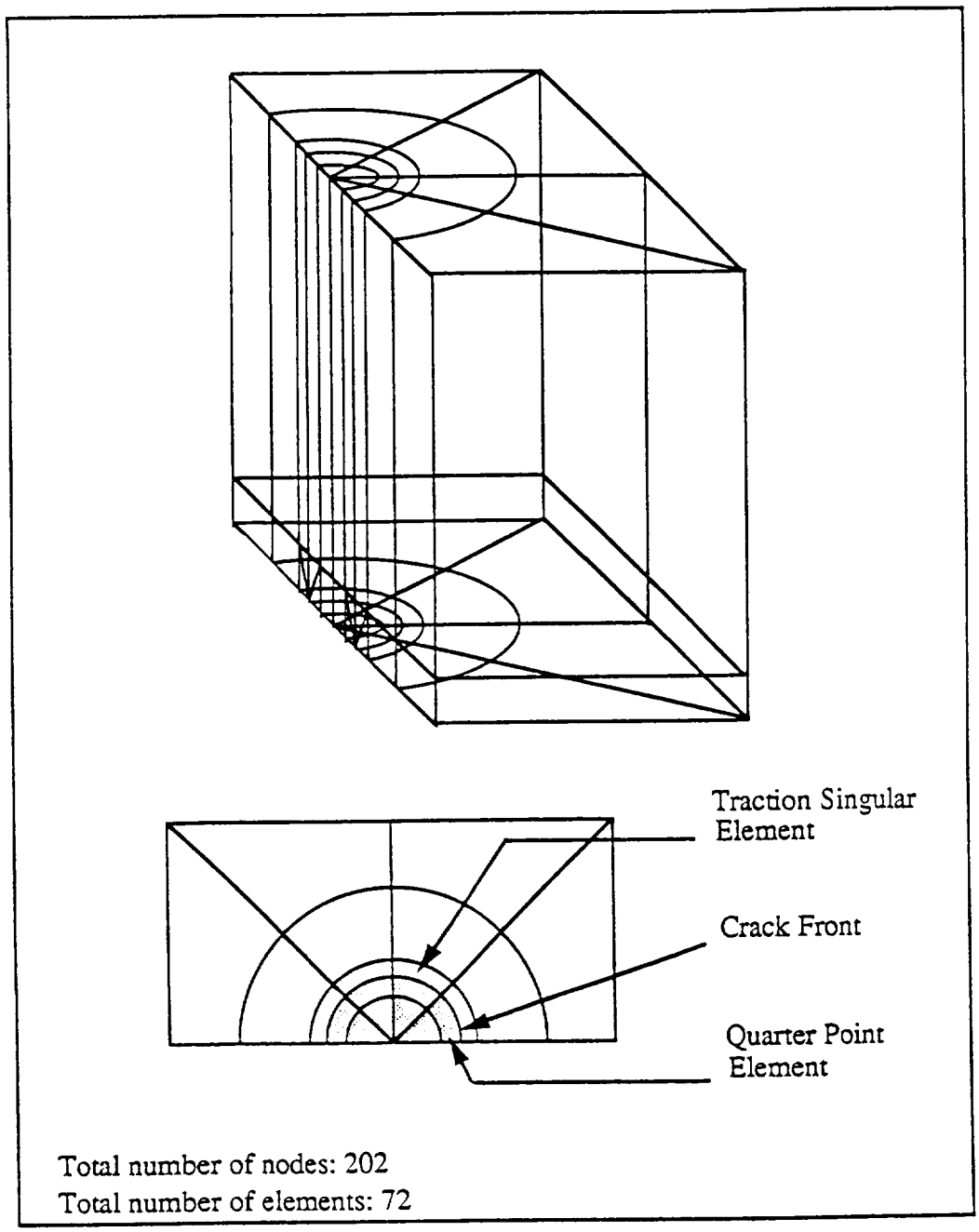

Figure 4.17 Element Mesh of Quarter Domain for Buried Circular Crack

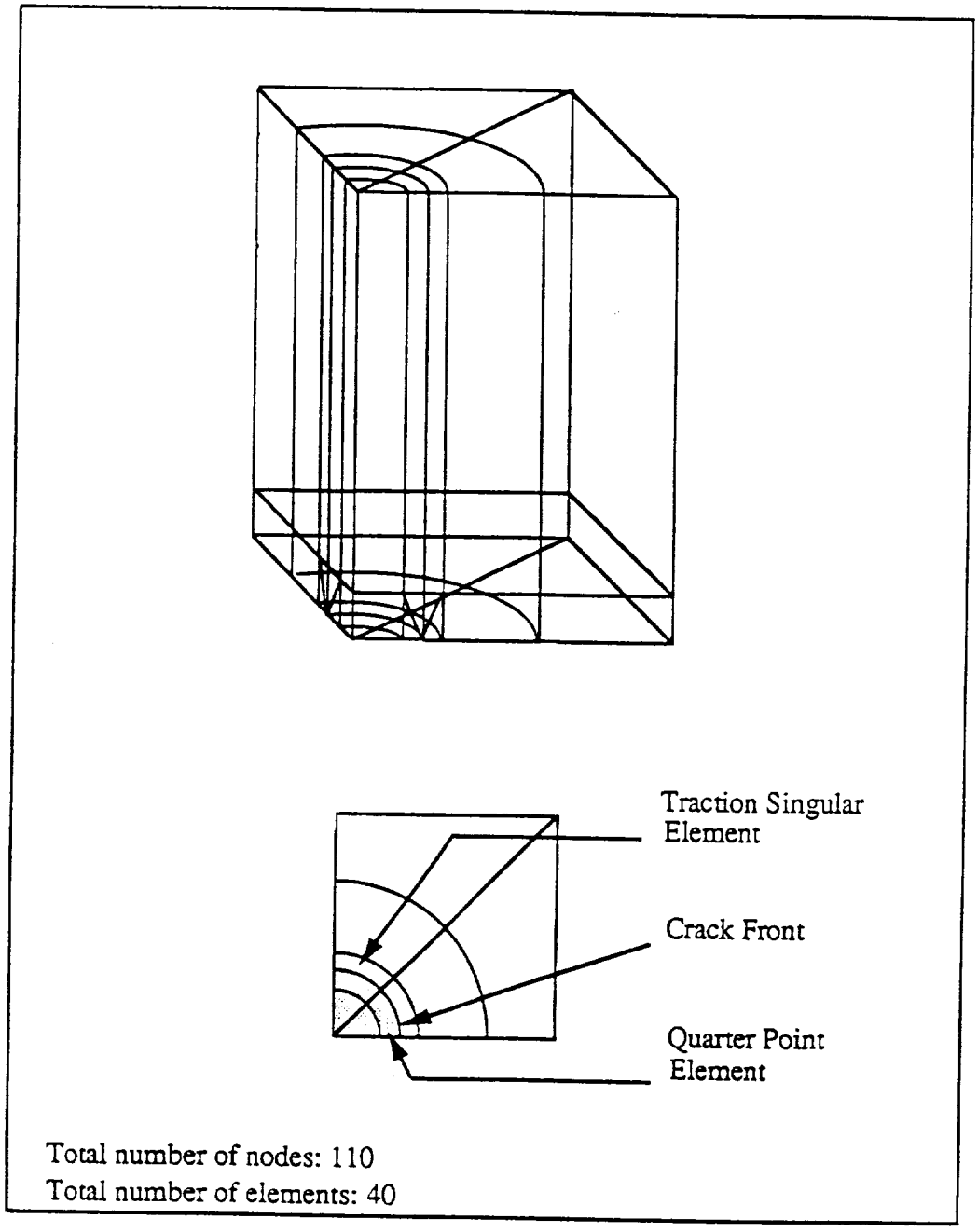

Figure 4.18 Element Mesh of One-Eighth Domain for Buried Circular Crack

Mesh (fig.)	4.12	4.14	4.15	4.16	4.17	4.18
Mesh Type	Double Region	Double Region	Single Region	Single Region	Single Region	Single Region
No. of Node	300	146	150	73	202	110
No. of Element	104	50	52	25	72	40
K_I	1.14604	1.13101	1.14647	1.13141	1.15534	1.15659
Error (%)	1.6	0.23	1.6	0.27	2.4	2.5
CPU Time (Second)	131	31	71	20	133	41

Exact solution : $K_I = 1.128379$
where crack radius a=1, applied stress σ=1.

Table 4.14 Circular Crack Buried in Infinite Body Under Uniform Tension: Comparison of Error for K_I and CPU Time for Different Meshes

singular elements by relocating their middle nodes on the two sides to the quarter position to capture the inverse square root singularity in stresses. This mesh is composed of 202 nodes and 72 elements. The differences between the analytic solution of K_I and the calculated results ranged from 1.2% to 2.3%. This mesh uses 133 seconds of CPU time.

The final mesh models one-eighth of the domain. Three planes, x=0, y=0, and z=0, are fixed in the x, y, and z direction, respectively, to represent the correct boundary conditions. The maximum error in K_I is 2.5%.

The results of this section are summarized in Table 4.14. From the table we also observe that the last two cases which model only part of the whole domain have the largest error. This is probably due to the asymmetry of the meshes. Suprisingly, the coarsest mesh (73 nodes) leads to the most accurate result. Since the K_I is constant along the crack front and the quadratic element on both side of the crack front can model the circular shape exactly, an accurate result can still be obtained by using only a few elements to model the crack. This also counts for the reason that the coarsest mesh can have such excellent results.

4.4 Circular Buried Crack Inclined at 30 Degrees Under Uniform Tension

This problem is used to ensure the ability of the Boundary Element Method to calculate stress intensity factors for mixed mode fracture problems. A circular crack deforms in three modes when the normal of the crack surface is not parallel to the direction of the applied load. The exact solutions for the stress intensity factors

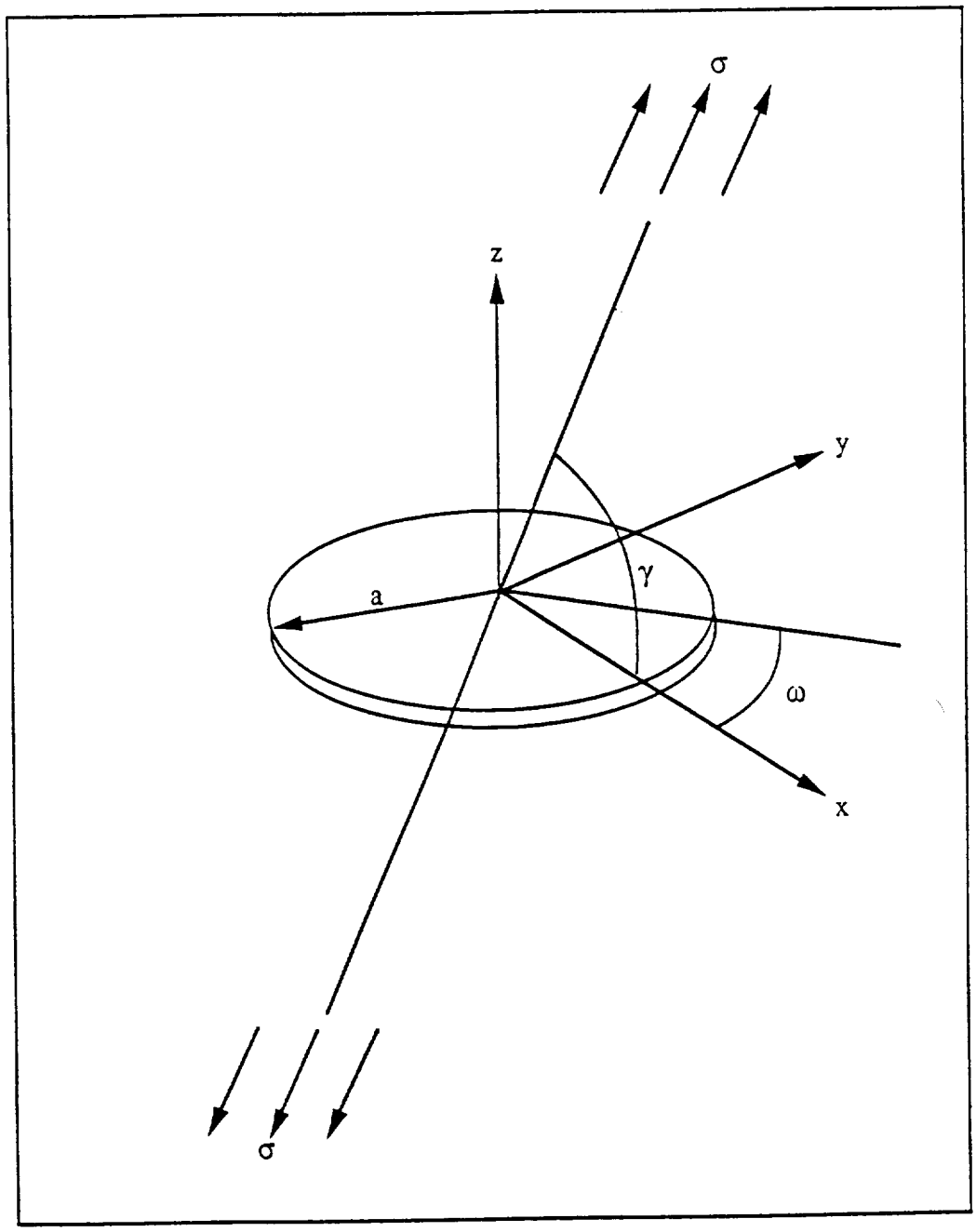

Figure 4.19 Circular Crack Buried in Infinite Body Inclined at an Angle γ With Respect to the Direction of Applied Load

are [33]

$$K_I = \left[\frac{2}{\pi}\sigma\sin^2\sqrt{\pi a}\right]$$

$$K_{II} = \left[\frac{4}{\pi(2-\nu)}(\sigma\sin\gamma\cos\gamma)\sqrt{\pi a}\right]\cos\omega$$

$$K_{III} = \left[\frac{4(1-\nu)}{\pi(2-\nu)}(\sigma\sin\gamma\cos\gamma)\sqrt{\pi a}\right]\sin\omega \qquad (4.5)$$

where σ is the applied stress, a the crack radius, γ the angle between the direction of applied load and the normal of the crack plane, and ω is the angle as is shown in Figure 4.19. Only a double region mesh can model this problem appropriately since symmetry no longer exists. The mesh is composed of two parallelepiped shaped subregions as shown in Figure 4.20. Each subregion is made up of 52 quadratic elements and 150 nodes including 88 nodes belonging to the interface. Quarter point elements and traction singular elements are used along the crack front as described in the previous section. The results are shown in Figures 4.21 to 4.23 in which the stress intensity factors are normalized. The calculated K_I are almost constant along the crack front. The error ranges from 1.17% to 1.19%. The maximum error for K_{II} and K_{III} are 2.34% and 5.71%, respectively. The total CPU time is 131 seconds.

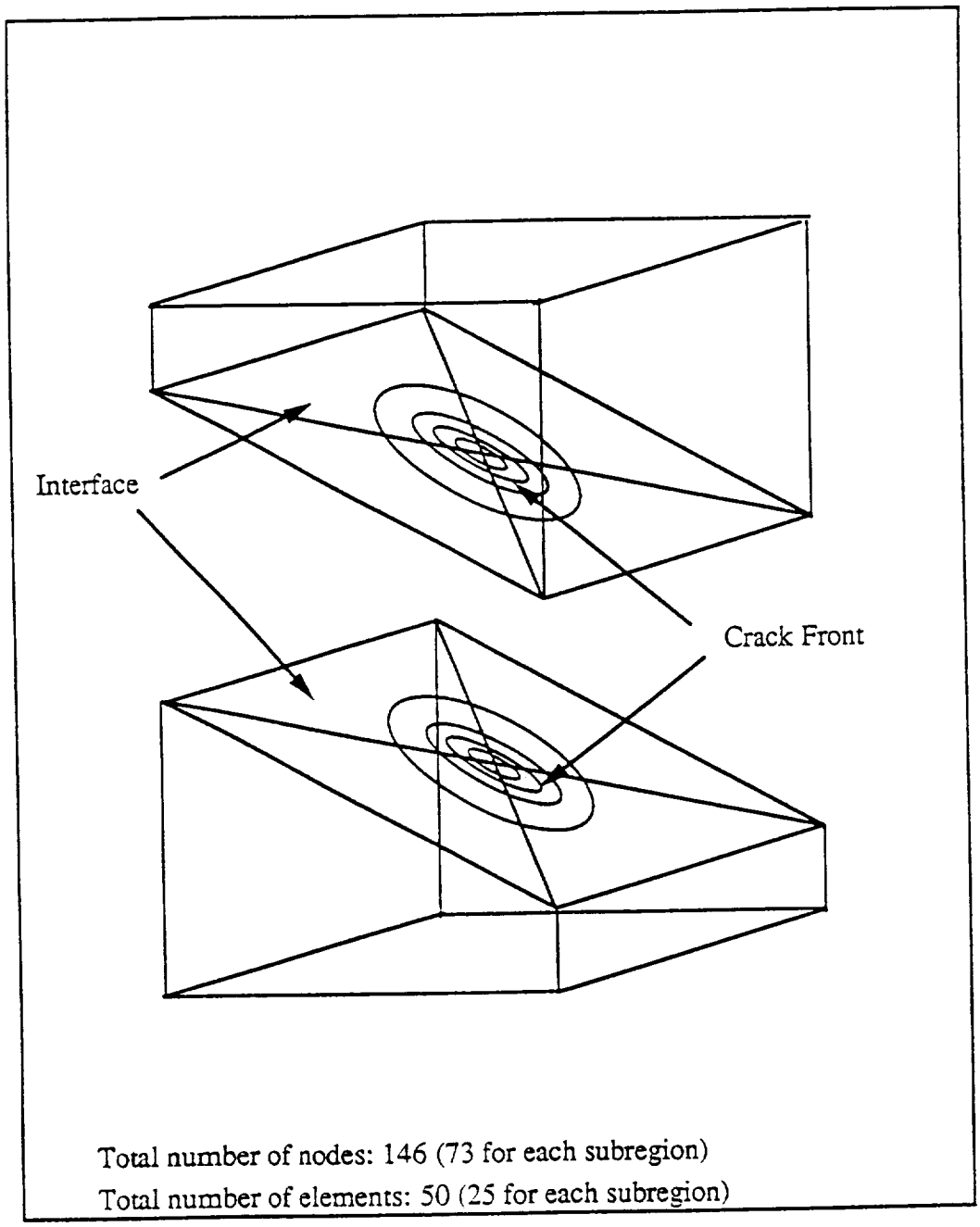

Figure 4.20 Element Mesh of Double Region Model for Buried Circular Crack Inclined at 30 Degrees

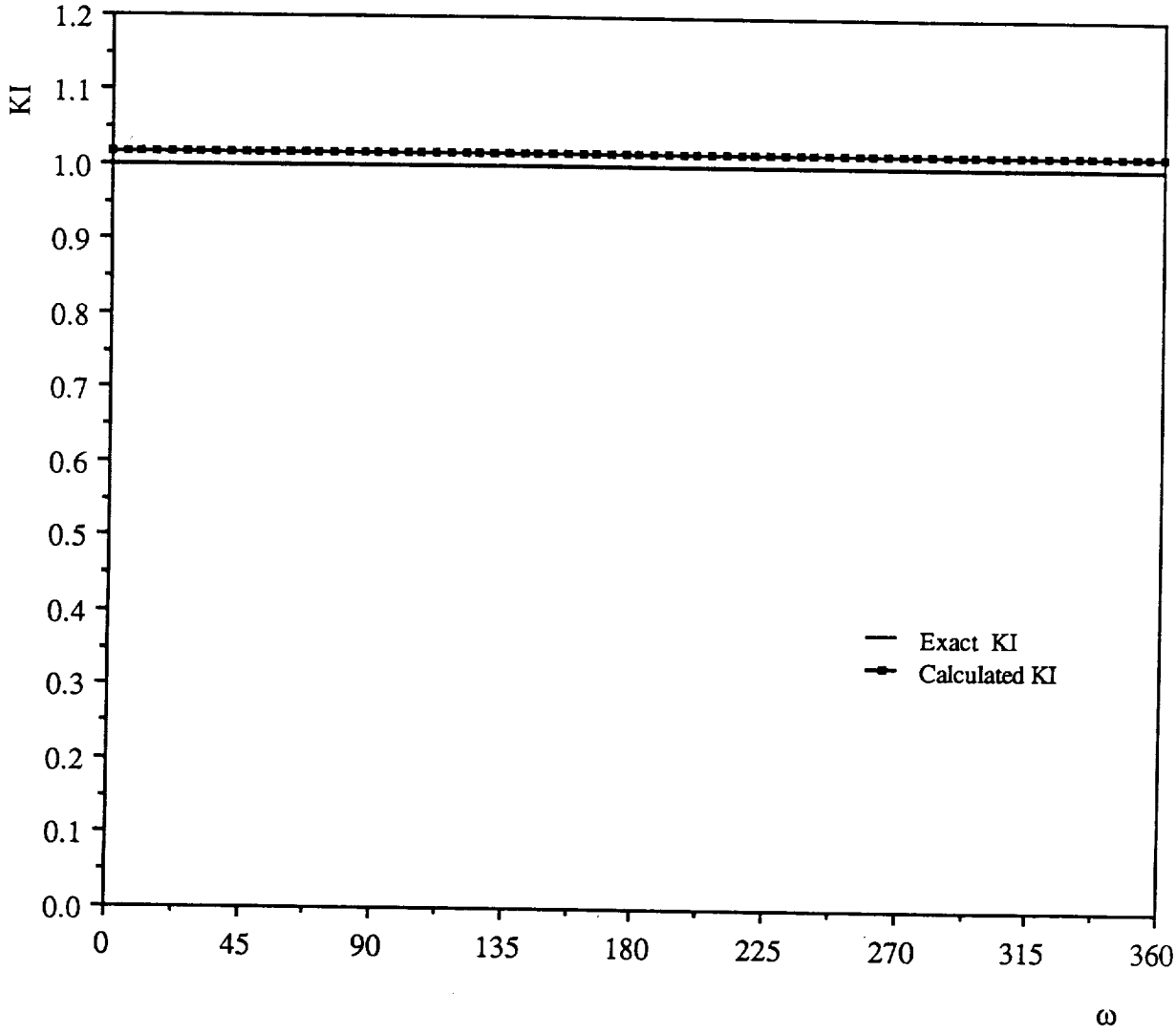

Figure 4.21 Comparison of Calculated KI with Exact Solution for Circular Crack Inclined at 30 Degrees

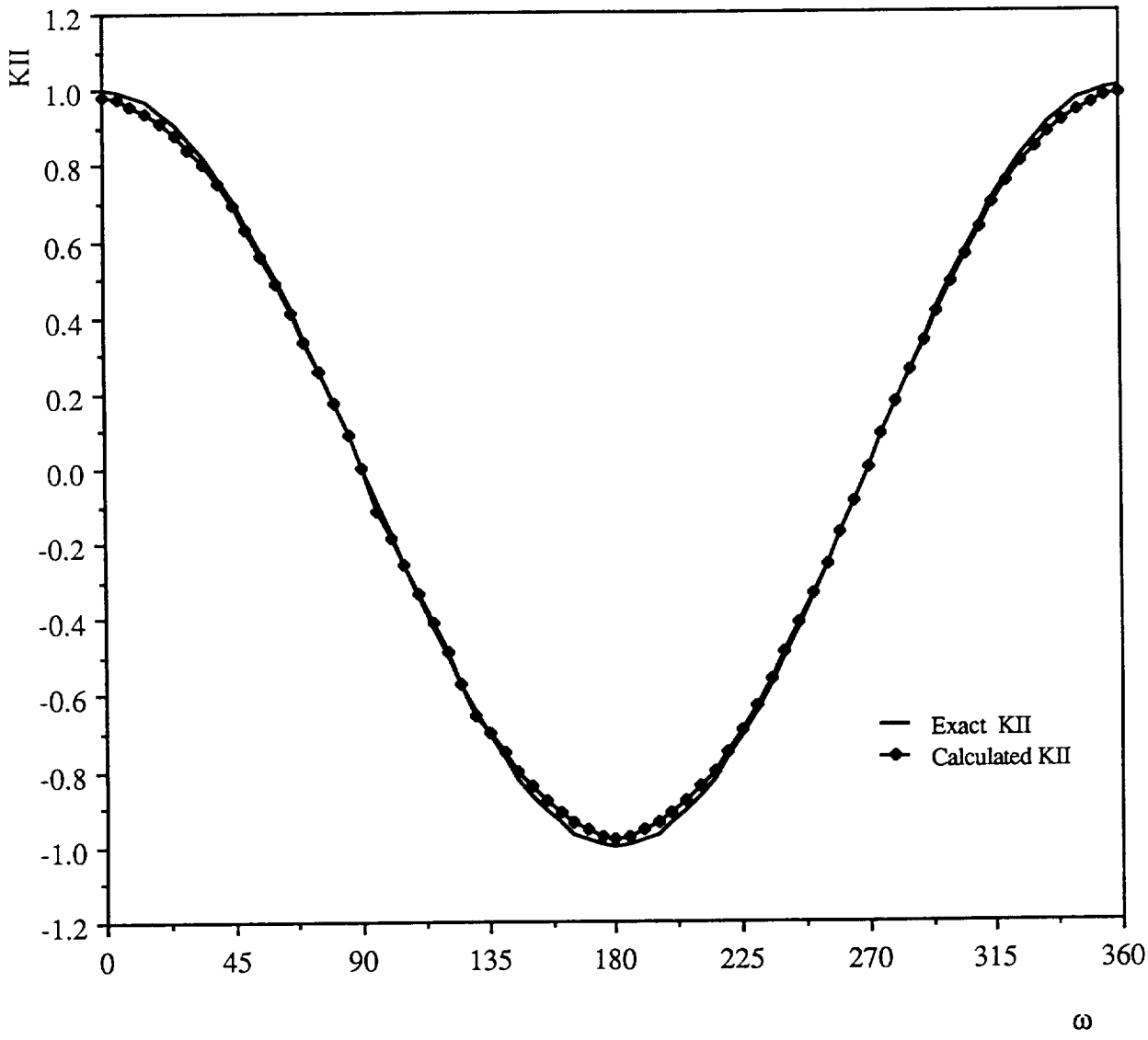

Figure 4.22 Comparison of Calculated KII with Exact Solution for Circular Crack Inclined at 30 Degrees

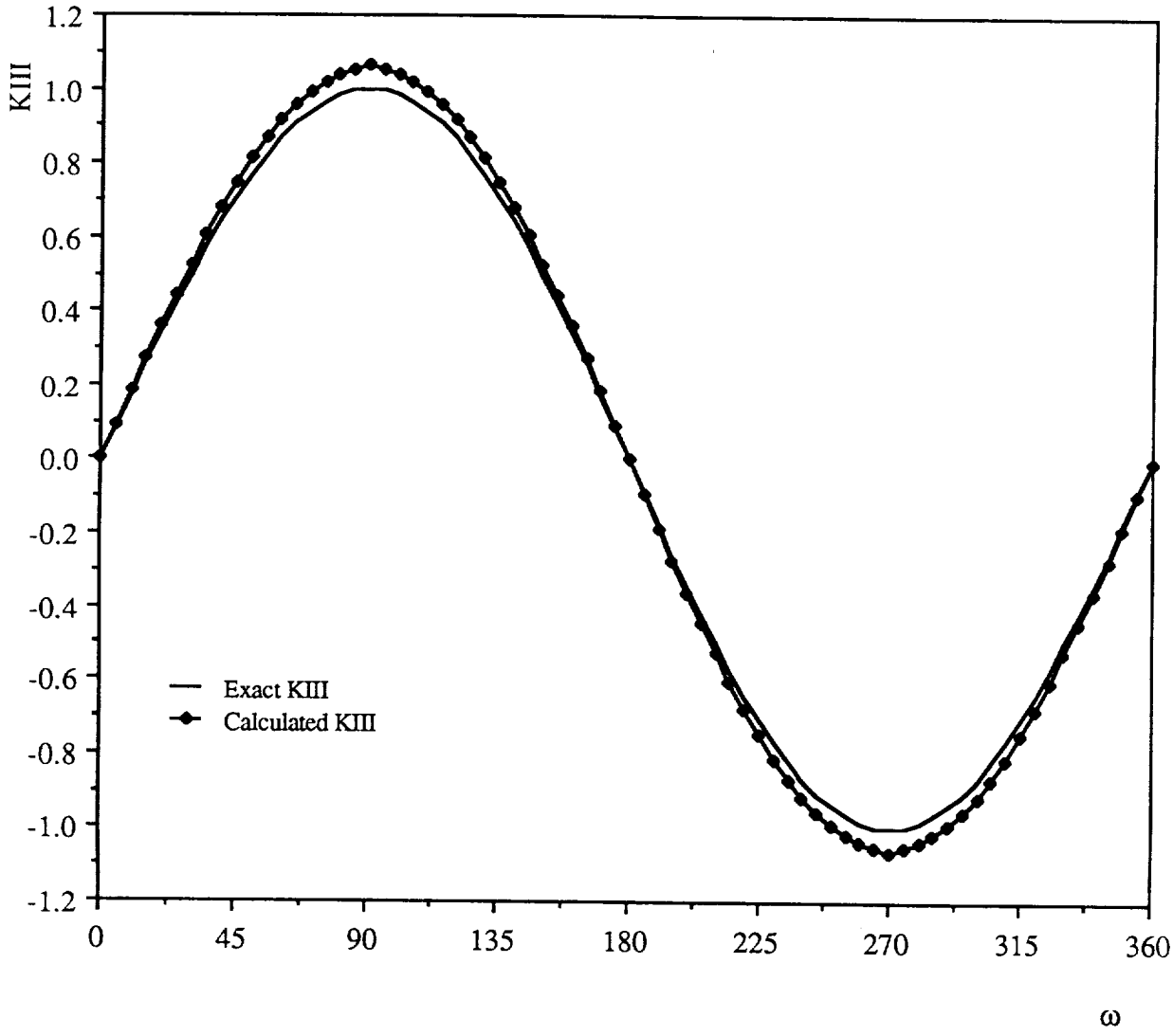

Figure 4.23 Comparison of Calculated KIII with Exact Solution for Circular Crack Inclined at 30 Degrees

4.5 Semi-circular Surface Crack Under Uniform Traction

The purpose of this section is to check the accuracy of the method for surface crack problems. Since an exact solution for this problem does not exist, the results are compared with the work of Tada [33], and Newman and Raju [34]. Tada presents the stress intensity factor K_I for a semi-circular surface crack in a semi-infinite body as shown in Figure 4.24 as

$$K_I(\theta) = \frac{2}{\pi}\sigma\sqrt{\pi a}\ F(\theta) \tag{4.6}$$

where

$$F(\theta) = 1.211 - 0.186\sqrt{\sin\theta} \qquad (10^\circ < \theta < 170^\circ)$$

and σ is the applied stress, a the crack radius, and θ is the angle measured from the surface as shown in Figure 4.24. Note that the K_I is not constant along the crack front. For the same problemNewman and Raju predict

$$K_I = \sigma\sqrt{\pi a}\left(\frac{1}{\sqrt{Q}}\right) F(\theta) \tag{4.7}$$

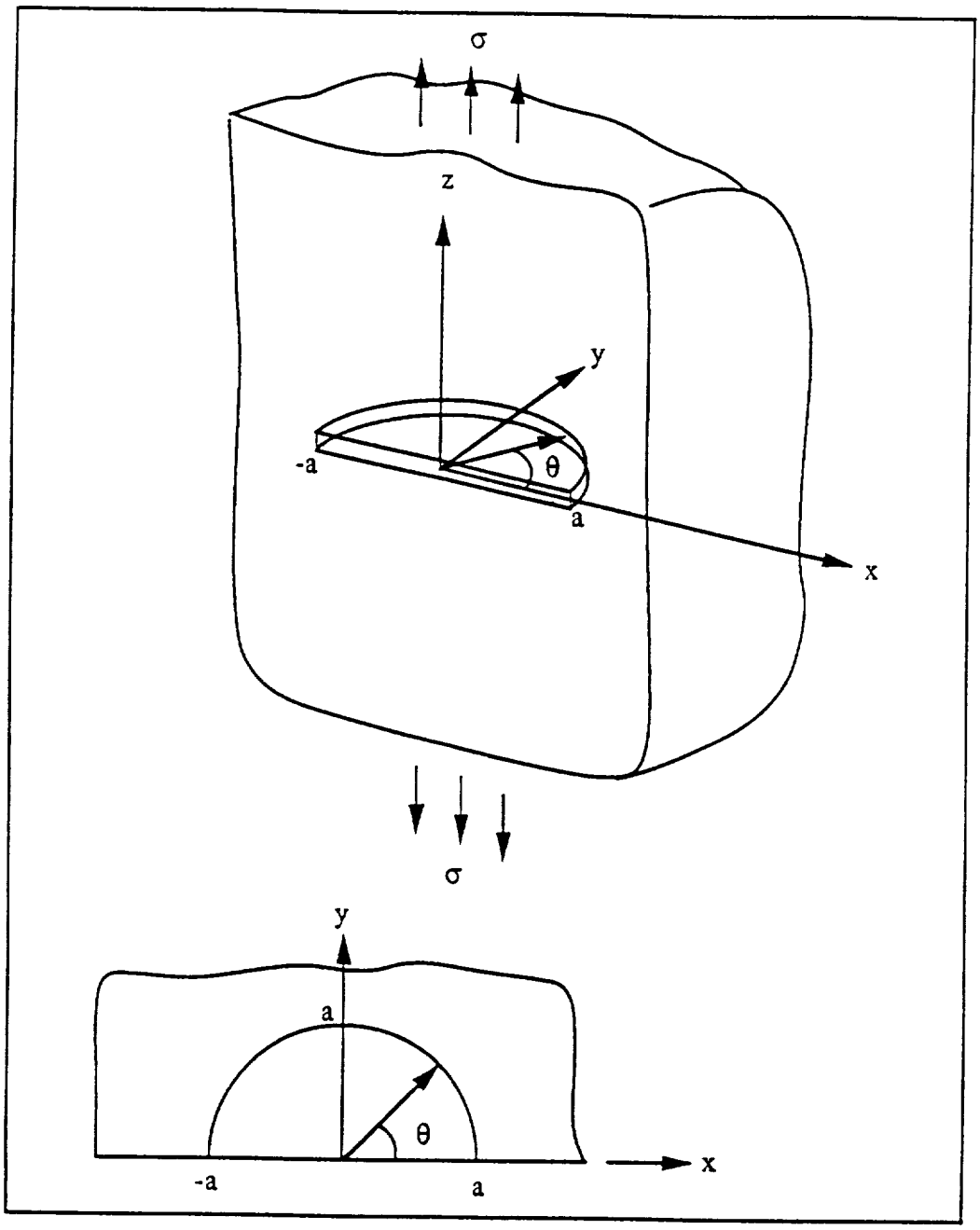

Figure 4.24 Circular Crack in Semi-infinite Body Under Uniform Tension

where

$$F(\theta) = 1.04 \left[1 + 0.1 \, (1-\sin\theta)^2 \right]$$

and Q = 2.464 for a semi-circular surface crack. A double region model, as shown in Figure 4.25, is used in the problem. Each subregion consists of 72 quadratic elements and 202 nodes.

The comparison of the results with the work of Tada and Raju and Newman is shown in Figure 4.26. The present results are quite consistent with these two predictions when the θ is between 35° and 90°. The maximum difference appears at the surface with the error of about 5.7%. This is because the K_I is calculated assuming of plane strain conditions and an inverse square root singularity of stresses. At the points where the crack intersects the free surface these conditions do not apply.

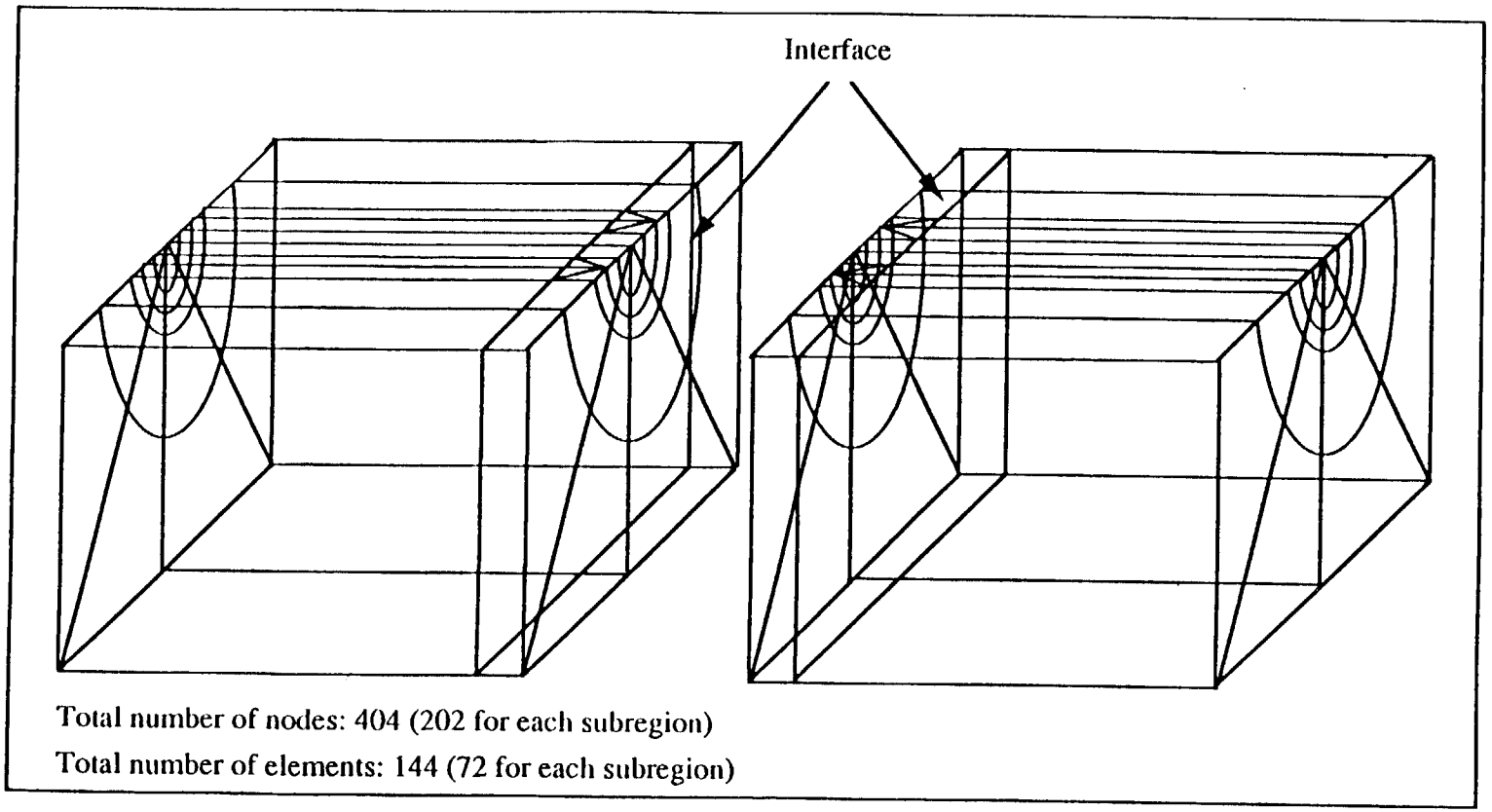

Figure 4.25 Element Mesh for Double Region Model of Surface Crack

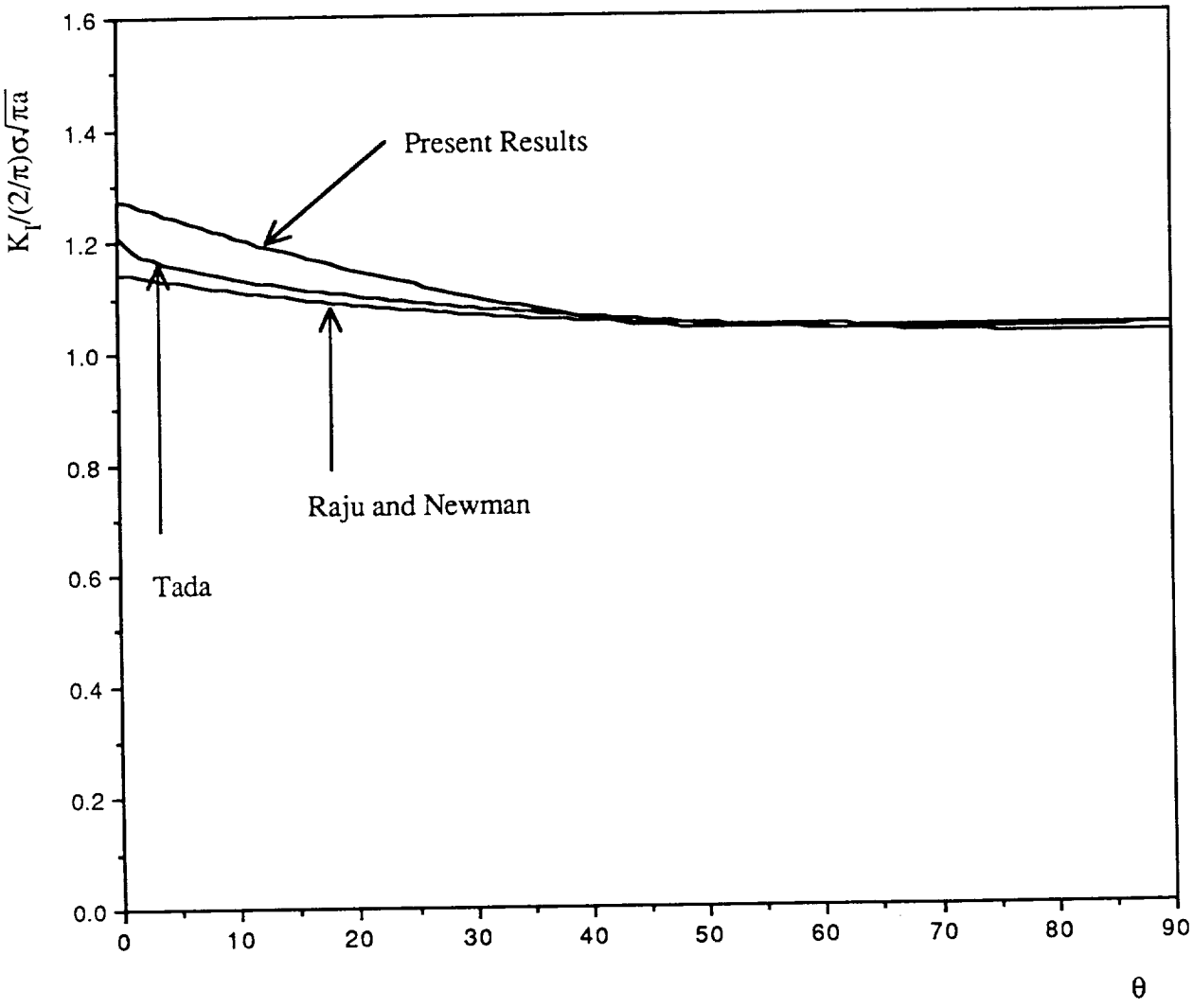

Figure 4.26 Comparison of Stress Intensity Factors for a Circular Surface Crack in a Semi-infinite Body Under Uniform Tension

CHAPTER FIVE

STRESS INTENSITY FACTOR ANALYSIS OF THE INNER RACEWAY OF HIGH SPEED BEARINGS

In this chapter, the geometry of the engine bearing is described and the loadings on the inner raceway (including the hoop stresses and the Hertzian contact load) are calculated. The stress intensity factors for several semi-circular surface cracks of different lengths and inclinations are presented as functions of the location of the indenters.

5.1 Geometry and Applied Loading

The bearing analyzed in this report is a high performance engine bearing which is used on the main shaft of an aircraft. The dimensions and the geometry of the bearing are shown in Table 5.1 and Fig.5.1, respectively.

The bearing consists of 28 ball rollers. To simulate the passage of each ball only 1/28th of the inner raceway is modeled. Since the radius of the inner raceway is large compared to the other dimensions of the part, the curvature is neglected and the mesh is modeled as a block with flat surface as shown in Fig.5.2.

The external loadings considered in the analysis are the hoop stresses and the Hertzian load. The hoop stresses due to the rotation and the shrink fit are taken from [22] and are given by

Shaft	Inner radius a_s = 2.0 inch
	Outer radius b_s = 2.30233 inch
Inner raceway	Inner radius a_i = 2.3 inch
	Outer radius b_i = 2.6 inch
Outer raceway	Inner radius a_o = 3.1 inch
	Outer radius b_o = 3.35 inch
Bearing length L	0.57322 inch
Ball bearing	Radius R = 0.25 inch
No. of ball bearings	28
Shaft speed	25,500 rpm
M50 steel material properities	$E = 3.0X\ 10^7$ psi
	$\rho = 0.288$ lb/in^3
	$\nu = 0.3$
	K_{IC} = 18 ksi$\sqrt{in}$

Table 5.1 Dimensions and Material Properities of Typical Ball Bearing for Aircraft Engines

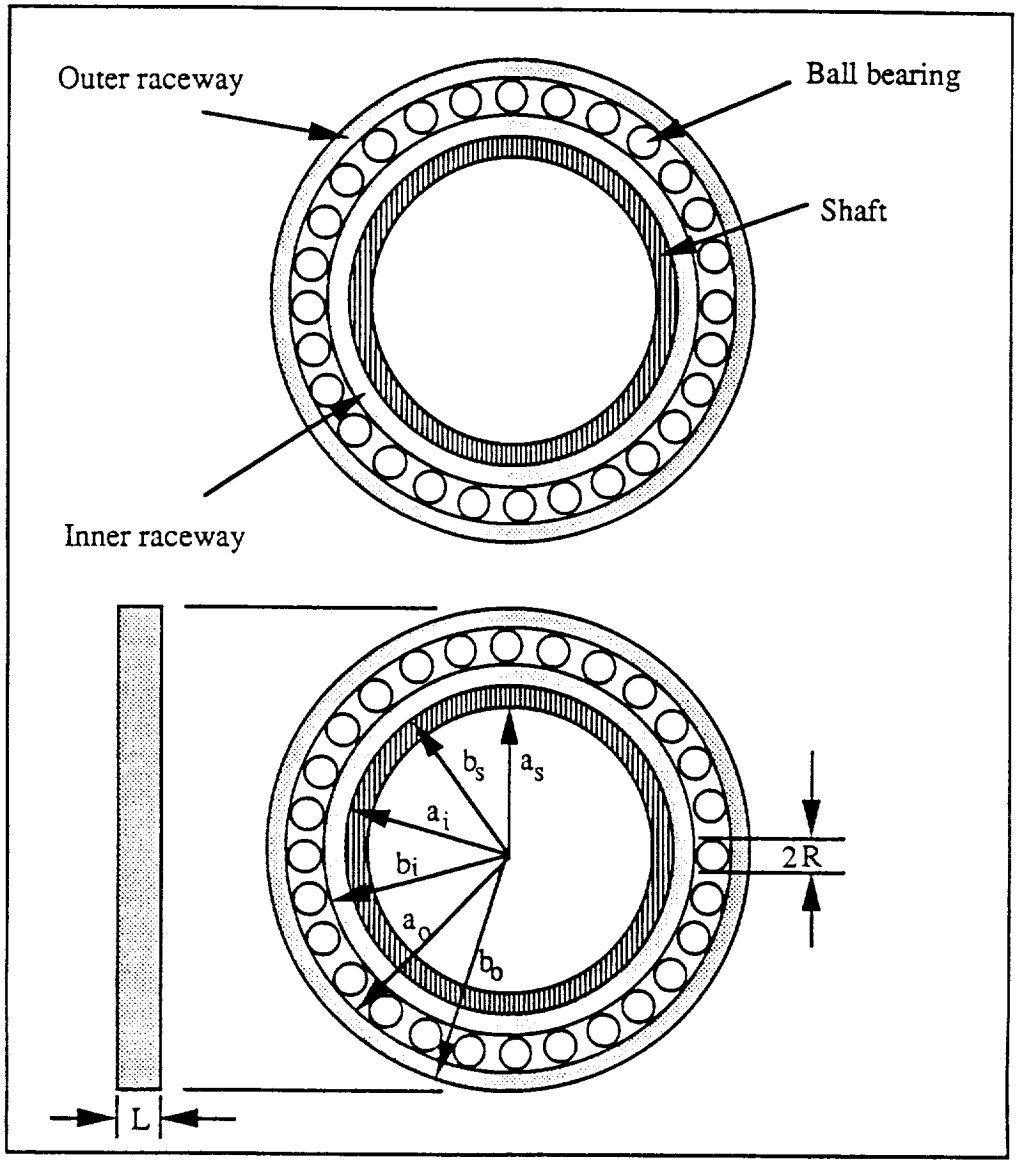

Figure 5.1 Geometry of Bearing

$$\sigma_{\theta\theta} = \frac{3+\nu}{8}\rho\omega^2[\, b_i^2 + a_i^2 + \frac{a_i^2 b_i^2}{r^2} - \frac{1+3\nu}{3+\nu} r^2] + P\frac{(b_i/r)^2 + 1}{(b_i/a_i)^2 - 1} \qquad (5.1)$$

where ω is the angular velocity of the shaft and P is the pressure existing between the shaft and the inner raceway which is equal to

$$P = \frac{E\delta_n}{a_i}\frac{(a_i^2 - a_s^2)(b_i^2 - a_i^2)}{2a_i^2(b_i^2 - a_s^2)} \qquad (5.2)$$

where δ_n is the difference between the outer radius of the shaft and the inner radius of the inner raceway during rotation at speed ω. It can be obtained by

$$\delta_n = \delta - \Delta\delta \qquad (5.3)$$

where δ is the original shrink fit at 0 rpm which is equal to 0.00233 inch in this case and $\Delta\delta$ is the difference in the radial displacement between the inner radius of the inner raceway, u_r^i, and the outer radius of the shaft, u_r^s, under the rotation at speed ω, i.e.,

$$\Delta\delta = u_r^i - u_r^s$$

$$= \frac{\rho\omega^2 a_i}{4E}[\,(3+\nu)b_i^2 + (1-\nu)a_i^2\,] - \frac{\rho\omega^2 b_s}{4E}[\,(3+\nu)b_s^2 + (1-\nu)a_s^2] \qquad (5.4)$$

Applying the data of Table 5.1 to the above equations results in

$$\sigma_{\theta\theta} = 1973.61[\,3.5986 + \frac{24.3286}{r^2}\,]$$

$$+ \omega^2 \times 10^{-5}\,[\,3.6290 - 0.1941(r^2) + \frac{9.1248}{r^2}\,] \quad \text{(psi)} \qquad (5.5)$$

where ω is in rpm. The maximum hoop stress of the inner raceway is at the inner radius. The hoop stresses range from 38 ksi to 44 ksi when the rotation speed is 25,500 rpm.

The contact region between a sphere and a flat surface is circular and the stress distribution is [30]

$$p = p_o\sqrt{1 - \frac{x^2}{a^2} - \frac{y^2}{a^2}} \qquad (5.6)$$

where a is the radius of the contact area and p_o is the maximum stress which can be

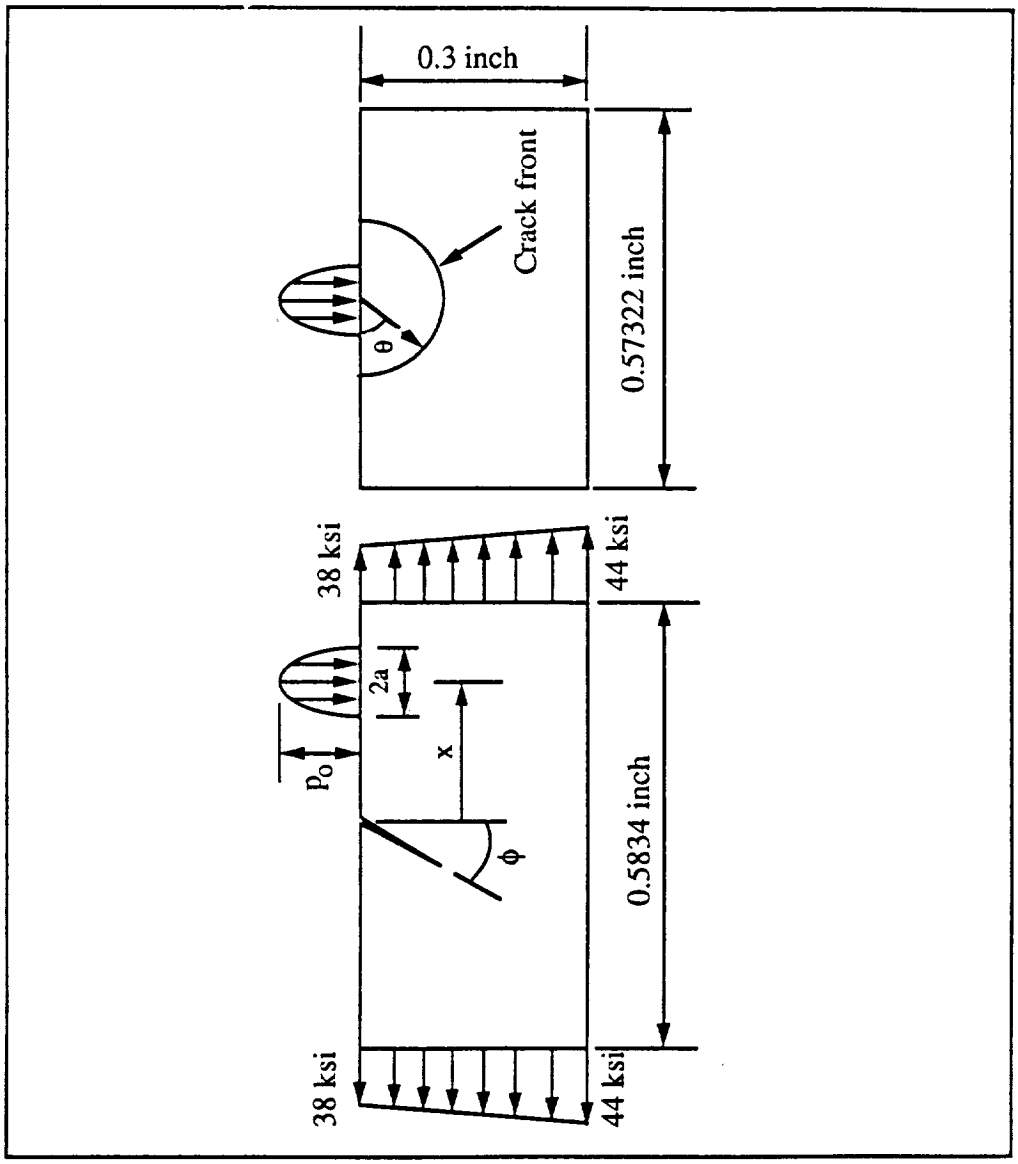

Figure 5.2 Model of Bearing

calculated from

$$p_o = \frac{3}{2}\frac{P_T}{\pi a^2} \tag{5.7}$$

where P_T is the total load. The radius is

$$a = \sqrt[3]{\frac{3P_T R\,(1 - \nu^2)}{2E}} \tag{5.8}$$

where R is the radius of the sphere. As discussed in [6] the experimental data indicates that for the bearing considered in the present analysis the maximum Hertzian stress is 285 ksi. Subsequent calculations will be based on this value.

The distribution of the Hertzian contact loading is distorted when the spherical body is rolling over a surface containing a surface breaking crack [31]. However, the influence of the subsurface crack on the Hertzian stress distribution has been shown [31] to be insignificant. The interaction effects of the subsurface crack on the Hertzian distribution are thus ignored.

Since the Hertzian stress fields can be solved in closed form, superposition is applied in order to decrease the number of nodes needed to model the Hertzian

contact load accurately. The superposition method is illustrated in Fig.5.3. The stress intensity factors of a surface crack subjected to the Hertzian load are equal to the stress intensity factors of the same crack loaded with the negative of the stresses produced by the Hertzian loading. The stresses produced in the interior of the plate by the hertzian contact loading are calculated by integrating the stresses due to a concentrated force acting on the boundary of a semi-infinite solid [22] as shown in Fig.5.4. The hoop stresses are directly applied on the the end of the plate. The total stress intensity factor is then the superposition of the stress intensity factor due to the hoop stresses and the one resulting from the Hertzian load. It should be noted that the depth of the plate is assumed to be large enough so that the distribution of loading remains Hertzian.

5.2 Stress Intensity Factor of Circular Subsurface Crack in the Inner Raceway of the Engine Bearing

This section presents the results of a quasi-static stress intensity factor analysis of a typical ball bearing which is used as a support for the main shaft of aircraft engines. All the calculations are based on the model shown in Fig.5.2 which consists of an axial hoop stress and a Hertzian load (contact radius a and maximum intensity p_0) interacting with a semi-circular crack (radius, or length l) inclined at an angle ϕ. The dynamic effect is ignored and the distance x, between the center of the Hertzian distribution and the crack mouth is changed incrementally to simulate the passage of each ball bearing.

The stress intensity factors for this problem vary with position along the

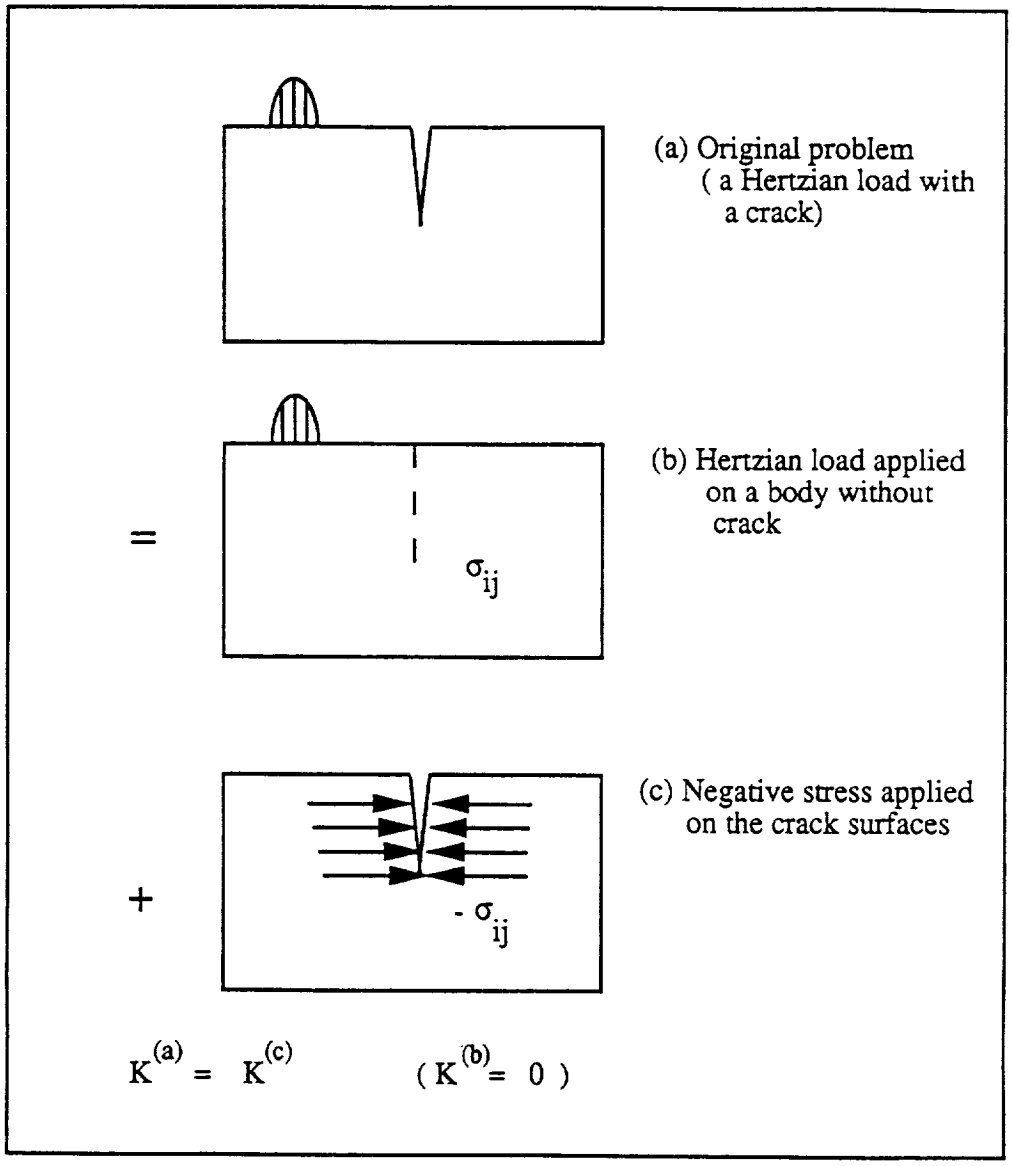

Figure 5.3 Illustration of Superposition Method

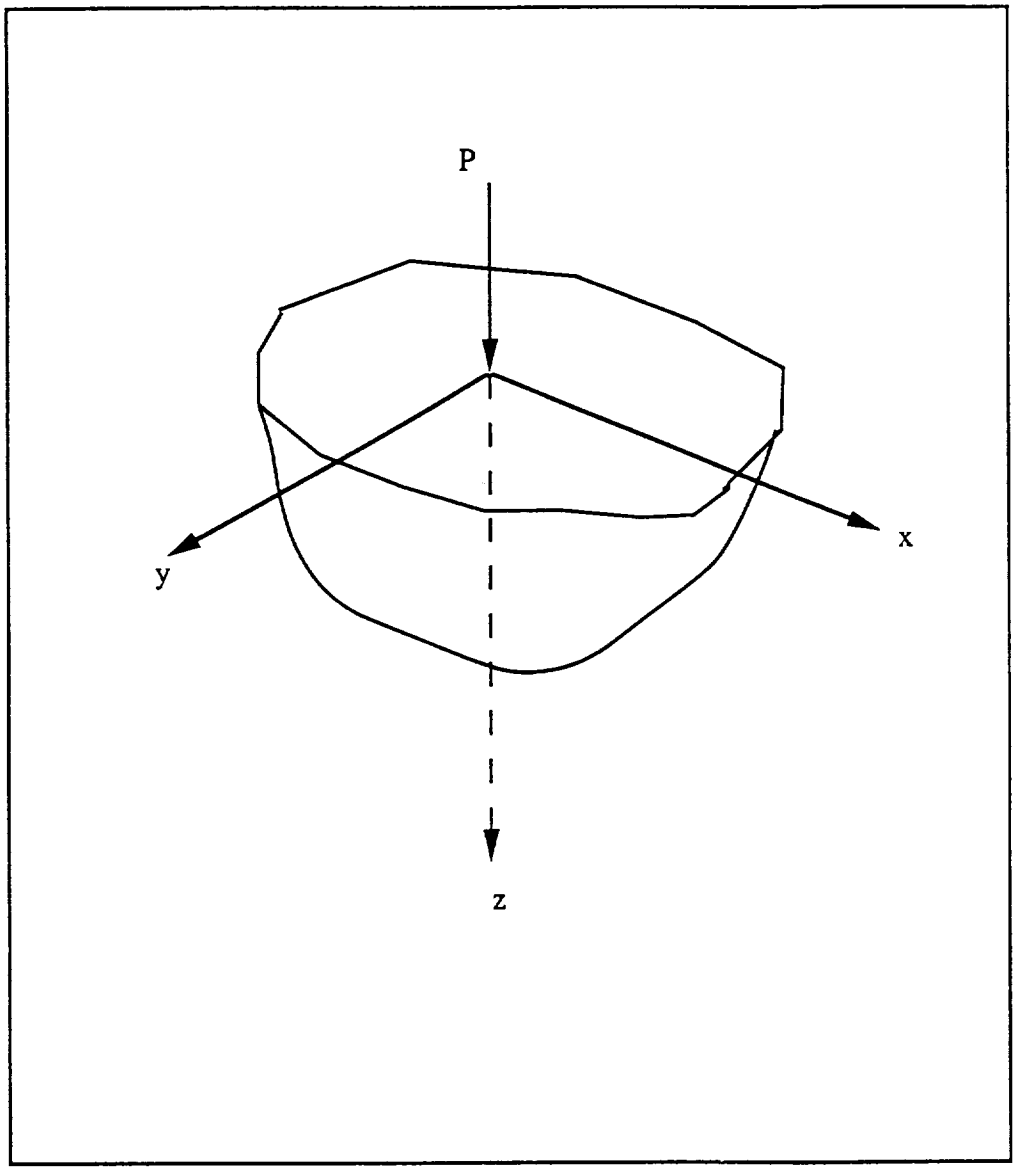

Figure 5.4 Concentrated Force acting on the Boundary of a Semi-infinite Body

crack front (θ). A typical variation of the mode I stress intensity factor at $\theta = 90°$ with roller position and crack length for a vertical crack ($\phi = 0°$) is shown in Fig.5.5 for p_o = 285 ksi (a = 0.00679 inch). When the roller is at a distance greater than four times the contact length from the crack mouth, the stress intensity factor is a constant which results from the axial stress. As the roller gets closer, the compressive stress arising from the Hertzian load decrease the K_I stress intensity factor. When the load is on the crack mouth the stress intensity factors becomes negative for the cracks which are shorter than 0.005 inch. The negative value of K_I indicates the closure of the crack. For longer cracks, the decrease of K_I diminishes since the crack tip is beyond the range of the highly compressive Hertzian stress field.

The variation of the mode II stress intensity factor for the same loading condition is shown in Fig.5.6. The value of K_{II} is zero when the roller is far from the crack mouth. As the roller approaches the crack, K_{II} starts to increase and reaches a maximum value when the load reaches the crack mouth. As the roller crosses to the other side of the crack, K_{II} abruptly changes sign and decreases to a minimum value equal in magnitude to the previous maximum. For small cracks this change is very abrupt, but for large cracks the change is more gradually. As pointed out in [6], these abrupt variations in K_I and K_{II} may significantly affect the propagation of short cracks.

The stress intensity factors for $\theta = 45°$ are shown in Fig.5.7 to 5.9. It is observed that the variations of K_I and K_{II} did not differ significantly from $\theta = 90°$. Another stress intensity factor K_{III} is observed based on the local coordinate system moving along the crack front. The K_{III} behaves as K_{II}. Fig.5.10 to 5.12

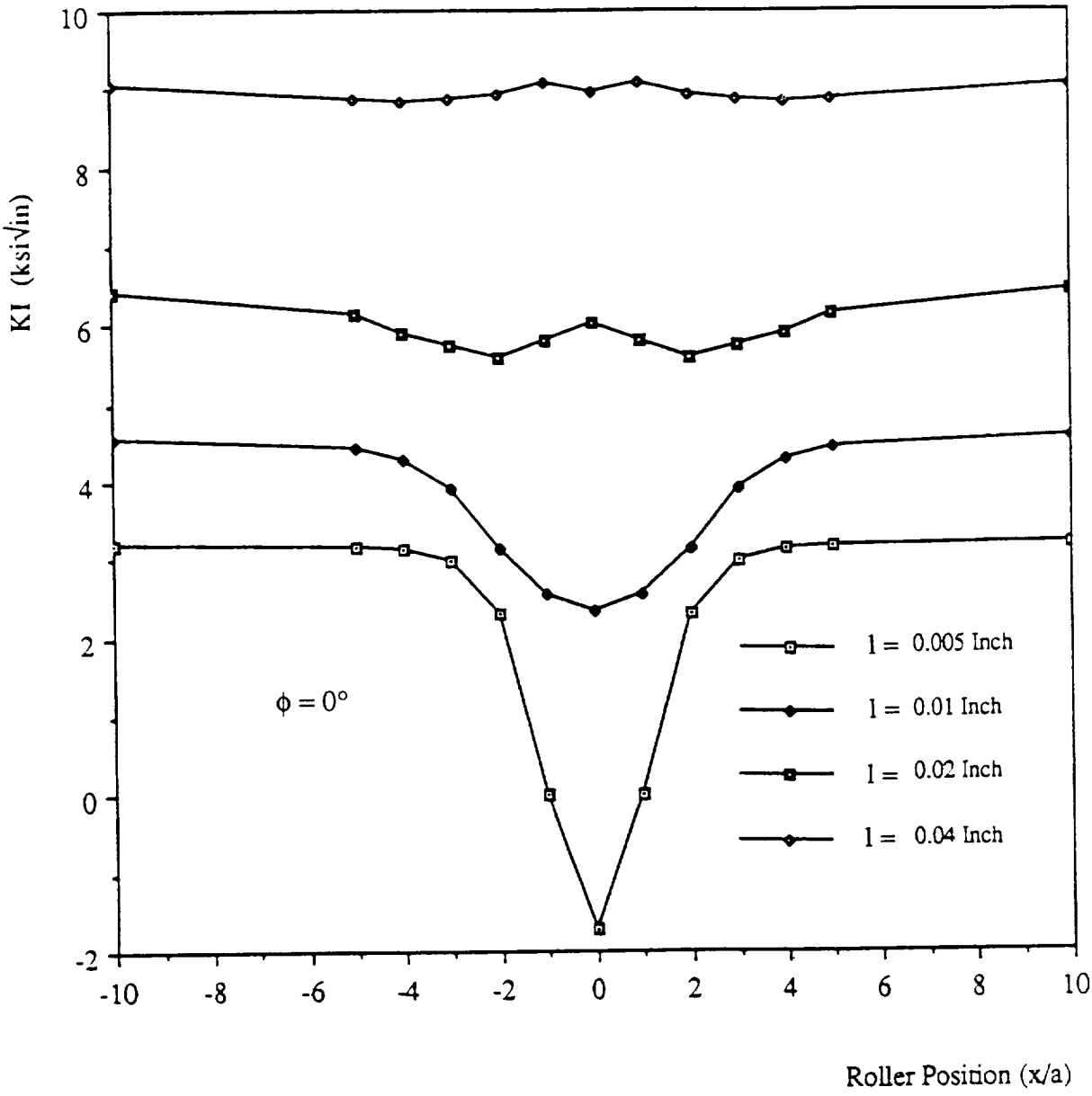

Figure 5.5 Variation of KI at $\theta = 90^{\circ}$ as a Function of Roller Position with Different Crack Length

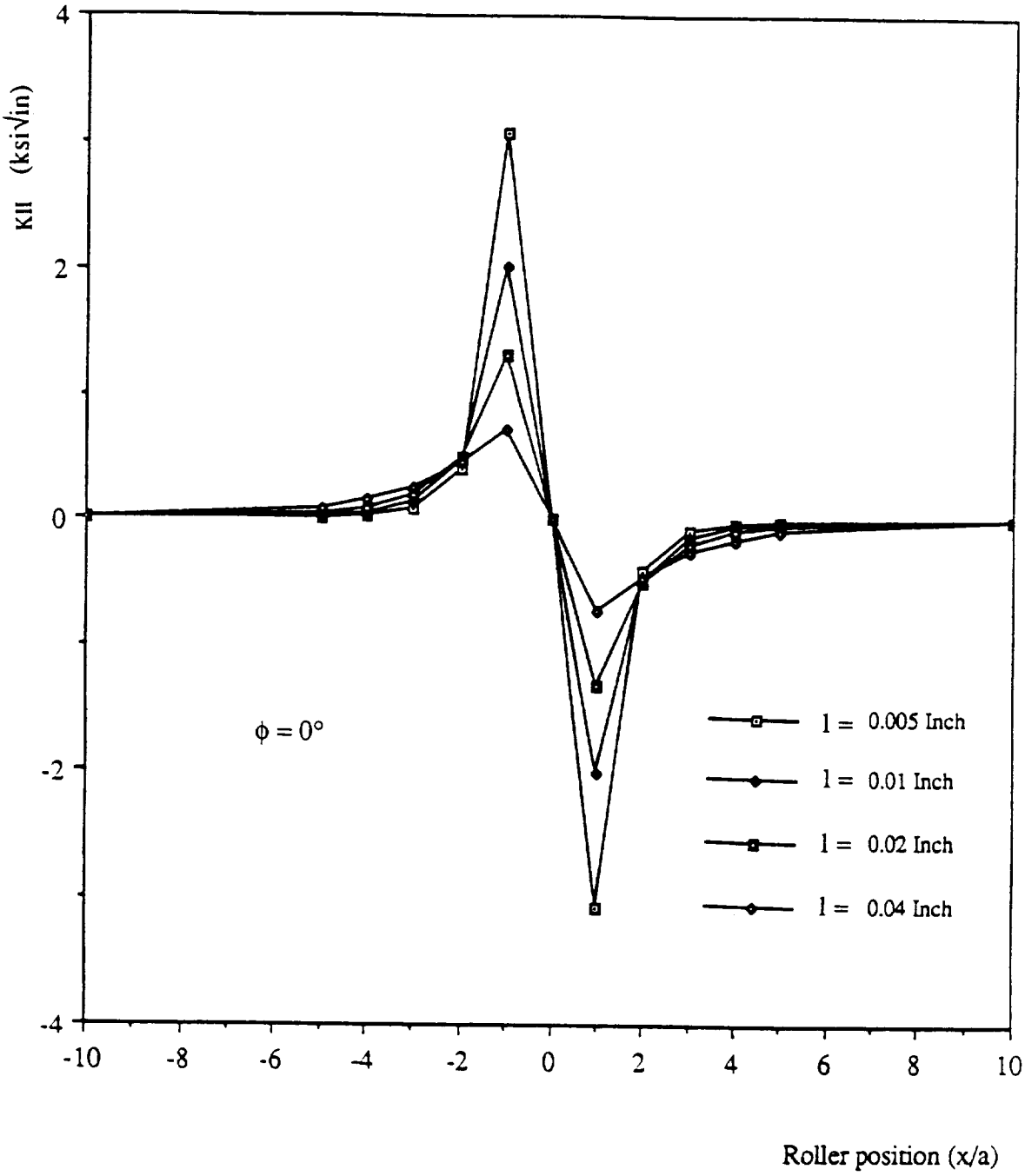

Figure 5.6 Variation of KII at $\theta = 90^{o}$ as a Function of Roller Position with Different Crack Length

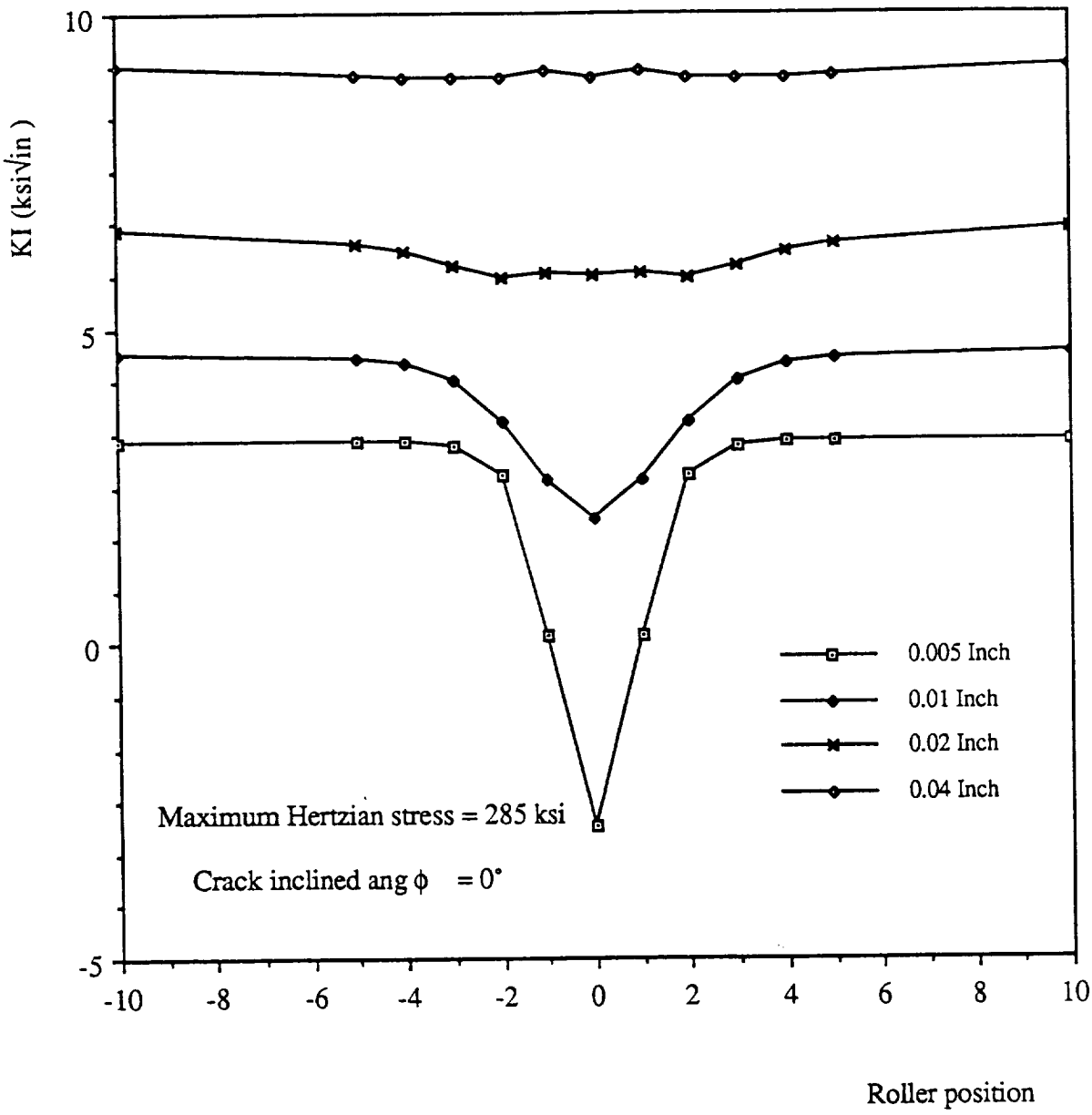

Figure 5.7 Variation of KII at θ =45° as a Function of Roller Position with Different Crack Length

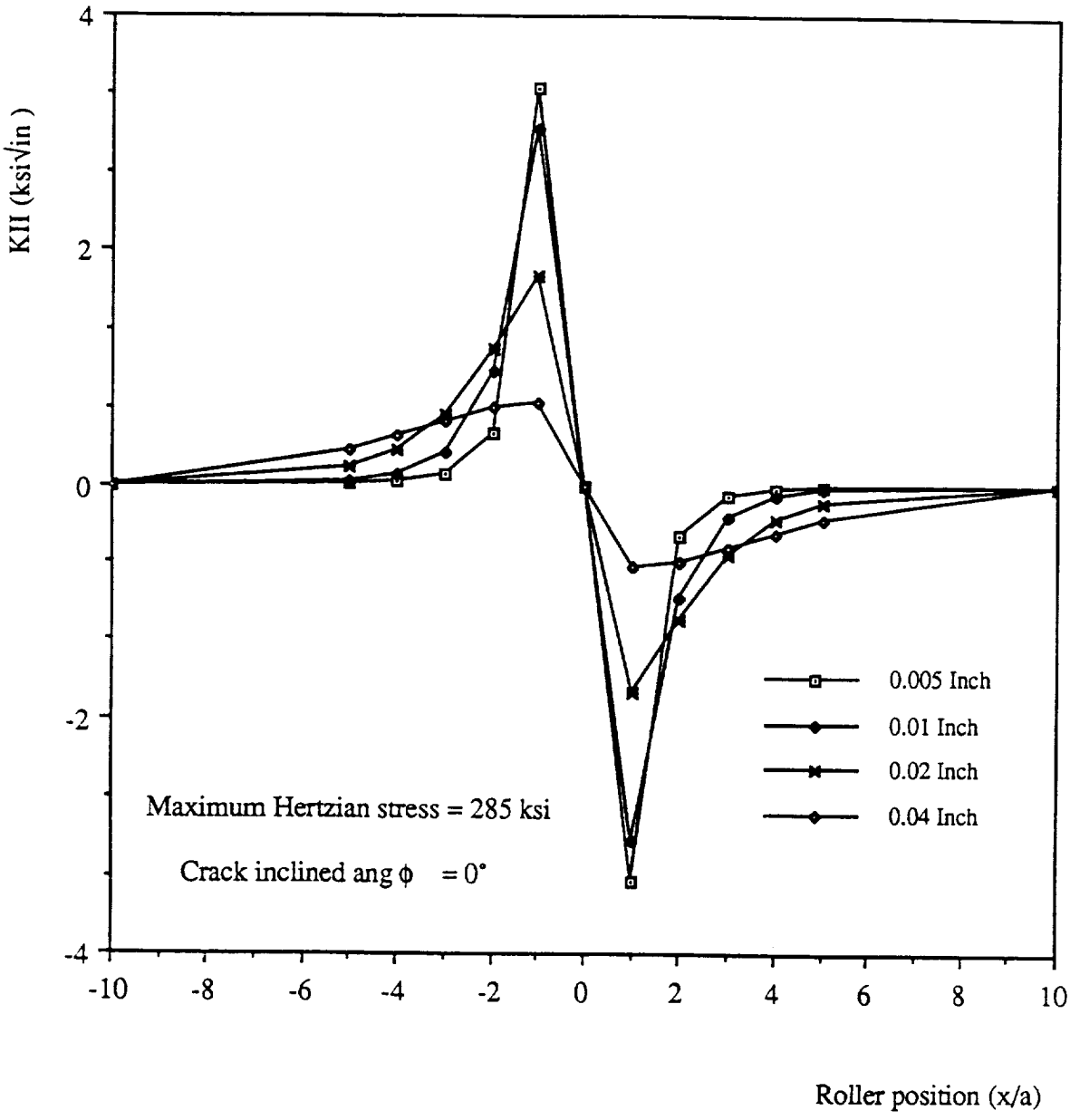

Figure 5.8 Variation of KII at θ =45° as a Function of Roller Position with Different Crack Length

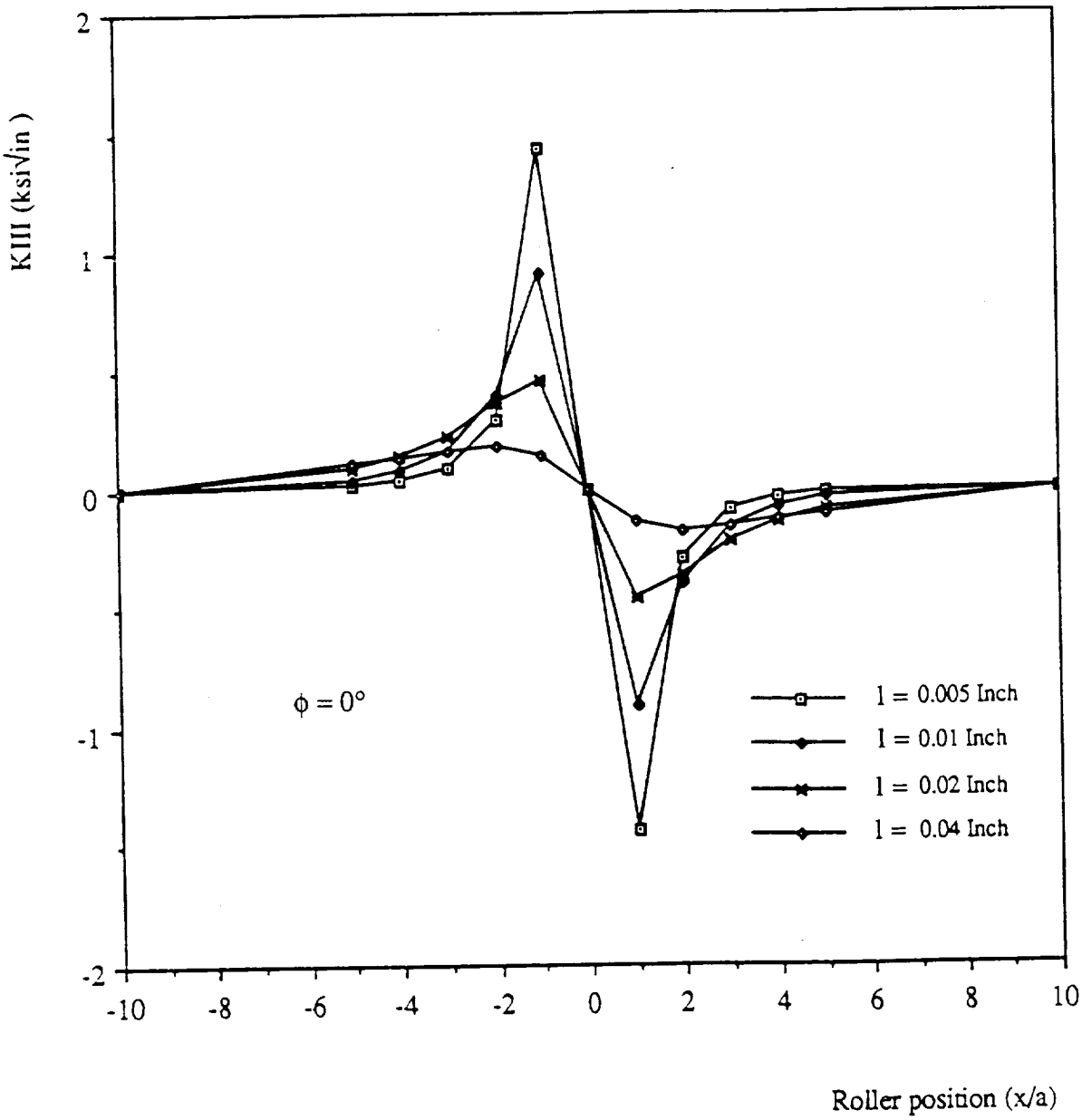

Figure 5.9 Variation of KIII at $\theta = 45^{o}$ as a Function of Roller Position with Different Crack Length

show the stress intensity factors for different locations along the crack front. It can be seen from Fig.5.10 that the magnitude of K_I does not change significantly. The magnitudes of K_{II} and K_{III} change along the crack front but however it can be calculated from Fig.5.11 and 5.12 that the square root of the sum of the squares of K_{II} and K_{III} are almost constant along the crack front. A comparison of the results for $\phi = 0°$ obtained in the presented analysis with those presented in Mendelson and Ghosn [6] revealed that the magnitudes and variations in K_I are similar. However, the mode II stress intensity factors differ significantly. As seen in Fig.5.5, for l = 0.02 inch the maximum value of K_{II} is approximately 1.5 ksi $\sqrt{in}$, while in reference [6] it is approximately 10 ksi$\sqrt{in}$.

Fig.5.13 and 5.14 present the stress intensity factors of K_I and K_{II} at $\theta=90°$, respectively, for cracks inclined at $\phi = 30°$ for $p_0 = 285$ ksi. An increase of K_I is observed when the roller passes to the right hand side of the crack mouth for short cracks. This is because the Hertzian load causes the inclined crack surfaces apart when it is passing over the crack mouth. The value of K_{II} before the roller crossing over the crack from the left is much greater than the K_{II} after the roller moving to the right of the crack mouth since the Hertzian load is pushing the left crack surface sliding along the right crack surface when the roller is on the right hand side of the crack.

Fig.5.15 and 5.16 show K_I and K_{II} variations for several inclinations of a crack length l = 0.02 inch. High values of K_{II} is observed for $\phi = 15°$ and $\phi = 30°$. The mode I fracture toughness of M50 steel, which is used for this type of bearing, is of the order of 18 ksi$\sqrt{in}$. Assuming the mode II toughness is of comparable magnitude, these results indicate that this applied loading would lead to large

propagation rates for cracks inclined at 30°.

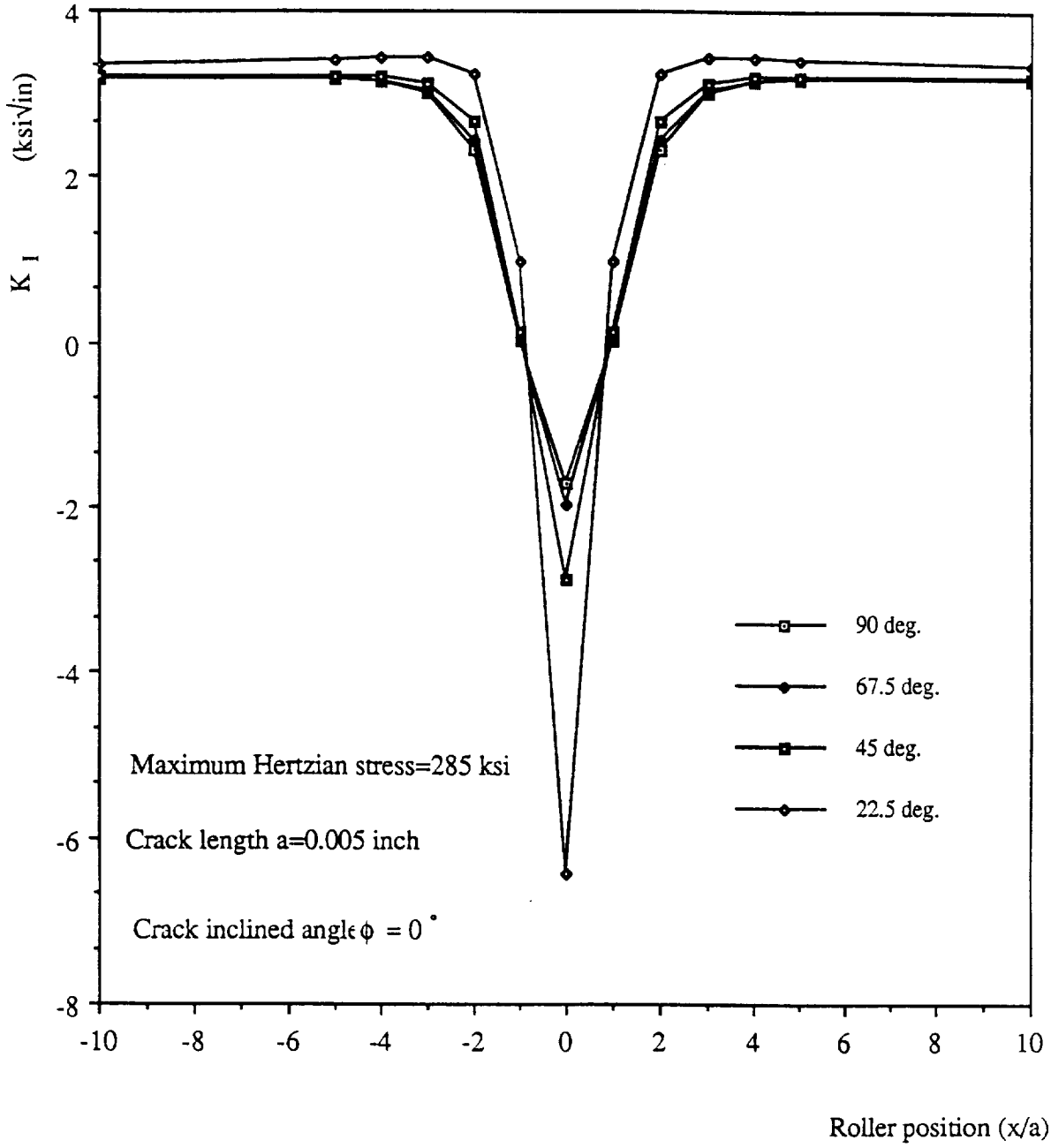

Figure 5.10 Variation of KI as a Function of Roller Position with Different Angle θ

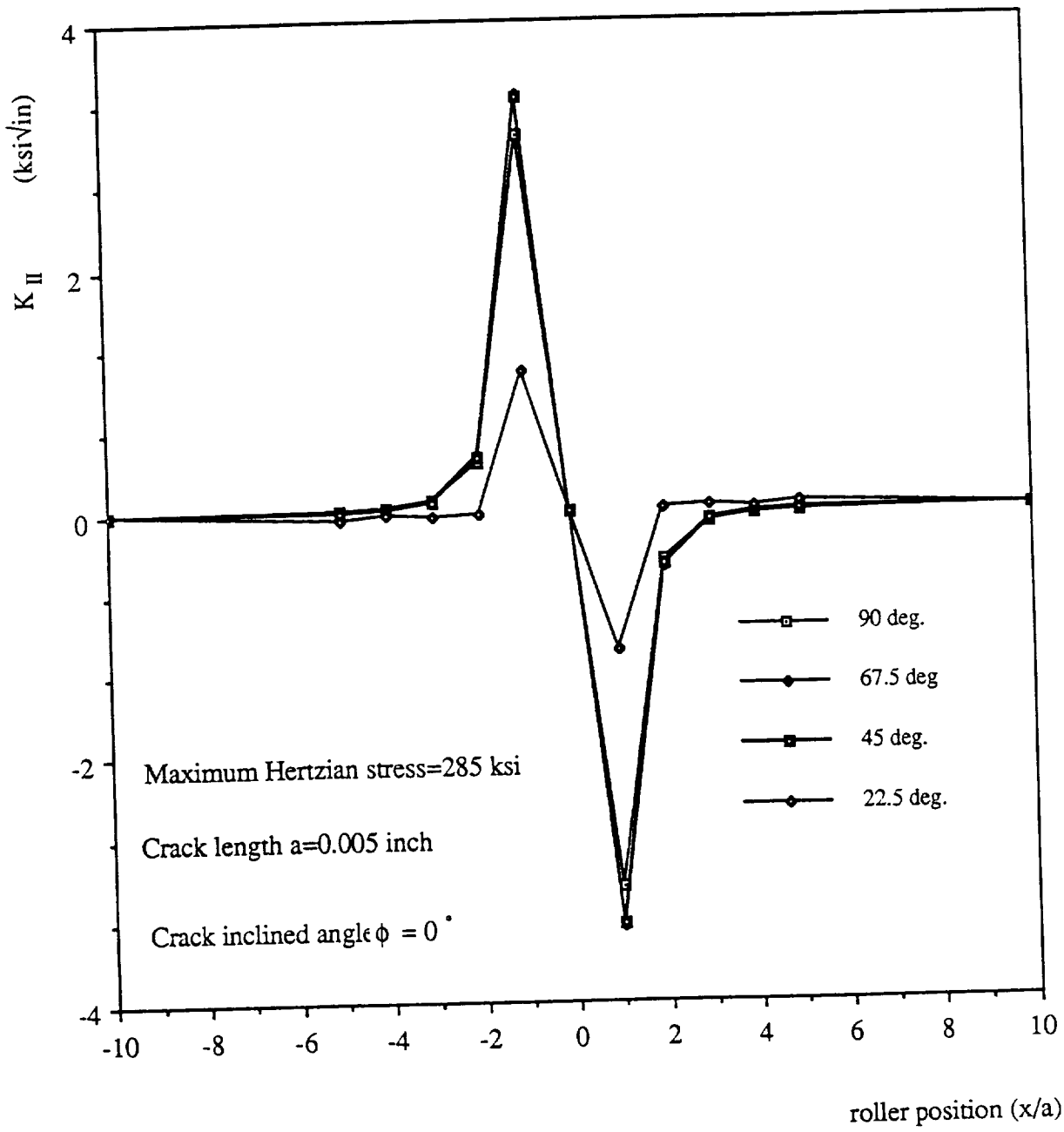

Figure 5.11 Variation of KII as a Function of Roller Position with Different Angle θ

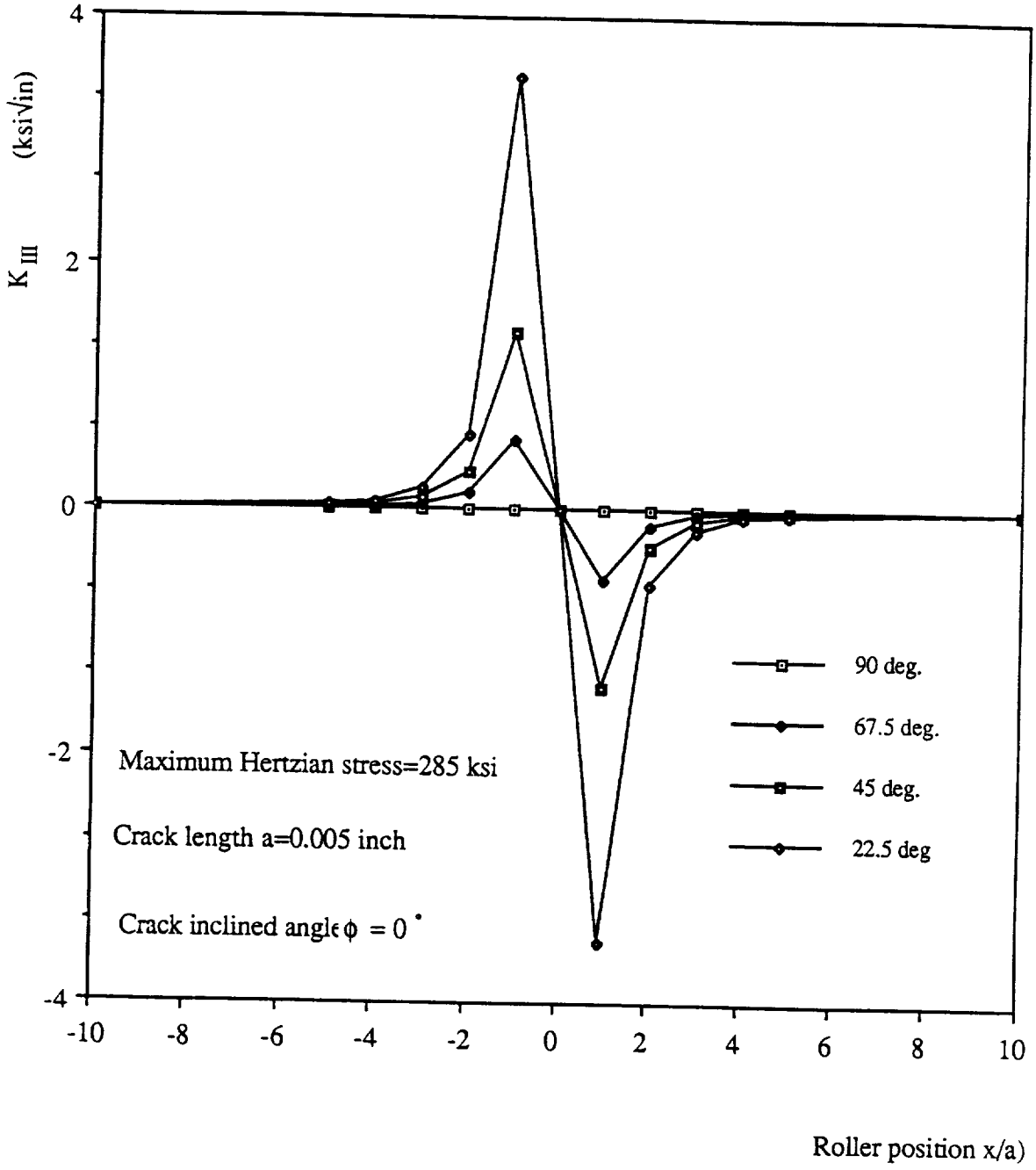

Figure 5.12 Variation of KIII as a Function of Roller Position with Different Angle θ

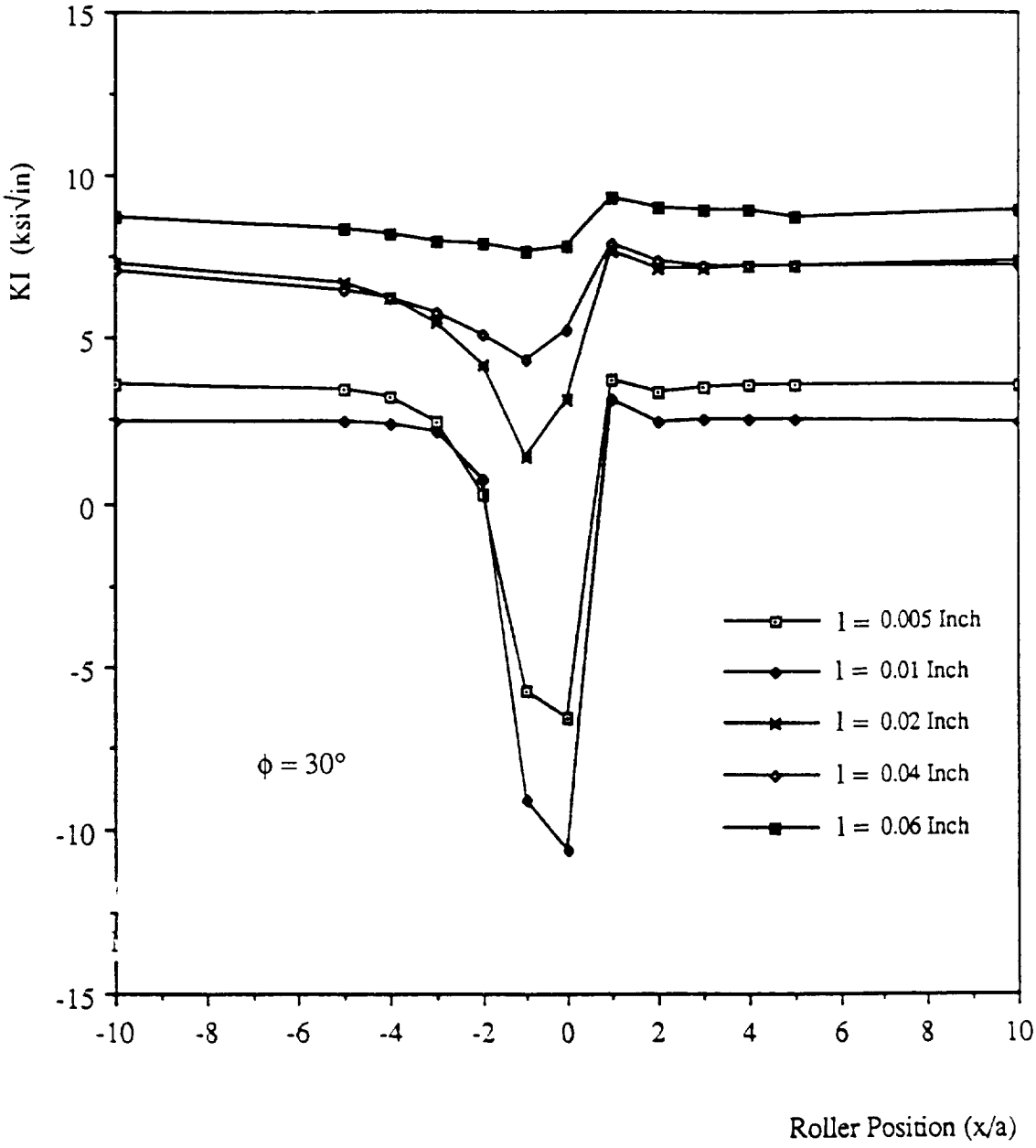

Figure 5.13 Variation of KI at $\theta = 90^{\circ}$ as a Function of Roller Position with Different Crack Length

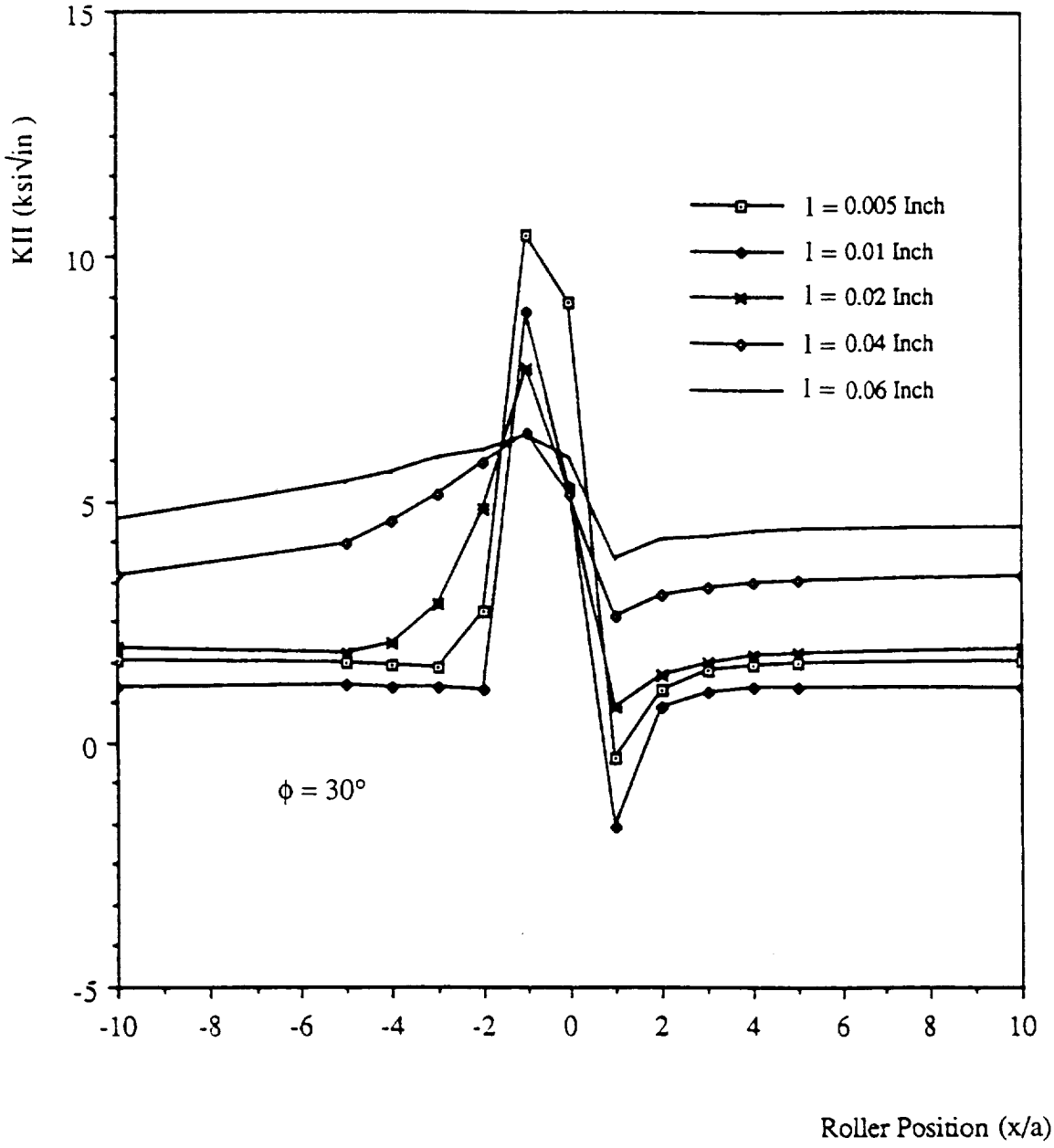

Figure 5.14 Variation of KII at $\theta = 90^{o}$ as a Function of Roller Position with Different Crack Length

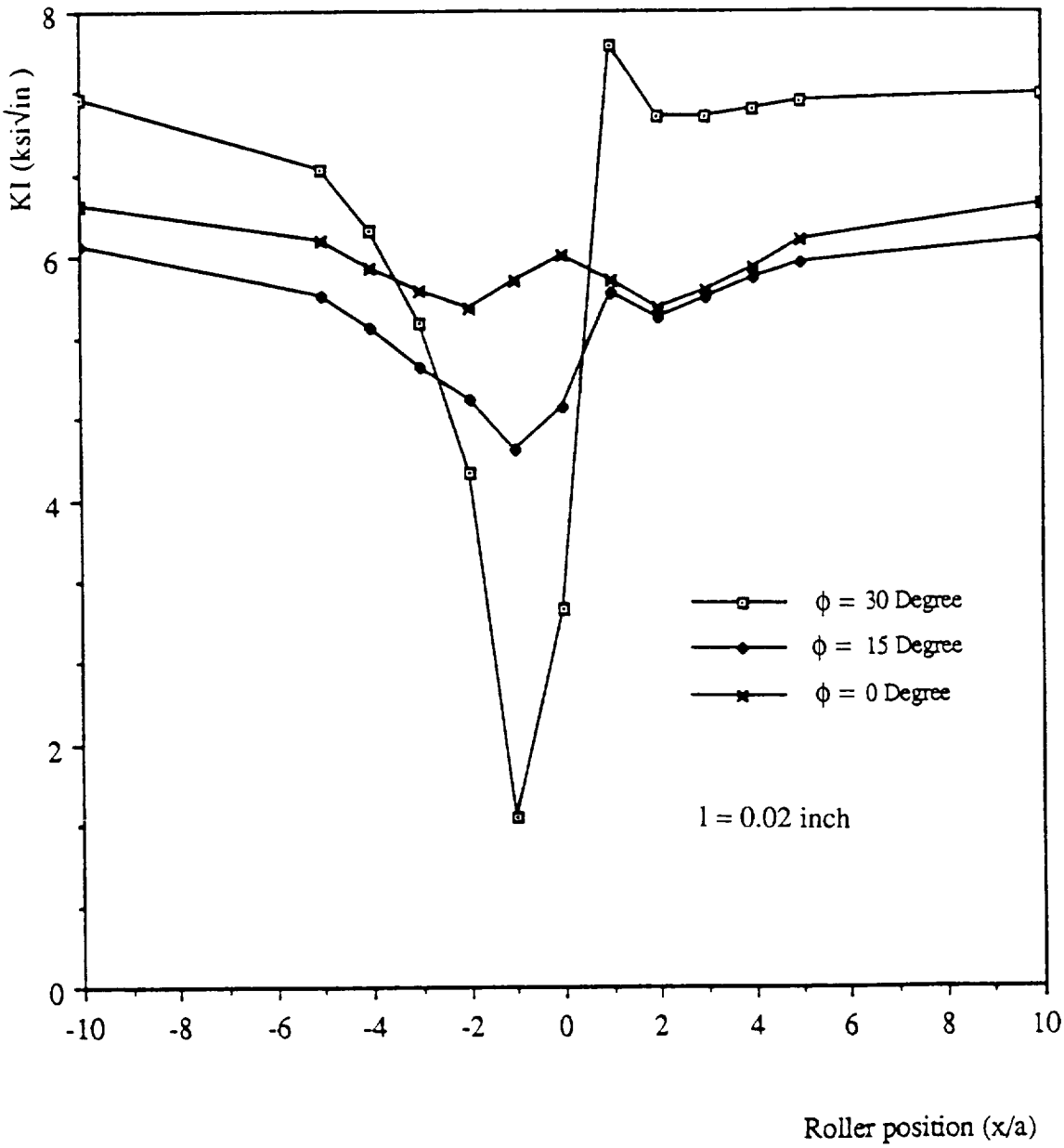

Figure 5.15 Variation of KI at $\theta = 90^{o}$ as a Function of Roller Position with Different Crack Length

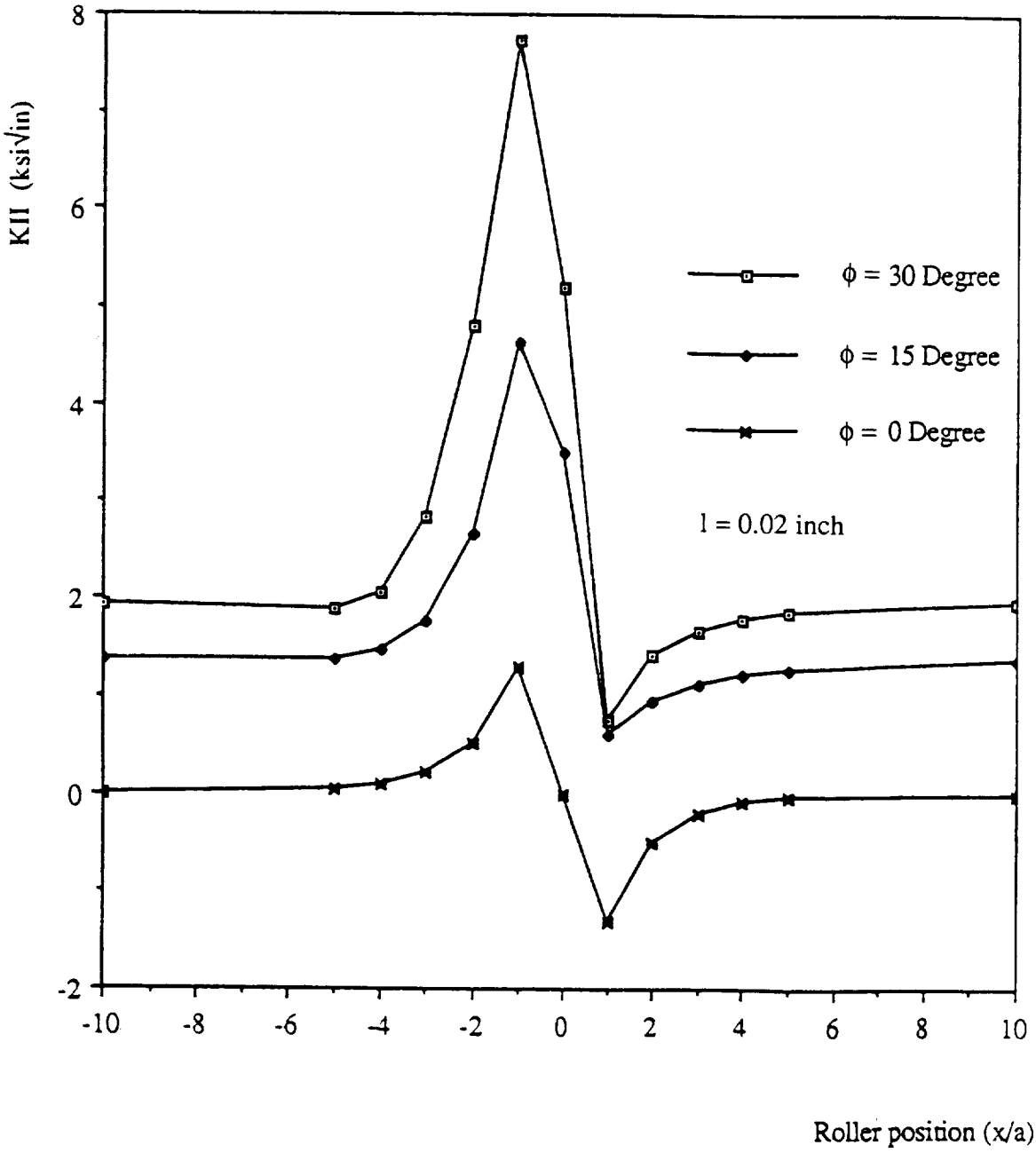

Figure 5.16 Variation of KII at $\theta = 90^{o}$ as a Function of Roller Position with Different Inclined Angle ϕ

CHAPTER SIX

CONCLUSIONS

A preliminary stress intensity factor analysis of a typical high speed bearing was conducted using the Boundary Element Method. The results obtained in the present three-dimensional analysis suggest lower mode K_{II} stress intensity factors than those predicted by the two-dimensional analysis in [6]. This is due to the fact that the total load needed to produce the experimentally measured 285 ksi Hertzian stress using a semi-spherical contact area is much lower than that using a cylindrical contact (27.5 lbs instead of 1500 lbs). This may be the reason why the predictions of Mendelson and Ghosns' [6] analyses are overly conservative. High K_I and K_{II} values were observed for cracks inclined at 30°. These results indicate that the interaction of the Hertzian load would lead to large propagation rates for cracks inclined at 30°.

Although the stress intensity factor data obtained from the analysis has not been reduced to a form suitable for life prediction, these preliminary results can provide a better understanding of the complex interactions between a surface crack, a moving Hertzian load, and an axial stress.

As for the further work, an incremental crack growth analysis of elliptical cracks using the Boundary Element Method and a fatigue crack growth law would be the next step. Also, more factors which affect the stress intensity factors of a crack such as friction between the roller and the raceway, the dynamic effect, etc. could be taken into consideration.

REFERENCES

1. Way, S., "Pitting Due to Rolling Contact", ASME Journal of Applied Mechanics, Vol. 2 ,1935, pp. A49-A38.

2. Fleming, J. R., and Suh, N. P., "Mechanics of Crack Propagation in Delamination and Wear", Wear, Vol. 44, 1977, pp. 39-56.

3. Fleming, J. R., and Suh, N. P.,"The Relationship Between Crack Propagation Rates and Wear Rates", Wear, Vol. 44, 1977, pp. 57-64.

4. Rosenfield, A. R., "A Fracture Mechanics Apporach to Wear", Wear, Vol. 61, 1980, pp. 125-132.

5. Clark, J. C., "Fracture Failure Modes in Light Weight Bearings", J. Aircraft, Vol. 12, 1975, pp. 383-387.

6. Mendelson, A., and Ghosn, L. J., "Analysis of Mixed-Mode Crack Propagation Using the Boundary Integral Method", NASA NAG-3-396, National Aeronautics and Space Administration, 1986.

7. Murakami, Y. "Mechanism of Surface Crack Growth in Lubricated Rolling/Sliding Spherical Contact", ASME, J. of Applied Mechanics, 1986, Vol. 53, pp. 354-360.

8. Foord, C. A., Hingley, C. G., and Cameron, A., "Pitting of Steel Under Varing Speeds and Combined Stresses", ASME, J. of Lubrication Technology, Vol. 91, pp. 282-293.

9. Rizzo, F. J., "An Integral Equation Approach to Boundary Value Problems of Classical Elastostatics", Quarterly Applied Mathematics, Vol. 25, 1967, pp. 83-95.

10. Kupradze, O. D., "Potential Methods in the Theory of Elasticity", Daniel Davey Co., New York, 1985.

11. Jaswan, M. A., "Integral Equation Methods in Potential Theory I", Proc. R. Soc. Ser. A., 275, 1963, pp. 23-32.

12. Symm, G. T., "Integral Equation Methods in Potential Theory II", Proc. R Soc. Ser. A., 275, 1963, pp. 33-46.

13. Cruse, T. A., "An Improved Boundary Integral Equation Method for Three Dimensional Elastic Stress Analysis", Computers & Structures, Vol. 4, pp. 741-754.

14. Latchat, J. C. and Watson, J. O., "Progress in the Use of Boundary Integral Equations, Illustrated by Examples", Computer Methods in Applied Mechanics and Engineering, Vol. 10, 1977, pp. 273-289.

15. Rizzo, F. J. and Shippy, D. J., "An Advanced Boundary Integral Equation

Method for Three Dimensional Thermoelasticity", International Journal for Numerical Methods in Engineering, Vol. 11, 1977, pp. 1753-1768.

16. Cruse, T. A. and Van Buren, W., "Three dimensional Elastic Stress Analysis of Fracture Specimen With An Edge Crack", International Journal of Fracture Mechanics, 1971, vol. 7, pp.1-15.

17. Blandford, G. E., Ingraffea, A. R., and Liggett, J. A., "Two Dimensional Stress Intensity Factor Computation Using the Boundary Element Method", International Journal of Numerical Method in Engineering, 1981, Vol. 17, pp. 387-404.

18. Barsoum, R. S., "On the Use of Isoparametric Finite Elements in Linear Fracture Mechanics", International Journal for Numerical Methods in Engineering, 1976, Vol. 10, pp. 25-37.

19. Cruse, T. A. and Wilson, R. B., "Boundary Integral Equation Method for Elastic Fracture Mechanics Analysis", AFOSR-TR-78-0355, 1977.

20. Cruse, T. A., "Mathematical Foundations of the Boundary Integral Equation Method in Solid Mechanics", AFOSR-TR-77-1002, 1977.

21. Sokolinikoff, I. S., "Mathematical Theory of Elasticity", McGraw-Hill, New York, 1956.

22. Saada, Adel S., "Elasticity, Theory and Applications", Robert E. Krieger Publishing Company Inc., 1983.

23. Timoshenko, S. P. and Goodier, J. N., "Theory of Elasticity", 3rd Ed., McGraw-Hill Company, 1986, pp. 271-274.

24. Lachat, J. C. and Watson, J. D., "Effective Numerical TReatment of Boundary Integral Equations: A Formulation for Three Dimensional Elastostatics", International Journal of Numerical Method for Engineering, Vol. 10, 1976, pp. 991-1005.

25. Cook, R. D., "Concepts and Applications of Finite element Analysis", John Wiley and Son, 1974.

26. Banerjee, P. K. and Butterfield, R., "Boundary Element Methods in Engineering Science", McGraw-Hill London, 1981.

27. Tada, H., Paris, P., and Irwin, G., "The Stress Analysis of Crack Handbook", Del Research Corporation, Hellerton, Pennsylvania, 1973.

28. Sih, G. C. and Liebowitz, H., "Mathematical Theories of Brittle Fracture", Fracture, an Advanced Treatise, Vol. 2, Mathematical Fundamentals, Academic Press Inc. New York, 1968, pp. 67-190.

29. Ingraffea, A. R. and Manu, C., "Stress Intensity Factor computation in Three Dimensions With Quarter-Point elements", International Journal for Numerical Methods in Engineering, Vol. 15, 1980, pp. 1427-1445.

30. Boresi, A. P. and Sidebottom, O. M., "Advanced Mechanics of Materials", 4th Edition, John Wiley & Sons Inc., 1985.

31. Bryant, M. D., Miller, G. R. and Keer, L. M., "Line Contact Between a Rigid Indenter and a Damaged Elastic Body",Quarterly Journal of Mechanics and Applied Mathematics, Vol.37, 1984, pp. 467-478.

APPENDIX A

SHAPE FUNCTIONS FOR ISOPARAMETRIC ELEMENTS

The shape functions for different elements are listed below corresponding to the elements shown in Fig.A.1.

(1) 3-Node Linear Triangular Element:

$$N_1 = \xi_1$$
$$N_2 = \xi_2$$
$$N_3 = \xi_3$$

where $\xi_1 + \xi_2 + \xi_3 = 1$

(2) 6-Node Quadratic Triangular Element:

$$N_1 = \xi_1(2\xi_1 - 1)$$
$$N_2 = \xi_2(2\xi_2 - 1)$$
$$N_3 = \xi_3(2\xi_3 - 1)$$
$$N_4 = 4\xi_1\xi_2$$
$$N_5 = 4\xi_2\xi_3$$
$$N_6 = 4\xi_3\xi_1$$

where $\xi_1 + \xi_2 + \xi_3 = 1$

(3) 4–Node Linear Quadrilateral Element:

$$N_1 = (1 - \xi_1)(1 - \xi_2) / 4$$

$$N_2 = (1 + \xi_1)(1 - \xi_2) / 4$$

$$N_3 = (1 + \xi_1)(1 + \xi_2) / 4$$

$$N_4 = (1 - \xi_1)(1 + \xi_2) / 4$$

(4) 8-Node Quadratic Quadrilateral Element:

$$N_1 = -(1+\xi_1+\xi_2)(1 - \xi_1)(1 - \xi_2) / 4$$

$$N_2 = -(1+\xi_1-\xi_2)(1 + \xi_1)(1 - \xi_2) / 4$$

$$N_3 = (-1+\xi_1+\xi_2)(1 + \xi_1)(1 + \xi_2) / 4$$

$$N_4 = -(1+\xi_1-\xi_2)(1 - \xi_1)(1 + \xi_2) / 4$$

$$N_5 = (1 - \xi_1^2)(1 - \xi_2) / 2$$

$$N_6 = (1 + \xi_1)(1 - \xi_2^2) / 2$$

$$N_7 = (1 - \xi_1^2)(1 + \xi_2) / 2$$

$$N_8 = (1 - \xi_1)(1 - \xi_2^2) / 2$$

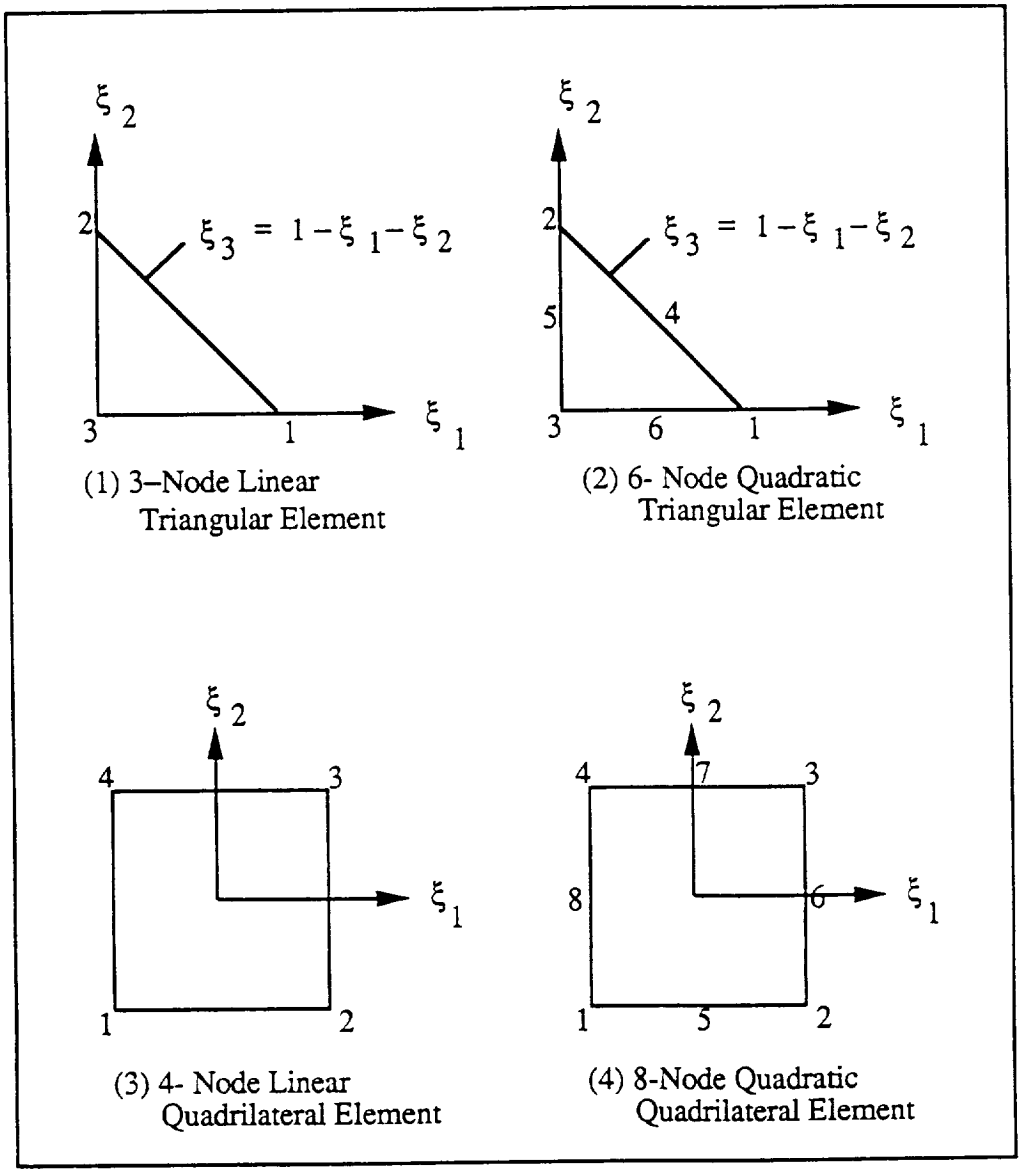

Figure A.1 Isoparametric Elements

APPENDIX B

TRANSFORMATION FUNCTIONS

The integral on a boundary surface element with domain Γ can be expressed as

$$I = \int_{\Gamma} \kappa(x,y)dxdy$$

In order to overcome the 1/r singularity of the kernel the integral is first transformed from the Cartesian coordinate system to the parametric ξ-coordinate system by using the shape functions

$$x = \sum_{i=1}^{n_m} N_i(\xi_1,\xi_2)X_i$$

$$y = \sum_{i=1}^{n_m} N_i(\xi_1,\xi_2)Y_i$$

corresponding with the Jacobian

$$J_1(\xi_1,\xi_2) = \begin{vmatrix} \frac{\partial x}{\partial \xi_1} & , & \frac{\partial x}{\partial \xi_2} \\ \\ \frac{\partial y}{\partial \xi_1} & , & \frac{\partial y}{\partial \xi_2} \end{vmatrix}$$

such that the integral becomes

$$I = \int_{\Gamma_\xi} \kappa(\xi_1,\xi_2) J_1(\xi_1,\xi_2) d\xi_1 d\xi_2$$

The integral on the isoparametric element is then divided into several triangles according to the location of the singular node. The singular integral on each triangle is carried out by using a polar coordinate system with its origin at the singular node such that

$$\xi_1 = f_i(r,\theta)$$
$$\xi_2 = g_i(r,\theta)$$

$$J_2(r,\theta) = \begin{vmatrix} \frac{\partial \xi_1}{\partial r} & , & \frac{\partial \xi_1}{\partial \theta} \\ \\ \frac{\partial \xi_2}{\partial r} & , & \frac{\partial \xi_2}{\partial \theta} \end{vmatrix}$$

and

$$I = \sum_{i=1}^{n_T} \int_{T_i} \kappa(r,\theta) J_1(r,\theta) J_2(r,\theta) dr d\theta$$

where n_T is the total number of triangles in which the isoparametric element is divided and T_i is the corresponding domain. The Jacobian $J_2 = r$ can remove the 1/r singularity. In order to accomplish the integral numerically by the Gaussian quadrature the polar coordinate is again transfered to a system with both coordinates ranging from -1 to 1 by the transforming functions

$$r = h_i(\underline{r}, \underline{\theta})$$
$$\theta = l_i(\underline{r}, \underline{\theta})$$

$$J_3 = \begin{vmatrix} \frac{\partial r}{\partial \underline{r}} & , & \frac{\partial r}{\partial \underline{\theta}} \\ \\ \frac{\partial \theta}{\partial \underline{r}} & , & \frac{\partial \theta}{\partial \underline{\theta}} \end{vmatrix}$$

The integral then becomes

$$I = \sum_{i=1}^{n_T} \int_{T_i} \kappa(\underline{r},\underline{\theta}) J_1(\underline{r},\underline{\theta}) J_2(\underline{r},\underline{\theta}) J_3(\underline{r},\underline{\theta}) d\underline{r} d\underline{\theta}$$

$$= \sum_{i=1}^{n_T} \left[\sum_{a=1}^{n_a} \sum_{b=1}^{n_b} w_1^a w_2^b \kappa(\underline{r}^a,\underline{\theta}^b) J_1(\underline{r}^a,\underline{\theta}^b) J_2(\underline{r}^a,\underline{\theta}^b) J_3(\underline{r}^a,\underline{\theta}^b) d\underline{r} d\underline{\theta} \right]$$

where n_a and n_b are the order of the Gaussian quadrature. The transforming functions for different element are illustrated in the following pages.

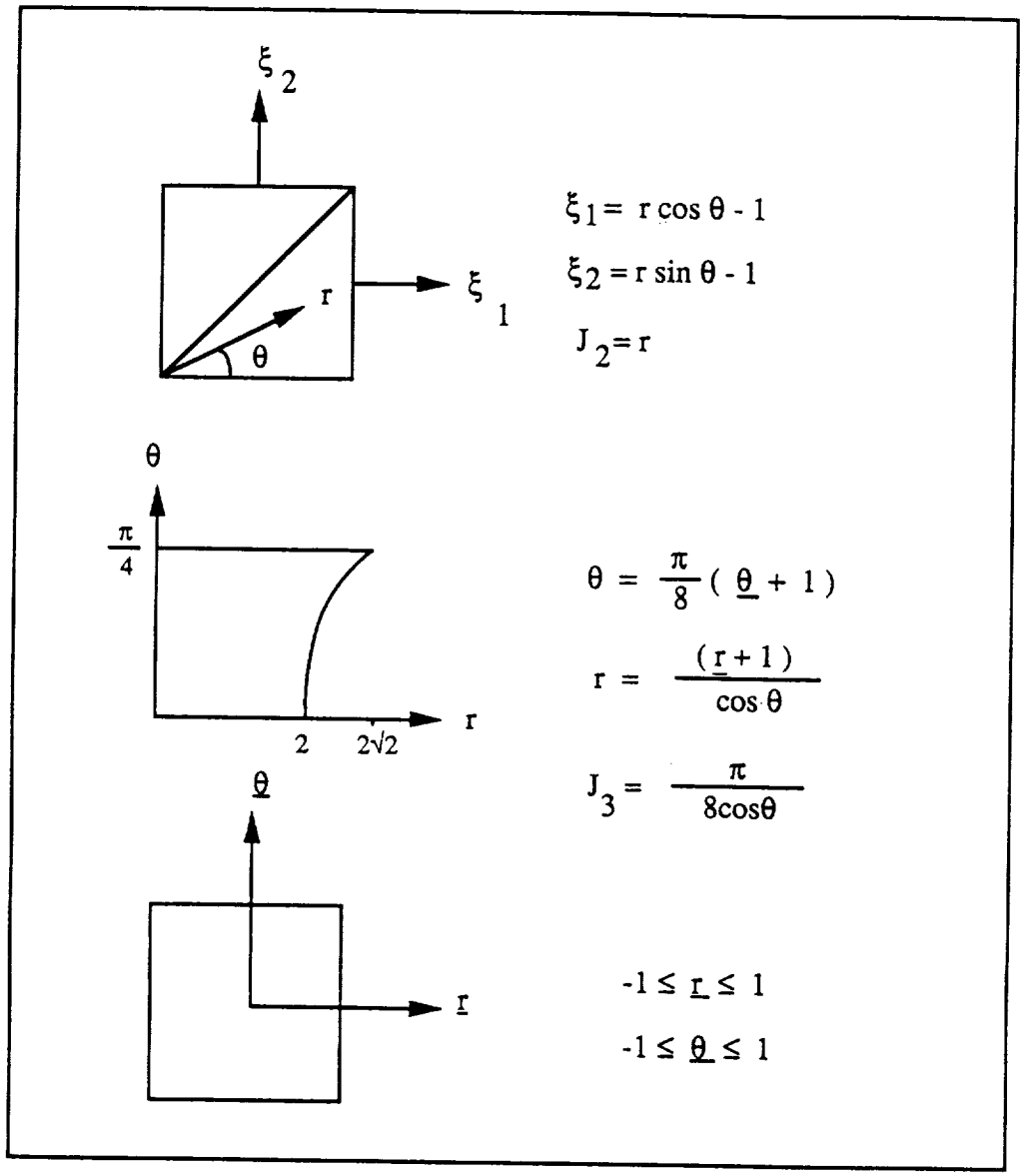

Figure B.1.a Illustration of Transformation of Coordinate System

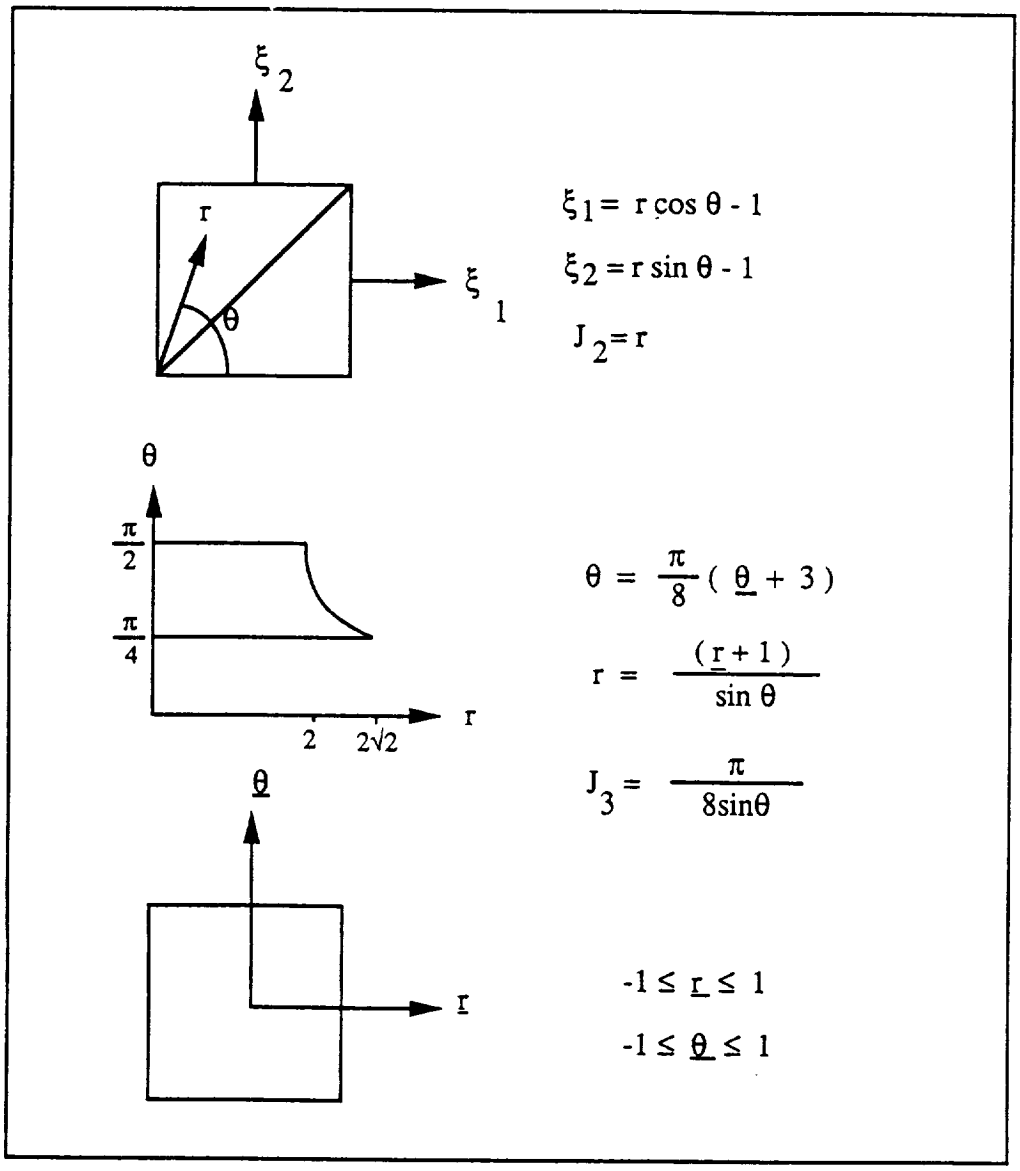

Figure B.1.b Illustration of Transformation of Coordinate System

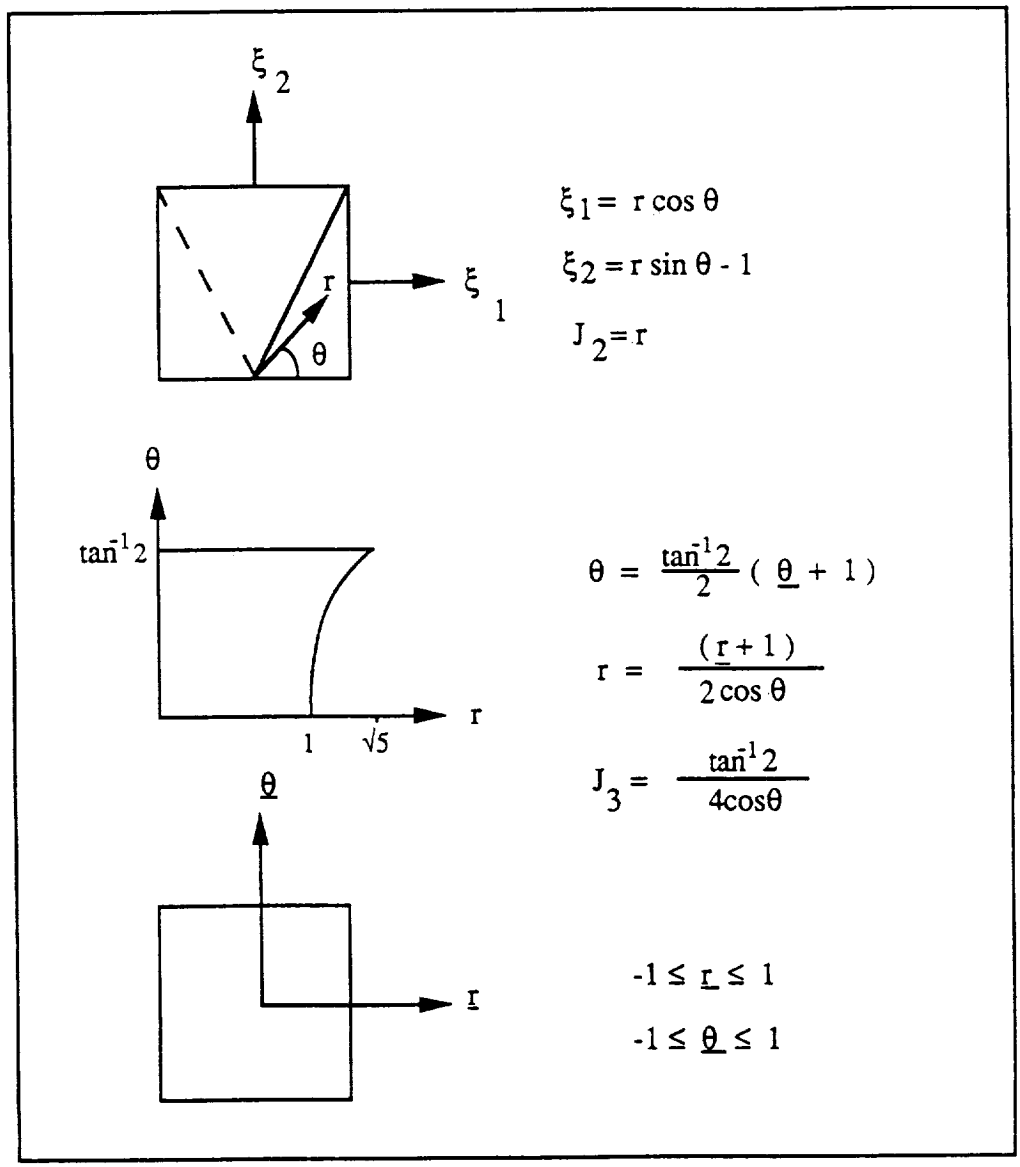

Figure B.1.c Illustration of Transformation of Coordinate System

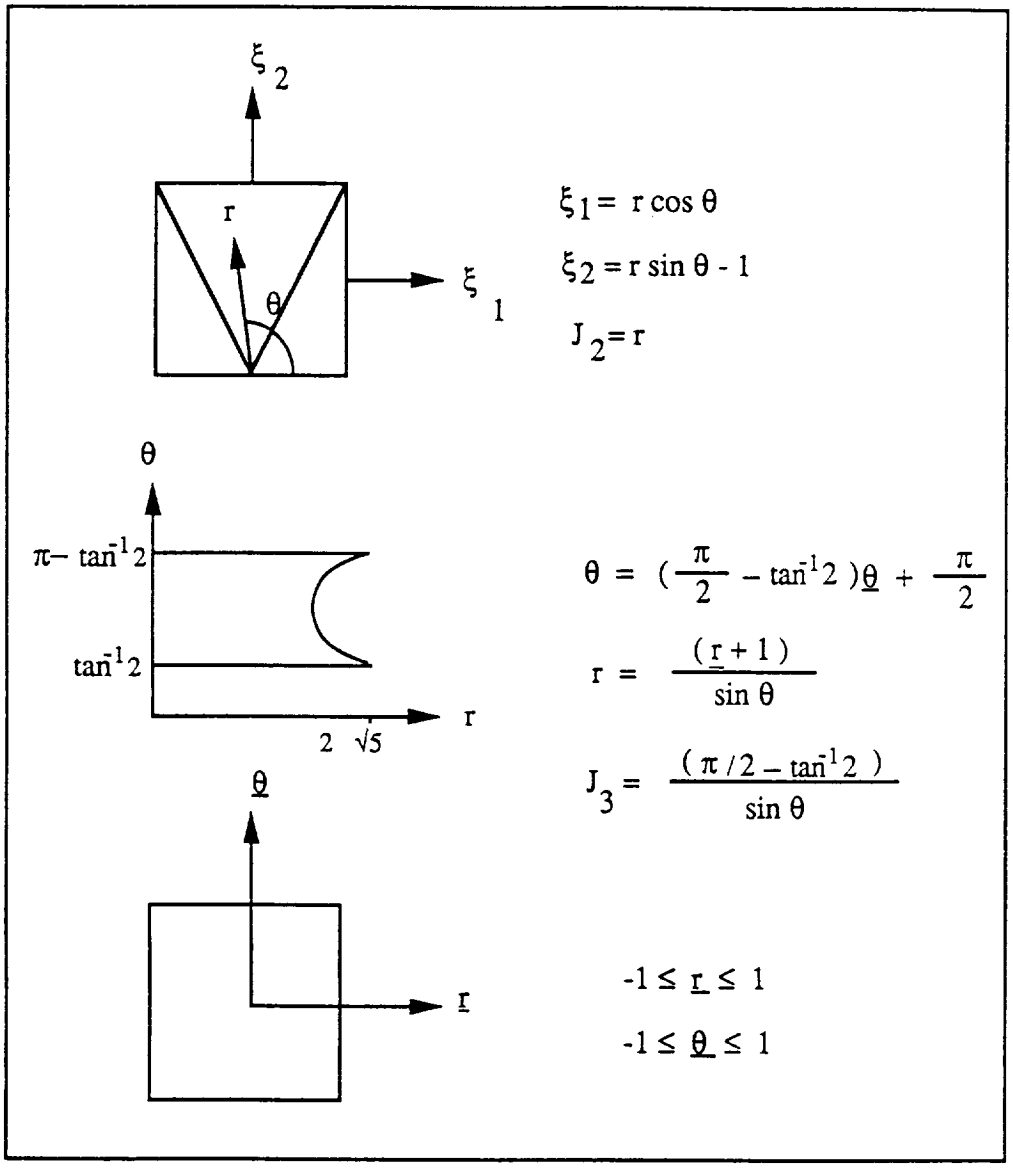

Figure B.1.d Illustration of Transformation of Coordinate System

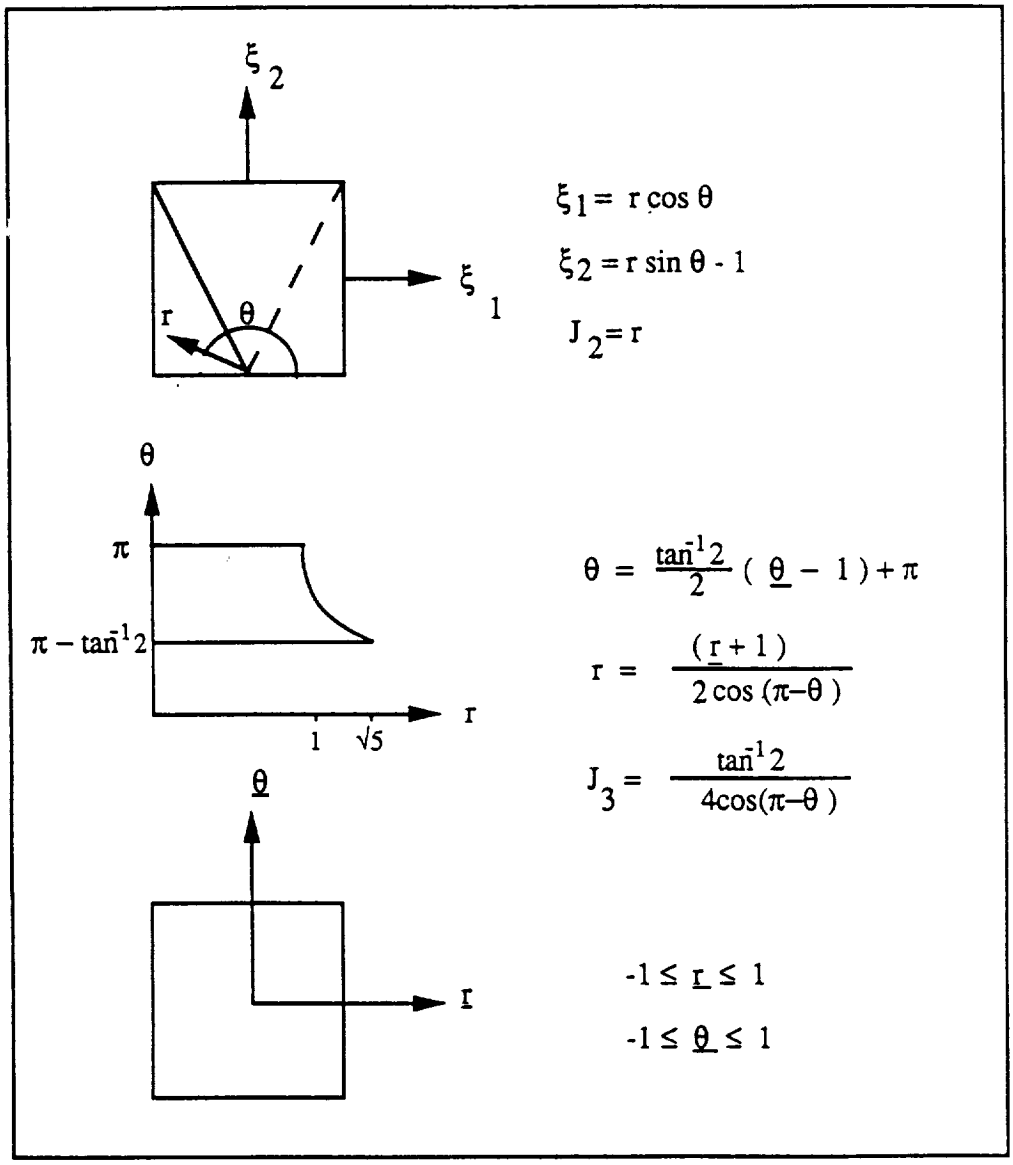

Figure B.1.e Illustration of Transformation of Coordinate System

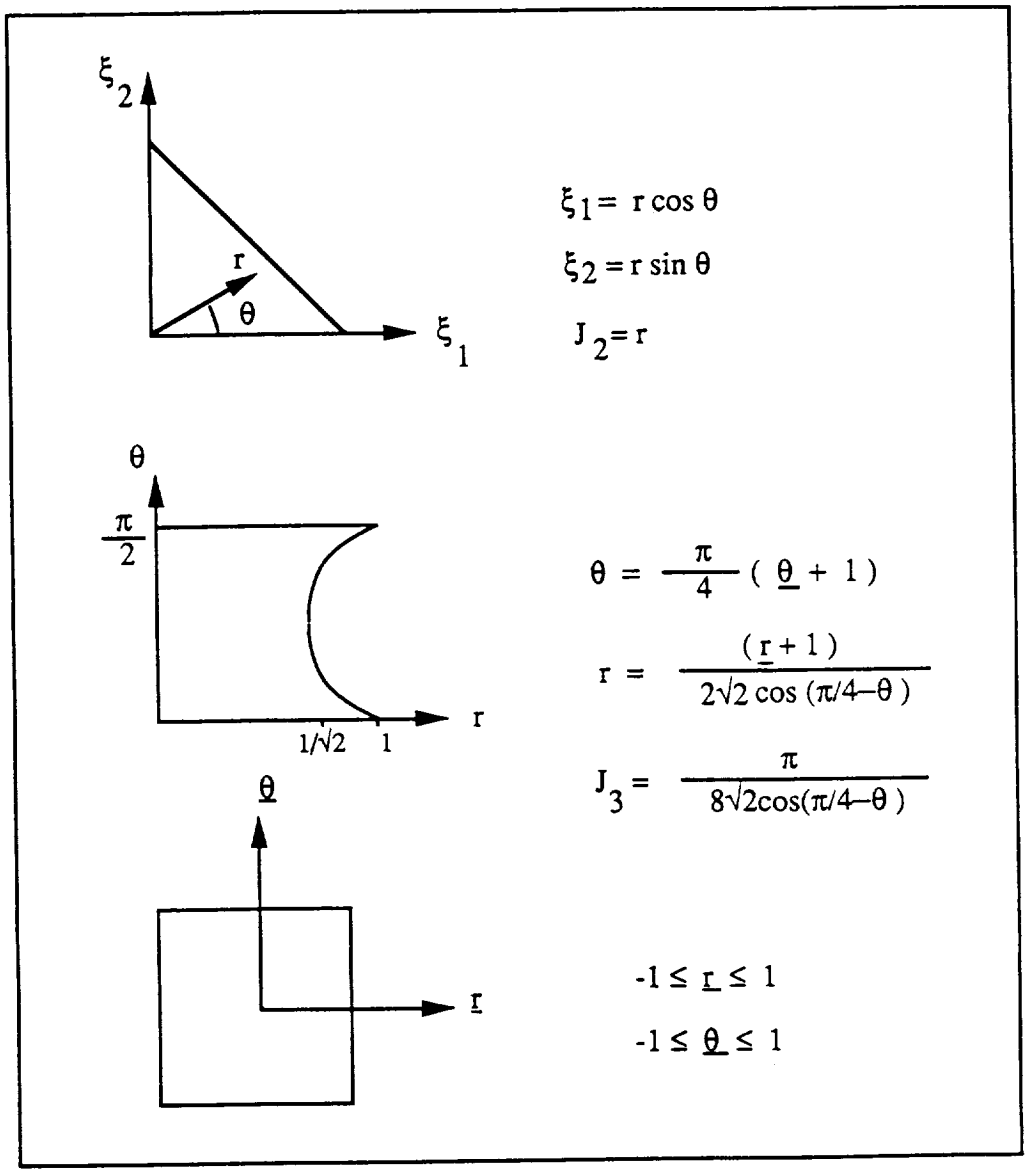

Figure B.1.f Illustration of Transformation of Coordinate System

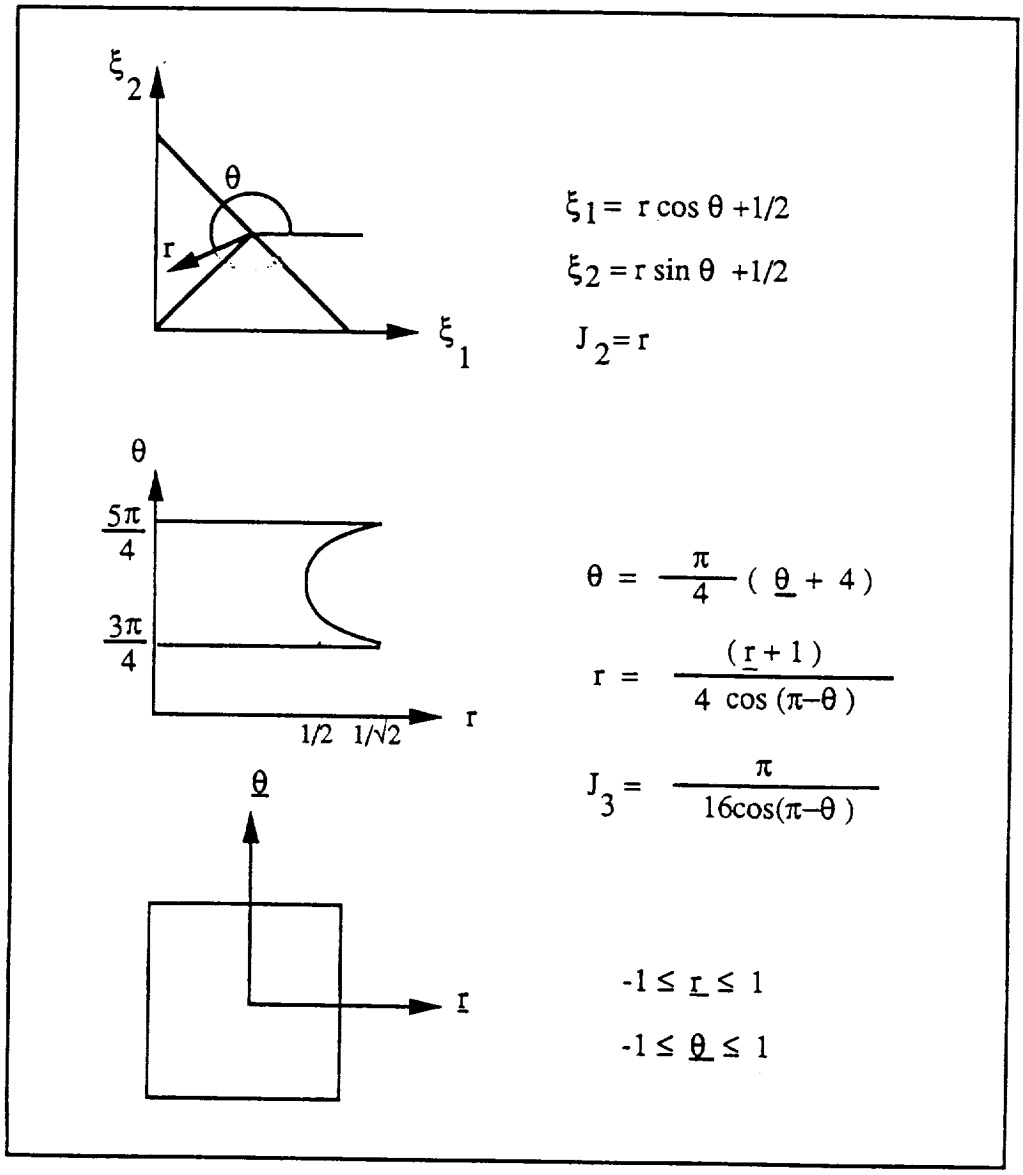

Figure B.1.g Illustration of Transformation of Coordinate System

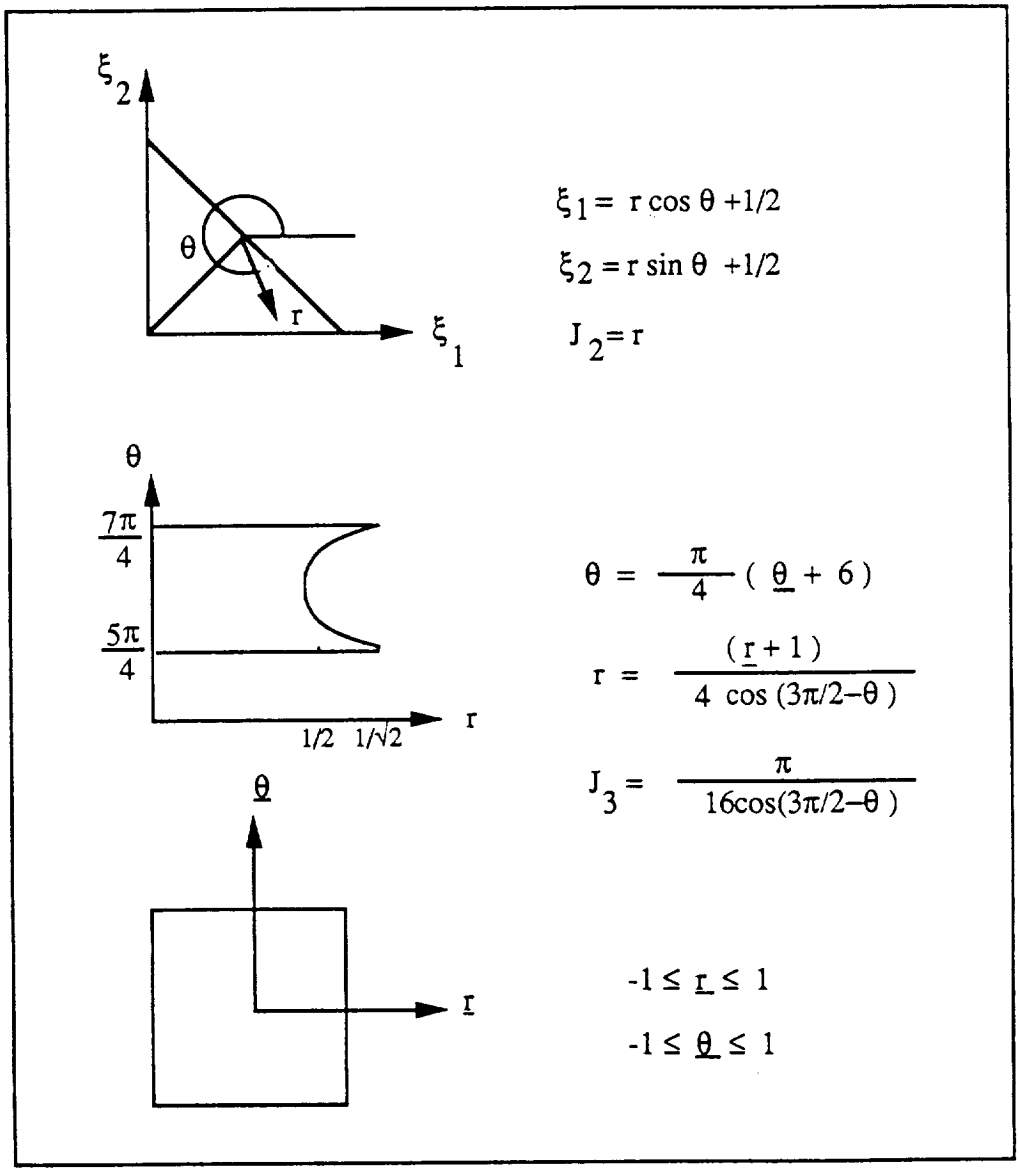

Figure B.1.h Illustration of Transformation of Coordinate System

NASA
National Aeronautics and Space Administration

Report Documentation Page

1. Report No.	2. Government Accession No.	3. Recipient's Catalog No.
NASA CR-4254		

4. Title and Subtitle
Three-Dimensional Analysis of Surface Crack-Hertzian Stress Field Interaction

5. Report Date
October 1989

6. Performing Organization Code

7. Author(s)
R. Ballarini and Y. Hsu

8. Performing Organization Report No.
None (E-5013)

10. Work Unit No.
505-63-1B

9. Performing Organization Name and Address
Case Western Reserve University
Department of Civil Engineering
Cleveland, Ohio 44106

11. Contract or Grant No.
NAG3-396

13. Type of Report and Period Covered
Contractor Report
Final

12. Sponsoring Agency Name and Address
National Aeronautics and Space Administration
Lewis Research Center
Cleveland, Ohio 44135-3191

14. Sponsoring Agency Code

15. Supplementary Notes
Project Manager, John L. Shannon, Jr., Structures Division, NASA Lewis Research Center.

16. Abstract

This thesis presents the results of a stress intensity factor analysis of semicircular surface cracks in the inner raceway of an engine bearing. The loading consists of a moving spherical Hertzian contact load and an axial stress due to rotation and shrink fit. A three dimensional linear elastic Boundary Element Method code was developed to perform the stress analysis. The element library includes linear and quadratic isoparametric surface elements. Singular quarter point elements were employed to capture the square root displacement variation and the inverse square root stress singularity along the crack front. The program also possesses the capability to separate the whole domain into two subregions. This procedure enables one to solve nonsymmetric fracture mechanics problems without having to separate the crack surfaces a priori. A wide range of configuration parameters was investigated. The ratio of crack depth to bearing thickness was varied from one-sixtieth to one-fifth for several different locations of the Hertzian load. The stress intensity factors for several crack inclinations were also investigated. The results demonstrate the efficiency and accuracy of the Boundary Element Method. Moreover, the results can provide the basis for crack growth calculations and fatigue life prediction.

17. Key Words (Suggested by Author(s))	18. Distribution Statement
Surface crack; Hertzian loading; Bearing; Boundary element method; Three-dimensional analysis	Unclassified – Unlimited Subject Category 39

19. Security Classif. (of this report)	20. Security Classif. (of this page)	21. No of pages	22. Price*
Unclassified	Unclassified	164	A08

NASA FORM 1626 OCT 86

*For sale by the National Technical Information Service, Springfield, Virginia 22161

NASA-Langley, 1989